NATURE PUBLISHING GROUP

nature photonics

A bright approach to E-paper

nature photonics

ORIGINAL RESEARCH TYPESET BY Techset Composition Ltd, www.techset.co.uk
PRINTED BY Wyndeham Grange, www.wyndeham.co.uk

MAY 2009 VOL 3 ISSUE 5

nature photonics

COVER IMAGE

Electronic paper that offers a large contrast, strong saturated colours and a bright appearance in ambient light may soon be a realistic prospect thanks to the development of an electrofluidic display. The display reported by Jason Heikenfeld and his co-workers operates by using electromechanical forces to control the extent to which water-based inks cover the surface of miniature aluminium reflectors that serve as pixels.

Article p292
News & Views p248
Interview p304

ON THE COVER

Solar cells
Organics beat recombination
Article p297, News & Views p250

Random lasers
Operational insights
Letter p279, News & Views p246

Plasmomics
Electrical detection
Letter p283

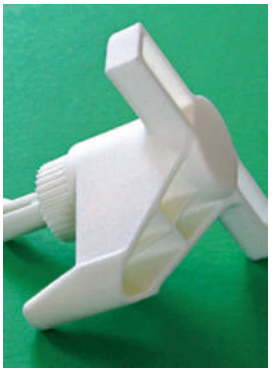

Laser sintering, the solidification of metal or plastic powders using a laser beam, is proving to be a valuable tool for rapid prototyping in the automotive and medical sectors.
Industry Perspective p265

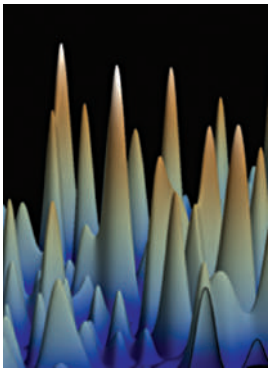

The question of whether laser modes in random laser media are strongly or weakly localized has been a topic of debate for sometime, now German researchers demonstrate experimentally that both can coexist.
Letter p279
News & Views p246

nature publishing group

Nature Photonics (ISSN 1749-4885) is published monthly by Nature Publishing Group (Porters South, 4 Crinan Street, London N1 9XW, UK). Editorial Office: Chiyoda Building, 5-6th Floor, 2-37 Ichigaya Tamachi, Shinjuku-ku, Tokyo, 162-0843, Japan. Telephone: +81 (0)3 3267 8751. Fax: +81 (0)3 3267 8754. Email: naturephoton@nature.com. North American Advertising: *Nature Photonics*, 75 Varick Street, 9th Floor, New York, NY, 10013-1917, US. Telephone: +1 212 726 9200. Fax: +1 212 696 9006. European Advertising: *Nature Photonics*, Porters South, 4 Crinan Street, London N1 9XW, UK. Telephone: +44 (0)20 7833 4000. Fax: +44 (0)20 7843 4596. Asia-Pacific Advertising: *Nature Photonics*, Chiyoda Building, 5-6th Floor, 2-37 Ichigaya Tamachi, Shinjuku-ku, Tokyo, 162-0843, Japan. Telephone: +81 (0)3 3267 8754. Fax: +81 (0)3 3267 8746. New subscriptions/renewals/changes of address/back issues and all other customer service questions should be addressed to - North America: *Nature Photonics*, Subscriptions Department, PO Box 5054, Brentwood, TN 37024-5054, USA. Outside North America: Subscriptions Department, Brunel Road, Basingstoke, Hants. RG21 6XS, UK. Telephone: +44 (0)1256 329242; Fax: +44 (0)1256 812358: Nature Asia-Pacific, Chiyoda Building, 5-6th Floor, 2-37 Ichigaya Tamachi, Shinjuku-ku, Tokyo, 162-0843, Japan. Telephone +81 (0)3 3267 8751. Annual subscription rates: US/Canada US$3060, Canada add 5% GST (institutional/corporate), US$152, Canada add 5% GST (individual making personal payment); UK/Rest of World (excluding Europe and Japan) £1570 (institutional/corporate), £78 (individual making personal payment); Europe €2430 (institutional/corporate), €121 (individual making personal payment). Back issues: US/Canada $45, Canada add 5% GST; Rest of World: surface mail US$43, air mail US$45. *Nature Photonics* (ISSN 1749-4885) is published monthly by Nature Publishing Group, c/o Mercury Airfreight International Ltd, 365 Blair Road, Avenel, NJ 07001, USA. Periodicals postage is paid at Rahway NJ. Postmaster: send address changes to *Nature Photonics*, c/o Mercury Airfreight International, 365 Blair Road, Avenel, NJ 07001, USA. Reprints: *Nature Photonics* Reprints Department, Porters South, 4 Crinan Street, London N1 9XW, UK. Subscription information is available at the *Nature Photonics* homepage at http://www.nature.com/naturephotonics. Postmaster: send address changes to *Nature Photonics* Subscriptions Department, Brunel Road, Basingstoke, Hants. RG21 6XS, UK or *Nature Photonics* Subscriptions Department PO Box 5054, Brentwood, TN 37024-5054, USA.

Combating plagiarism

Accountability of coauthors for scientific misconduct, guest authorship and deliberate or negligent citation plagiarism, highlight the need for accurate author contribution statements.

Almost one hundred years ago in 1912, in a gravel pit in the village of Piltdown, East Sussex, England, the fragments of a skull and jawbone belonging to an early human were found, providing a new link between ape and man — or so it seemed. Today, however, Piltdown is famed not for a magnificent scientific discovery, but for scientific misconduct that stunted research on human evolution for decades.

Eoanthropus dawsoni, or 'Dawson's dawn-man', named after Charles Dawson who presented the specimen to the scientific community, was only definitively proved to be fraud some 40 years later in 1953 when the remains were shown to consist of the skull of a medieval-age man, the 500-year-old jaw of an orangutan and the teeth of a chimpanzee. The identity of the Piltdown forger is still unclear. What is abundantly clear is the damage that resulted; the 'find' sent many researchers in wrong directions, and for nearly two decades genuine finds were ignored by many and hundreds of papers related to the fraud were written.

Although it is to be hoped that scientific misconduct, including plagiarism, remains a fringe activity, the motivations are obvious. If undetected, it is conceivable that even subtle forms of misconduct may benefit an offender's career, for example in getting their PhD, securing a permanent faculty position or enhancing a grant proposal.

Many forms of plagiarism exist, but the goal is generally the same — to garner false or undue credit. Plagiarism sometimes involves reuse of another author's published work, but it is commonly thought that the most typical tool of the plagiarist is self-plagiarism: the reuse of substantial parts of an author's own published work, particularly without appropriate referencing, and less commonly, duplicate publication, in which the results are recycled in their entirety.

The peer-review process provides a net for catching offenders, but it cannot provide a fail-safe barrier. As a result, *Nature Photonics* is now starting to use the plagiarism-detection software CrossCheck[1], which makes comparative checks between provided manuscripts and those previously published and in an existing database. Any manuscript that seems to show an abnormally high match will be immediately investigated. Unfortunately, plagiarism can also occur without verbatim duplication of words or data. And it is here that the lines between normal and acceptable activity and plagiarism become smeared, and the likelihood of detection and punitive repercussions is diminished.

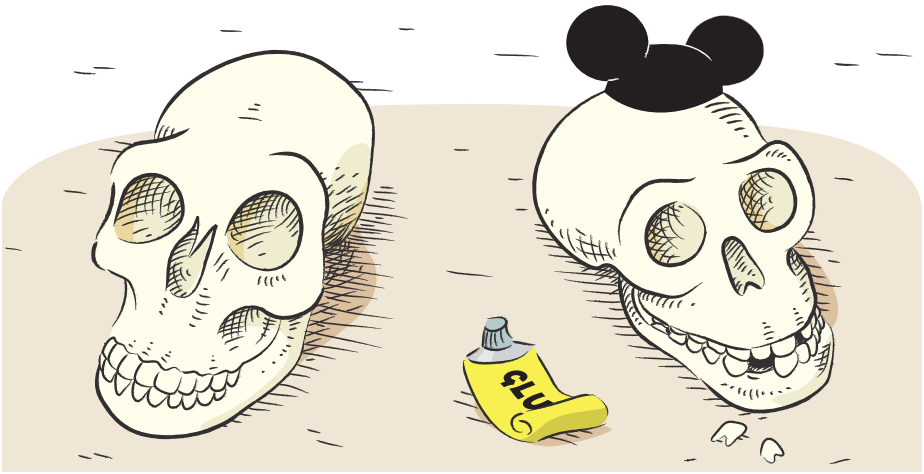

TOM WILSON

Using another researcher's arguments and logic, even if the text is not identical, without due reference is intellectual plagiarism. This type of plagiarism can be subtle and as simple as not including a reference to a highly relevant previous paper. Citation-related plagiarism, whether it is intentional, or due to gross negligence, can give an untruthful impression of precedence, reassigning credit from the original discoverer to another person.

When reporting scientific messages, it is an author's responsibility to find and acknowledge the critically relevant literature, or at least to have endeavoured to do so with rigour. Failing this can result in falsely apportioned claims, albeit caused by negligence.

If plagiarism is suspected in research results published by us, it is our policy to conduct an immediate investigation and if deemed appropriate to contact the author's institute and funding agencies and consider a formal retraction of the paper[2]. Although it is often the first authors who have historically borne the brunt of confirmed misconduct allegations, our editorial policies highlight the serious responsibilities of all coauthors: "submission to a Nature journal is taken by the journal to mean that all the listed authors have agreed to the content"[3]. It is unreasonable to expect each author to be responsible for every aspect of the paper, but it is the responsibility of the corresponding author to manage the understanding that all authors are expected to have made reasonable attempts to check the findings submitted to a journal for publication[3].

To help clarify author contributions, the current policy of Nature research journals is: "Authors are strongly encouraged to include a statement in the end notes to specify the actual contribution of each coauthor to the completed work"[3]. Such a statement serves at least two useful purposes: it is a statement that (should) clearly state each author's contribution, and hence to some extent also their responsibility in the case of misconduct, and it serves to discourage guest authorship — the unscrupulous practice of including authors for other than scientific reasons. We strongly recommend that all authors of papers submitted to *Nature Photonics* file such contributions for reasons of transparency, and as a model for good working practices for the communication of scientific research.

Published ideas, thoughts, concepts and results are the tangible essence of a scientist, and must be defended.

References

1. http://www.crossref.org/crosscheck.html
2. http://www.nature.com/authors/editorial_policies/plagiarism.html
3. http://www.nature.com/authors/editorial_policies/authorship.html

Future optical technologies for telescopes

Colin Cunningham

New optical technologies have revolutionized astronomy, from the invention of the telescope 400 years ago to more recent developments of adaptive optics and segmented mirrors. The next disruptive technologies could well emerge from integrated photonic devices.

With 2009 being the International Year of Astronomy, it is an apt time to reflect on just how far telescope technologies have come, and speculate about the future. Just over 400 years ago, Hans Lipperhey filed a patent for an optical device that he (and possibly other Dutch spectacle makers) had invented by putting together a converging and a diverging lens to make a revolutionary instrument that could magnify distant objects, in particular military targets. The patent was refused, but the device spread rapidly round Europe, and most importantly to Italy.

Here, Galileo took this crude device with a magnification of around ×3 and refined it, by improving lens quality, until he had a useable magnification of ×20. Galileo gave very few details of his observing techniques, but it seems likely that the critical and counterintuitive (in those days before aberration theory) innovation was the improvement in image quality by 'stopping down' the aperture[1]; it is now well known that making the aperture smaller improves image quality. Galileo used his device, as shown in Fig. 1a, to discover the moons of Jupiter, and so confirmed his conviction of the validity of the Copernican model of the Solar System.

The drive was then on to build bigger and more powerful telescopes with greater magnification. It was soon realized that what was to become known as chromatic aberration was a limiting factor in refracting telescopes, and that this could be overcome by making lenses with longer focal length, resulting in monsters like Hevelius's 45-metre-long telescope in Danzig. Two key inventions enabled astronomers to overcome the problem of chromatic aberration: the invention of the reflecting telescope described by James Gregory and built in a different form by Isaac Newton (Fig. 1b), and the invention of the achromatic doublet by John Dolland and others (Fig. 1c).

In the nineteenth century, the emergence of diffraction theory enabled telescope builders to understand in more detail the benefits of larger-aperture telescopes — mainly higher sensitivity and higher spatial resolution due to the collection of more photons and reduced diffraction effects, respectively. Refracting telescopes dominated the nineteenth century, with the size of apertures rising to reach the physical limits for lens manufacture at a diameter of around one metre. A key optical development that allowed the one-metre barrier to be broken was the introduction of silvered-glass mirrors by Foucault[2] in 1857 (Fig. 1d). This opened the way for the great reflecting telescopes of the twentieth century — epitomized by the 200-inch Hale on Mount Palomar and by the space telescopes.

It was not until the 1990s that the next physical barrier, transportation, was overcome. On the ground, the maximum mirror size is determined by what can be taken up a mountain road; and in space, by what can be enclosed in a launcher shroud. The solution to both problems was another optical technology: segmented mirrors. First used by Guido Horn D'Arturo[3] in Bologna in 1935–52, the idea of constructing a primary mirror from co-phased hexagonal segments was perfected by Jerry Nelson's Californian team in building the two 36-segment 10-metre Keck telescopes on Mauna Kea in Hawaii (Fig. 1e). It is this technology that now opens the door to much bigger telescopes on the ground, for example the 42-metre European Extremely Large Telescope (ELT) being designed by the European Southern Observatory (Fig. 2), which will have nearly a thousand segments, and in space with the deployable segmented-mirror James Webb Space Telescope which is due to launch in 2013.

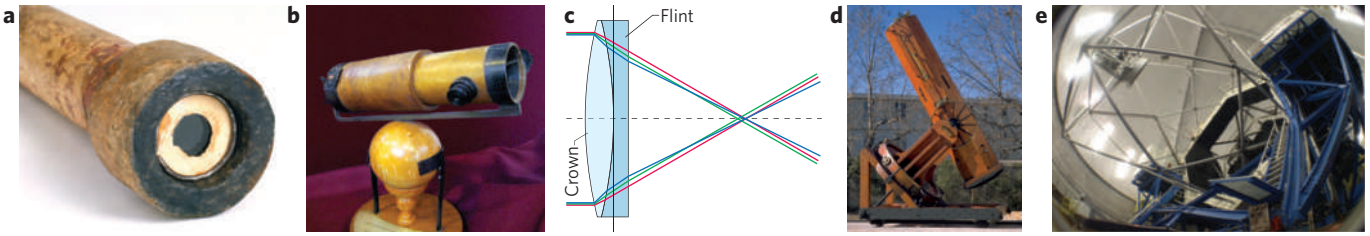

Figure 1 | Key optical innovations in astronomy. **a**, 1609: Galileo's two-lens refracting telescope (image © Photo Franca Principe, IMSS - Florence); **b**, 1668: Isaac Newton's reflecting telescope (image © Andrew Dunn); **c**, 1758: Dolland's achromatic doublet lens; **d**, 1857: Foucault's silvered-glass reflecting primary reflector (Marc Heller, © 1997 Région Provence-Alpes-Côte d'Azur - Inventaire général); **e**, 1992: Keck segmented-primary mirror telescope. A parallel development in controllability pushed the telescope from a passive device to a fully adaptive computer-controlled system able to track sources automatically, correct for gravity-induced structural deformation and finally cancel out atmospherically generated distortion of the incoming wavefront (image courtesy of Scott Kardel).

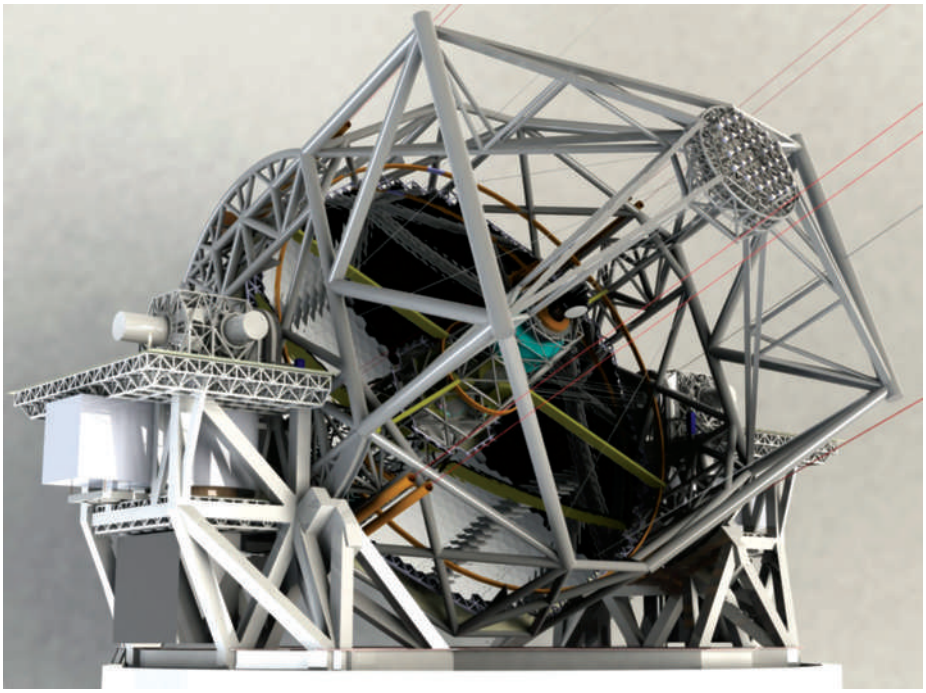

ESO

Figure 2 | The European Extremely Large Telescope.

On the ground, it is not diffraction that limits the spatial resolution of a telescope, but turbulence in the atmosphere blurring the image. Even at the best observing sites in the world on high mountain tops, the best images that can be obtained with standard optics have a resolution of about half an arcsecond, equivalent to resolving features separated by 1 km on the Moon as viewed from the Earth. This is the same size as the diffraction spot from a telescope of only 0.25 metres in diameter operating at visible wavelengths — so why did we build bigger telescopes than this? The answer is to collect more photons to get higher sensitivity and measure light from fainter objects that are further away. The most obvious way to defeat this limitation of imaging through the atmosphere was to go into space, giving us the spectacular results of the Hubble Space Telescope. Now we have another way: ground-based optical technologies that use adaptive optics (a technique invented over 50 years ago by Horace Babcock[4]) to cancel out distortions introduced by the atmosphere.

Thanks to adaptive optics it is now possible to get very close to the diffraction limit of performance by measuring wavefront errors and correcting them by introducing inverse distortions in a deformable mirror. The European ELT is an adaptive telescope with built-in deformable mirrors. It aims to approach diffraction-limited performance in the near-infrared wavelength region and resolve 8 milliarcseconds — equivalent to a mere 14 metres on the Moon as viewed from the Earth.

This type of adaptive optics system has been very successful on the current generation of telescopes 8–10 metres in diameter, allowing direct imaging of a system of three planets orbiting a nearby star[5], and demonstrating the existence of a massive black hole at the centre of our Galaxy by precision measurements of the orbits of stars around what seems to be an object with the mass of three million Suns[6].

Many of the optical technology developments being pursued for future telescopes and imaging instruments are aiming at solving problems in adaptive optics. Some examples include better sky coverage by use of laser 'guide stars' (reference beacons stimulated in the upper atmosphere), an enhanced field of view by multi-conjugate tomographic techniques, and better understanding of atmospheric properties by development of SLODAR (slope detection and ranging)[7]. The most challenging technology developments needed are higher-power lasers to excite artificial guide stars in the sodium layer in the mesosphere, high-speed, low-noise wavefront sensors, and large high-deformation and small high-actuator-density deformable mirrors.

An alternative method for increasing the spatial resolution of a telescope on the ground is to build an optical interferometer, as pioneered by Albert Michelson on the Hooker 100-inch telescope in 1919. Collecting light from two or more apertures spaced apart by a distance d produces spatial resolution inversely proportional to d and independent of the individual telescope aperture. For a single-aperture telescope, the spatial resolution is inversely proportional to the telescope aperture D. It is clearly much easier and cheaper to make d much bigger than D, so an interferometer can be built with higher spatial resolution, down to the order of microarcseconds. This is a standard technique at radio wavelengths, but several successful optical and infrared interferometers have now been built, the prime examples being ESO's Very Large Telescope Interferometer (VLTI) and the CHARA interferometer on Mount Wilson. Limitations for interferometers are sensitivity (limited by the combined area of the telescopes) and field of view (limited to the diffraction pattern of the individual telescope), so they will always remain complementary to large single-aperture telescopes. Building optical interferometers with baselines of tens to hundreds of metres creates many optical challenges, some of which are now being addressed by adoption of photonic technologies.

To obtain a good image, an optical or infrared interferometer needs to take light from multiple apertures, correct for phase differences by using optical path-length compensators, and then combine the beams so as to form an interferogram that can be measured with a sensitive fringe analysis camera. This is very challenging in an observatory situation, and systems are often compromised by mechanical vibration and turbulence in the optical path. The resulting systems are complex, with hundreds of optical components mounted on precision transport devices and optical benches, as shown in Fig. 3.

Much of this complexity can be removed by the use of photonic devices. A team from the Laboratoire d'Astrophysique de Grenoble, the Université Joseph Fourier, CNRS and CEA-LETI have used silica-on-silicon technology to fabricate integrated optics devices[8,9]. One of the devices uses a system of beam combiners (see Fig. 4), beam splitters and phase-shifting devices to take light from four telescopes and produce six interferometric pair-wise combinations, each consisting of four outputs shifted in phase by 90°. These four outputs can be used to extract both the amplitude and phase of the incoming light, and hence generate an interferometric image by a Fourier transform process. As we will see later, it is also possible to integrate a spectrometer into such a system to enable wavelength to be measured as well. Even more complex integrated optics systems may be made possible by new three-dimensional waveguides manufactured using femtosecond-laser direct-writing techniques[10].

F. MILLOUR, AMBER CONSORTIUM

Figure 3 | Complex bulk optics: part of the VLTI Amber instrument.

Another application of photonic devices in astronomical interferometry is modal filtering for nulling interferometry, which can be used to remove the light from a bright star with minimum scattering, when attempting to detect a much dimmer planet nearby. Also, the use of low-dispersion photonic-crystal fibres for single-mode beam transport could make much longer baselines possible.

Returning to single-aperture telescopes, many teams in Europe and North America are currently grappling with the challenges of producing conceptual designs of instruments needed to turn the ELTs into working observatories. Some of the concepts that are emerging are as big, complex and expensive as many current telescopes. A big, and therefore heavy, instrument creates stability problems, particularly when it is mounted in a way that forces it to rotate in one or more axes to track the sky.

A question now being addressed is whether we can move away from the conventional methods of building astronomical instruments, and go from massive steel and glass instruments to arrays of miniature photonic devices. If the light from the telescope can be coupled efficiently into a photonic waveguide device, we can then address several critical problems, as we can see from the following examples.

Hydroxyl (OH) emission lines in the atmosphere limit the sensitivity of infrared imagers and spectrometers, producing up to 98% of the background photons. Broadband Bragg grating devices can be tuned to reject the light in these unwanted lines[11].

Integrated spectrometers could help reduce the mass and size of instruments enormously. One possibility is to use array waveguide devices — devices that generate a differential phase shift using an array of optical waveguides of differing length and are commonly used for data channel multiplexing in telecommunications[12]. Another is the Stationary-Wave Integrated Fourier Transform Spectrometer (SWIFT)[13], where on-chip detection of the spectrum is achieved by generating a standing wave within a mirror-terminated cavity. The spectrum is measured by probing the evanescent-field standing waves within a single-mode waveguide using nanodetectors.

Such integrated spectrometers could be incorporated into a three-dimensional architecture to allow them to measure the spectrum across an image of extended objects such as merging galaxies in the same way as we now do with conventional integral field units. These are devices that use a lens, fibre or mirror array to measure an object both spatially and spectrally to make a three-dimensional spectrometer. Three-dimensional photonic spectrometers could in theory be attached to robotic deployment devices to generate a swarm of miniature instruments that could be deployed across a focal plane to measure hundreds of objects in parallel.

Other photonic devices that are planned to be deployed in future instruments are ultra-stable laser combs for wavelength calibration of high-resolution spectrometers used for radial velocity measurements of stars disturbed by planetary motions. Such instruments measure tiny shifts in the frequency of light and need very precise calibration. It has even been proposed that such highly stable instruments could make direct measurements of the tiny shifts in absorption spectra caused by the expansion of the Universe[14].

A common problem with many of these photonic devices is how to minimize losses owing to scattering, absorption and inefficient mode-coupling. It is pointless to build a 42-metre telescope and then throw away much of the light because of poor mode coupling to a photonic device. Most photonic devices developed for applications such as communications rely on single-mode propagation and are very narrow in spectral bandwidth. The problem is that astronomical signals are much more complex, ranging from the uncorrected image of a point source, which will show multiple modes and much variation in time due to atmospheric turbulence, to an adaptive-optics corrected image, which, while being much simpler, still contains several modes. Dealing with the former case, for efficient coupling there is no alternative to the use of large-diameter multi-mode fibre that may be split into many single-mode fibres, for instance, to build an OH suppression Bragg grating filter. It is clear that expanding such a device over a reasonable field of view would be very clumsy. The situation involving adaptive optics is far more favourable as it produces a point spread function close to the ideal diffraction limit, which is easier to couple. Here, an efficient mode converter can be designed[15] to couple into the single-mode photonic devices. However, it should also be remembered that if the image is pushed towards the diffraction limit by the use of adaptive optics, a conventional bulk-optics instrument can also be much smaller.

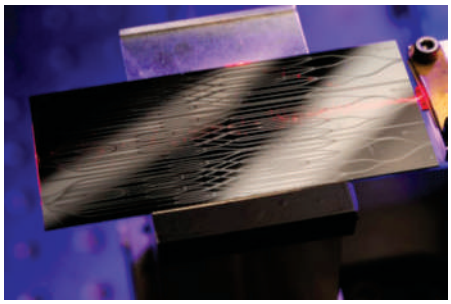

CNRS PHOTOTHEQUE / EMMANUEL PERRIN

Figure 4 | An integrated optics four-way beam combiner.

A good summary of the potential of photonics in astronomy is given in ref. 16. A coordinated research project supported by the European Union Framework 7 has just started under the OPTICON banner[17] and the OPTICON Key Technologies Network has recently updated its technology roadmap to include some of the ideas outlined here[18].

There are many challenges in building the next generation of giant optical/infrared telescopes and associated adaptive optics systems and instruments. But perhaps we are about to see another revolution in the techniques used to understand the heavens, appropriately starting in the 400th year since Galileo's revolution.

Colin Cunningham is in the UK Astronomy Technology Centre, Royal Observatory Edinburgh, Blackford Hill, Edinburgh EH9 3HJ, Scotland, UK.
e-mail: crc@roe.ac.uk

References

1. van Helden, A. *Trans. Am. Phil. Soc.* **67,** 4 (1977).
2. Tobin, W. *The Life and Science of Léon Foucault* (Cambridge Univ. Press, 2003).
3. Zuccoli, M. & Bonoli, F. (eds) *Guido Horn d'Arturo e lo specchio a tasselli* (Cooperativa Libraria Universitaria Editrice Bologna, 1999).
4. Babcock, H. W. *Publ. Astron. Soc. Pac.* **65,** 229–236 (1953).
5. Marois, C. *et al. Science* **322,** 1348–1352 (2008).
6. Gillessen, S. *et al. Astrophys. J.* **692,** 1075–1109 (2009).
7. Butterley, T., Wilson, R. & Sarazin, M. *Mon. Not. R. Astron. Soc.* **369,** 835–845 (2006).
8. Benisty, M. *et al. Astron. Astrophys.* doi:10.1051/0004–6361/200811083 (2009).
9. Labeye, P. Composants optiques intégrés pour l'interférométrie astronomique. Thesis, Inst. National Polytechnique de Grenoble (2008).
10. Thompson, R. R., Kar, A. K. & Allington-Smith, J. *Opt. Express* **17,** 1963–1969 (2009).
11. Bland-Hawthorn, J., Englund, M. & Edvell, G. *Opt. Express,* **12,** 5902–5909 (2004).
12. Bland-Hawthorn, J. & Horton, A. *Proc. SPIE* **6269,** 62690N (2006).
13. Le Coarer, E. *et al. Nature Photon.* **1,** 473–478 (2007).
14. Pasquini, L. *et al. Proc. SPIE* **7014,** 70141I (2008).
15. Corbett, J. C. *Opt. Express* **17,** 1885–1901 (2009).
16. Bland Hawthorn, J. & Kern, P. *Opt. Express* **17,** 1880–1884 (2009).
17. Allington-Smith, J. *Proc. SPIE* **7018,** 70182P (2008).
18. http://www.astro-opticon.org/networking/key_tech.html

NANOPHOTONICS

Take your vitamins

Science **323,** 1319–1323 (2009)

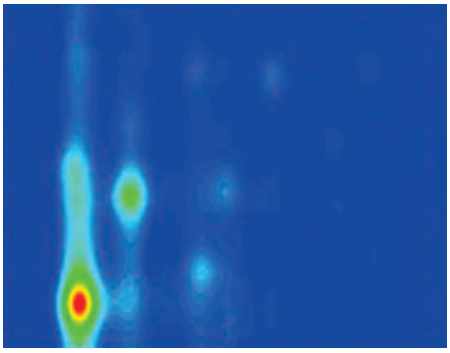

Carbon nanotubes that reliably fluoresce brightly have been fabricated by a team of researchers from the University of Connecticut. Using a chemical that mimics a cofactor of vitamin B2, Sang-Yong Ju and others have shown that they can boost the photoluminescence yield of single-walled carbon nanotubes (SWNTs) to levels as high as 20%.

The optical — in particular, photoluminescent — properties of SWNTs are important for applications ranging from optoelectronics to biological imaging and sensing. Unfortunately, fluorescence quantum yields are usually low because of quenching that arises from defects, the presence of oxygen (which adsorbs into the nanotube sidewalls) and the fact that solution-suspended nanotubes tend to group together into bundles.

Ju *et al.* show that an analogue of a solvent known as flavin mononucleotide, or FC12, can solve these problems. It arranges itself around the SWNTs to form a helical wrapper and, unlike other surfactants, its organization is tight enough to exclude oxygen from the surface of the SWNTs. The result is a boost in the quantum luminescence yield; for aggregates of SWNTs the yield increases from 0.1–1.5% to 11%, and for an individual nanotube the maximum yield rises to 20%.

PHOTOVOLTAICS

New dimension for solar cells

Science **324,** 232–235 (2009)

Solar technology will be an important part of the world's future energy picture, and flexible solar cells are attracting increased attention as they promise to be more convenient and cheaper to deploy than conventional photovoltaic devices. Scientists at Konarka Technologies in the United States have taken this flexibility to another level, by designing organic photovoltaic cells that come in the shape of a wire and offer efficiencies of around 3%.

The Konarka team uses thin metal wires as the basis for their device, so that photogenerated electrical current can be carried over long distances. One wire, made of stainless steel, is coated with a photoactive layer made from a conducting polymer and fullerene derivative. The two phases form intertwined, worm-like domains that yield a high surface area and boost the efficiency of electron collection in the device. A second wire, which is coated with a silver film, serves as the counterelectrode and is wrapped around the first. Both electrodes are encased in a transparent polymer cladding, which focuses incoming light onto the photovoltaic layer even when it is completely shadowed by the counterelectrode. Compared with previous organic-based fibre photovoltaic devices, which are less than 1% efficient, this dual-wire design offers efficiencies ranging from 2.8 to 3.3%.

MICROSCOPY

Steady as she goes

Nano Lett. **9,** 1451–1456 (2009)

Atomic force microscopy (AFM) is a well-established technique, but unwanted mechanical drift between the probe tip and sample remains a critical and largely unaddressed issue. This drift can limit the stability of the AFM tip over a precise sample location and degrades registration, making it harder for the probe to return to a particular location.

Gavin King and colleagues have published a technique that addresses these challenges. By scattering focused laser beams off the apex of a commercial AFM tip, they show that it is possible to measure and control the three-dimensional position of the tip to within 40 pm. With this increased stability — which can be achieved with submilliwatt laser power — there is no need to scan rapidly while imaging, and the signal-to-noise ratio is improved by a factor of five.

Using a series of AFM images of transparent substrates, the authors demonstrate atomic-scale tip-to-sample stability (of the order of 100 pm) and registration over tens of minutes. Unlike previous efforts to improve AFM tip-to-sample control, the technique can be used in air at room temperature, and does not require a cryogenic or ultrahigh-vacuum environment.

QUANTUM OPTICS

Sensitive soul

Phys. Rev. Lett. **102,** 10301 (2009)

Sensitivity is the name of the game for gravitational-wave detectors. Scientists in Paris have studied how the quantum effects of radiation pressure — the mechanism by which light exerts pressure on any surface it comes into contact with — could affect the pursuit of these elusive gravitational waves.

Verlot and co-workers measure radiation-pressure-induced correlations between two optical beams sent into a moving mirror cavity. The first beam — an intense signal beam — causes the mirror to move by means of radiation pressure. A weaker second beam called the meter beam monitors the position fluctuations of the mirror. Because the intensity fluctuations of the signal are unchanged on reflection from the mirror, and the radiation pressure exerted by the weak beam is negligible, the intensity–phase correlations between the two reflected beams offer a direct measurement of radiation-pressure effects.

For the technique to work, losses and thermal variations have to be extremely low. The cavity, which uses a fused silica mirror, has a finesse of 330,000 and is operated in vacuum to increase its mechanical quality factor. The authors are able to detect weak correlations between the signal and meter beams at a quantum level, an advance that could benefit the fields of precision metrology and quantum optics.

BIOPHOTONICS

Pinning down proteins

Nano Lett. **9,** 1598–1603 (2009)

Researchers in the United States have devised a single-molecule technique that uses quantum dots to pinpoint the location of proteins bound to DNA. The method could be used to study DNA such as viral genomes or bacterial or mammalian genome fragments.

Transcription factors are one example of DNA-binding proteins, and the ability to identify their exact position and occupancy is important for gaining insights into cell processes such as gene expression and regulation. Ebenstein and co-workers perform a proof-of-principle experiment that uses far-field optics to probe a linear array of viral DNA strands to which RNA polymerase proteins are bound. The virus in question is T7, which infects most *Escherichia coli* strains.

Imaging is performed using fluorescence. In practice, four to six different transcription factors can be labelled with different quantum dots that emit in the visible and can be spectrally separated from one another. Strands of DNA are stretched out on glass slides in linear arrays, and a single light source is used to induce light emission. The researchers are able to pin down the position of multiple proteins on long stretches of DNA — spanning tens to hundreds of kilobases (1 kilobase is equal to 1,000 base pairs) — offering promise of a high-throughput analysis technique. Eighty-seven per cent of quantum dots are located to an accuracy of one kilobase.

IMAGING

In a squeeze

Phys. Rev. Lett. **102,** 103902 (2009)

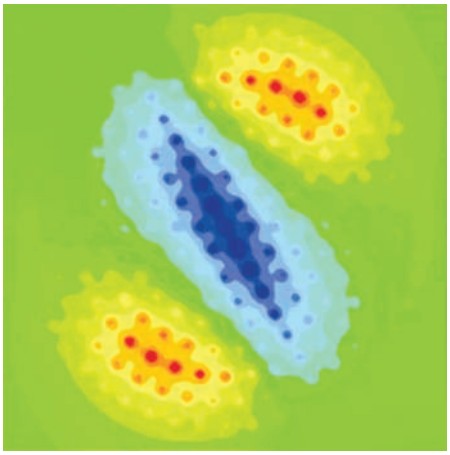

Complicated images can be pushed through tiny subwavelength holes without losing any of their fine detail, according to Mário Silveirinha and Nader Engheta. Their studies suggest that this is possible even when the hole has a diameter that is considerably smaller than the size of the image.

Overcoming diffraction typically involves metamaterials or plasmonic effects. In contrast, Silveirinha and Engheta suggest sampling an image 'pixel by pixel' using an array of parallel nanowires, then 'squeezing' the electric current associated with each pixel through a tiny hole, with essentially no reflection. In their proposal, a bundle of 217 metallic nanowires is squeezed through a tiny hole (about 2 μm in diameter) in an opaque metallic screen. To ensure that the energy associated with each image pixel is transmitted and not reflected, the screen and hole are embedded in a block of low permittivity — in this case, silicon carbide, which has a near-zero permittivity near the design wavelength of 10.3 μm.

Despite the subwavelength dimensions of the hole, even a complicated image can be reproduced accurately on the other side of the screen. Such an imaging system could potentially open the door to unprecedented manipulation of electromagnetic fields on the nanoscale.

OPTOFLUIDICS

Thin ice

Appl. Phys. Lett. **94,** 113901 (2009)

Optical tweezers are a well-known example of using light to control matter remotely. However, the idea of harnessing light to manipulate fluids rather particles — the principle of optofluidics — is also proving popular. Scientists have now shown that a moving laser spot focused onto a thin ice sheet can create fast-action microchannels useful for pushing other molecules along.

Weinert *et al.* scan an infrared laser beam across a micrometre-thick ice sheet. The ice melts at the laser spot and freezes behind it, and, as a result of the difference in specific volume, fluid flows inside the molten ice along the direction of the laser beam. The melting transition dynamics are such that ice can be pumped along freely defined patterns (in this case channels 25 μm wide and 3 μm deep) at velocities of up to 50 mm s^{-1}.

The authors demonstrate their mechanism by pumping fluorescent dye molecules across an ice–ice interface. By using an ice sheet as the channelling medium instead of water, the resulting thermoviscous pumping is three orders of magnitude faster. The diffusion limitation of ice means that dissolved molecules can be controlled without the need for pre-defined channels, valves or external pumps.

SILICON PHOTONICS

Round the bend

Opt. Express **17,** 4752–4757 (2009)

Low-loss silicon waveguides are critical for on-chip optical networks. But as with many technological challenges, the engineering approaches usually involve trade-offs: low losses but large bending radii (as with ridge waveguides), or small bending radii and higher losses (as with strip waveguides).

Now, scientists at Cornell and Harvard Universities have come up with efficient silicon waveguides that offer the best of both worlds. Their waveguides, based on a silicon-on-insulator wafer with a device layer of 500 nm and a 3-μm-thick buried oxide layer, are made in an etchless procedure whereby the silicon is never exposed to the etching plasma. In place of etching, Jaime Cardenas and colleagues choose a selective oxidation method, which results in ultra-smooth sidewalls with width variations of 0.3 nm and losses of just 0.3 dB cm^{-1} at a wavelength of 1.55 μm. The technique reduces bending losses to 0.007 dB per bend for a right-angled bend with a 50-μm bending radius.

LASER SCIENCE

Bumpy ride

Opt. Express **17,** 5058–5068 (2009)

Lasers are useful for engineering glass surfaces that are difficult to mould or emboss. Carbon dioxide lasers are usually the tool of choice, but feature heights are limited to several micrometres because the absorption depth at their wavelength (around 10.6 μm) is small relative to the glass thickness.

Richard Grzybowski and colleagues have shown that by using different lasers, larger features are possible and bumps 100 μm or taller can be grown on glass. In place of a carbon dioxide laser, they use near-infrared lasers — an 810-nm pigtailed diode laser and a 1,550-nm fibre laser. Whereas light from a carbon dioxide laser couples to phonon oscillations in the glass, near-infrared laser light couples by an electronic absorption mechanism, meaning that the penetration depth can vary from several tens of micrometres to several millimetres.

The resulting laser-induced bump can reach 10–13% of the overall glass thickness and depends on the glass base composition. In the case of doped borosilicate glasses, the swelling is reversible, and the bump height can be increased or decreased depending on whether consecutive laser pulses have higher or lower energy than previous ones. Grzybowski *et al.* suggest that this approach to glass swelling could be used to make tightly packed arrays of tiny lenses with varying numerical apertures, or to perform very precise alignment of micrometre-sized components.

ANTIMATTER

Abundant positron production

Researchers at Lawrence Livermore National Laboratory have generated billions of positrons, forming the highest antimatter densities ever created on earth, by using superintense short laser pulses.

Carsten Müller and Christoph H. Keitel

In 1928, Dirac postulated the existence of antimatter on the basis of his relativistic quantum-mechanical wave equation. Four years later, Anderson identified the positron, the antiparticle of the electron, in cloud-chamber analyses of cosmic rays. Since then, antimatter has constituted an essential part of our understanding of the fundamental laws of physics, and has always represented a driving force for scientific research, leading to the formulation of quantum field theory and its experimental verification in particle accelerators of ever-increasing dimensions. There exists a perfect symmetry between matter and antimatter, at least according to our present understanding. Today, positron research extends over diverse fields, ranging from particle physics and astrophysics to tomographic applications in medicine. But corresponding experimental studies often necessitate large numbers of positrons that are difficult to supply: positrons usually arise in modest quantities only, and then annihilate quickly on a nanosecond timescale when brought into contact with matter.

Chen *et al.* at Lawrence Livermore National Laboratory (LLNL) have now succeeded in generating copious amounts of positrons[1]. After illuminating a millimetre-thick gold target with short, ultra-intense laser pulses, the researchers detected more than 1 million positrons, implying that in total around 100 billion electron–positron pairs were created in the material at previously unsurpassed densities of 10^{16} cm^{-3}. This enormous output substantially exceeds the positron yields generated in the laboratory by any other means.

The conversion of high-energy photons into electron–positron pairs is a known phenomenon. The required photon energy scale is determined by the rest energy of the pair, which is about 1 MeV. For instance, an MeV photon may decay into an electron–positron pair in the neighbourhood of an atomic nucleus whose presence is required to absorb recoil momentum. This fundamental process was first calculated by Bethe and Heitler in the early days of relativistic quantum mechanics[2].

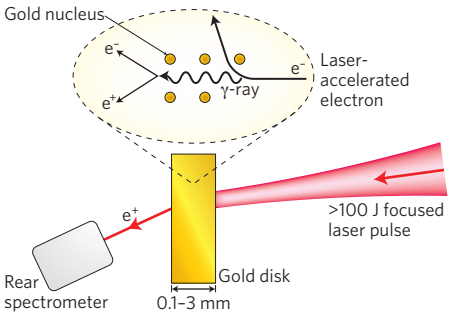

Figure 1 | Experimental set-up and, in the enlarged region, the underlying physical mechanism for pair creation.

Later, it was confirmed experimentally by using energetic bremsstrahlung — that is, gamma-rays produced by acceleration of a charged particle — from synchrotron sources or nuclear gamma-rays. In the following year, the Bethe–Heitler mechanism has been used for positron production by shooting energetic electrons from a linear accelerator onto a moderator with a high nuclear charge number.

At first sight, it is not obvious how optical laser photons with energies in the electronvolt range could be related to the generation of electron–positron pairs. The different energy scales, being separated by six orders of magnitude, seem to exclude any connection. However, electric field intensities in excess of 10^{20} W cm^{-2} can nowadays be produced by ultra-short laser pulses of femtosecond or picosecond duration. When such an ultra-intense laser pulse impinges on a solid target, a hot plasma can be formed. Owing to rather complex collective dynamics, a plasma wake emerges in which electrons are accelerated to high kinetic energies in the mega- or even gigaelectronvolt domain[3]. The fast electrons collide violently with the plasma ions giving rise to the emission of bremsstrahlung which may be converted to electron–positron pairs through the Bethe–Heitler reaction (see Fig. 1). This indirect pair-production mechanism by means of relativistic laser–solid interaction can be extremely efficient, as demonstrated by the LLNL experiment[1]. It used a Nd:glass laser system based on an optical parametric chirped-pulse amplifier (OPCPA) producing, twice per hour, ultra-intense short pulses (~10^{20} W cm^{-2} for 1 ps) with a near-infrared wavelength of about 1 μm and total energies exceeding 100 J. The pulses were incident at an 18° angle on a solid gold disk with a diameter of 6 mm and a variable thickness of up to 3 mm. Two spectrometers of high energy coverage and resolution at the target front and rear sides detected numerous hot positrons (and electrons) within a narrow angular range, corresponding to ~10^{10} particles per steradian. The positrons reaching the detectors represent only a small portion of the total amount produced because the bulk part is trapped in a small volume (~10^{-5} cm^3) inside the target where the highest concentrations of MeV positrons ever created in the laboratory are reached. The record was accomplished by optimizing the target and beam design and their interaction geometry, in comparison with earlier pioneering studies at LLNL[4] and the Max Planck Institute for Quantum Optics using a table-top set-up[5]. Whereas in those experiments some 100 positrons were detected, vastly more antiparticles were observed in the present measurement because of the ultra-high laser pulse energies (as compared with 200 mJ in ref. 5) and the large target thicknesses (as compared with paper-thin targets in ref. 4). The latter feature is also responsible for the dominance of the Bethe–Heitler process over competing pair-creation mechanisms.

Chen and co-workers anticipate average positron production rates of 10^9 s^{-1} sr^{-1} using future high-power laser sources of high repetition frequency (several shots per second), which would be competitive with existing positron sources based on β^+-radioactive ^{22}Na nuclei (see ref. 1). These conventional devices provide positrons with typical energies between 100 and 500 keV at an intensity that is constant over long periods owing to the ^{22}Na lifetime of 2.6 years. After its β^+-decay, the nucleus stabilizes by emission of a 1.3-MeV

gamma-ray photon. Laser-based positron sources offer complementary properties as the particles are generated in ultra-short bursts with the positron energy, emission angle and intensity variable through variation of the external parameters. Thus, lasers may produce positron flashes within a specified energy range on demand. Radiation protection (from nuclear, bremsstrahlung and annihilation gamma-rays) is required in both cases.

The first observation of laser-induced electron–positron pair creation came in the late 1990s at the Stanford Linear Accelerator Center[6]. It also applied ultra-intense picosecond laser pulses, which, however, were not used to accelerate electrons. Rather, they participated directly in the pair creation step when brought into collision with a 46-GeV electron beam which was generated by conventional acceleration means. The experiment observed about 100 positrons produced through a nonlinear variant of a Bethe–Heitler-type reaction, where, on the beam collision, several (around five) laser photons were absorbed at once to create an electron–positron pair. Similarly, nonlinear Bethe–Heitler production of muon–antimuon pairs may also come into reach by using near-future X-ray laser devices in conjunction with a powerful ion accelerator such as the Large Hadron Collider at CERN[7].

Although representing an impressive technical achievement on its own, the LLNL experiment more importantly offers a new route towards the generation of high-density positron samples, which are of paramount interest for so many current research activities. For example, serious efforts are being spent in putting the charge–parity–time (CPT) theorem experimentally to the test. This cornerstone of the Standard Model of particle physics goes back to Pauli (and others) in the 1950s, and says that the combined discrete transformations of charge conjugation (that is, interchange of particles with antiparticles), parity and time reversal leave the physical laws unchanged. Although there is no experimental evidence yet for a violation of this symmetry, physicists are searching for it as it might explain the apparent imbalance between matter and antimatter observed in the Universe, which represents one of the greatest cosmological mysteries today. The ATHENA[8] and ATRAP[9] collaborations, for instance, are heading for laser-spectroscopic precision measurements on atomic transitions in antihydrogen at CERN's antiproton decelerator facility. A comparison with the extremely accurate hydrogen data holds the potential for revealing even a tiny CPT violation. A main obstacle for these studies is the generation of sufficient numbers of low-energy positrons (and antiprotons) allowing for the required level of precision. It is interesting to note that the LLNL scheme of positron production could be incorporated into the future Facility for Antiproton and Ion Research (FAIR) at GSI in Darmstadt, Germany[10]. Starting in 2014, it will host the most brilliant source of antiprotons and may additionally use the petawatt-class laser system PHELIX which is already operational there.

Another important application of intense positron sources is the generation of very dense targets of cold positronium (Ps) atoms, the hydrogen-like bound state of an electron and a positron. The first production of di-positronium (Ps_2) molecules has recently been achieved[11], and the intended formation of a Ps Bose–Einstein condensate is likely to require positronic densities of ~10^{18} cm^{-3}, which are so far unavailable. Similar needs exist for the realization of a 511-keV annihilation gamma-laser. Our understanding of various astrophysical phenomena such as gamma-ray bursts or black-hole evaporation dynamics could also greatly benefit from experiments on dense hot electron–positron plasmas.

Several technical challenges remain to be overcome, of course, such as the complete extraction of the dense positron cloud from the target material and, if desired, the deceleration and cooling of the positrons for subsequent formation and trapping of cold antihydrogen or positronium atoms. But still, ultra-strong lasers (in particular when table-top in size) may develop into relatively cheap and compact antimatter factories that could find applications in a wide range of scientific areas. ❐

Carsten Müller and Christoph H. Keitel are at the Max Planck Institute for Nuclear Physics, Saupfercheckweg 1, 69117 Heidelberg, Germany.
e-mail: c.mueller@mpi-k.de, keitel@mpi-k.de

References

1. Chen, H. *et al. Phys. Rev. Lett.* **102,** 105001 (2009).
2. Bethe, H. A. & Heitler, W. *Proc. R. Soc. Lond. A* **146,** 83 (1934).
3. Leemans, W. P. *et al. Nature Phys.* **2,** 696–699 (2006).
4. Cowan, T. E. *et al. Laser Part. Beams* **17,** 773–783 (1999).
5. Gahn, C. *et al. Appl. Phys. Lett.* **77,** 2662–2664 (2000).
6. Burke, D. *et al. Phys. Rev. Lett.* **79,** 1626–1629 (1997).
7. Müller, C. *et al. Phys. Rev. Lett.* **101,** 060402 (2008).
8. Fujiwara, M. C. *et al. Phys. Rev. Lett.* **101,** 053401 (2008).
9. Gabrielse, G. *et al. Phys. Rev. Lett.* **89,** 213401 (2002).
10. http://www.gsi.de/fair/
11. Cassidy, D. B. & Mills, A. P. Jr *Nature* **449,** 195–197 (2007).

LASER PHYSICS

Random lasers explained?

Random lasers can be made simply by grinding a laser crystal and optically pumping the resulting powder. The physics behind the resulting laser emission is rich but has led to much controversy. New experiments may now settle the debate behind their operation.

Diederik S. Wiersma

The Maxwell equations often allow accurate prediction of optical phenomena, and it is then just a matter of reproducing the right conditions in the laboratory to confirm the theory. But sometimes a new phenomenon is observed that at first seems incomprehensible and proves difficult to model theoretically. This is precisely what has happened in the case of random lasing, a recently observed phenomenon in which laser light can be generated from strongly scattering substances such as fine powders, translucent ceramics and dye-doped microporous glass[1]. Although it has been clear from various experiments that one can generate coherent laser light from these materials, few people agreed on how this was possible. The main points of contention were how random structures could sustain optical modes and what the character of such modes should be. The various physical mechanisms that were proposed for explaining random lasing could be divided into two categories, namely those predicting spatially confined (localized) optical modes and those predicting extended modes that covered a large

volume of the sample. This led to agitated discussions among research groups about the validity of the available models.

Now Fallert *et al.* report[2] on page 279 of this issue an experiment that may have solved this controversy once and for all. They measured the local emission spectra from random laser samples and studied the spatial extent of random laser modes. The results are surprising: both points of view seem to be correct. They found that in a sample, it is possible to observe both extended and localized modes. Random laser emission is normally highly multimode, meaning that several sharp spectral peaks corresponding to the various modes are observed simultaneously. (In certain experimental conditions, for instance when the number of modes is very large and several emission pulses are averaged, these sharp peaks can be averaged out, leading to a smooth spectrum.) By measuring local emission spectra, Fallert *et al.* were able to map the modes of their sample and thereby know their spatial extent. A previous attempt[3] to measure this was not conclusive because the sample was excited only locally, exactly where the spectra were taken. This intrinsically excluded the build-up of extended modes. Fallert *et al.* solved this by probing locally, but at the same time exciting the entire sample.

Before going deeper into the various models of random lasing, let us address the question of how it is possible to have laser emission from a powder in the first place. How can one obtain coherent light without an optical cavity? To understand this, let us recall briefly how a regular laser works. A laser contains an element that can provide optical gain by stimulated emission, for instance a laser dye that can be excited. A cavity is then used to trap the light in this gain medium, and lasing occurs when the total amplification becomes larger than the losses. The resulting light emission is spectrally narrow and coherent, meaning that the intensity fluctuations are suppressed (or, in quantum optical terms, the photons in a coherent light beam are less bunched than those from a chaotic source). It is, however, not the cavity as such that creates this coherence, but the saturation of the gain. When the gain is saturated, the intensity simply cannot grow further and hence the intensity fluctuations are suppressed. This condition can easily be achieved in powders in which light is multiply scattered and amplified by stimulated emission, which is the reason that random lasers can emit coherent light without a cavity. The modes provide the wavelength selection in a laser, and, in the case of a random laser, one must therefore consider the optical modes of the random dielectric structure.

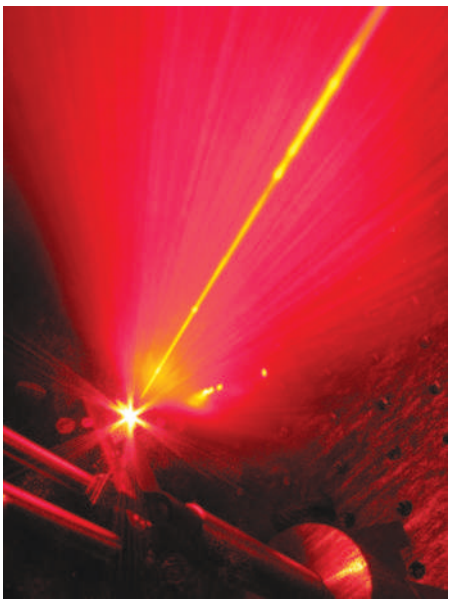

DIEDERIK S. WIERSMA.

Figure 1 | Light scattered by a random laser material. The emission is clearly polydirectional. In the red emission pattern, lines are visible, corresponding to maxima in the angular distribution of the intensity (speckle spots).

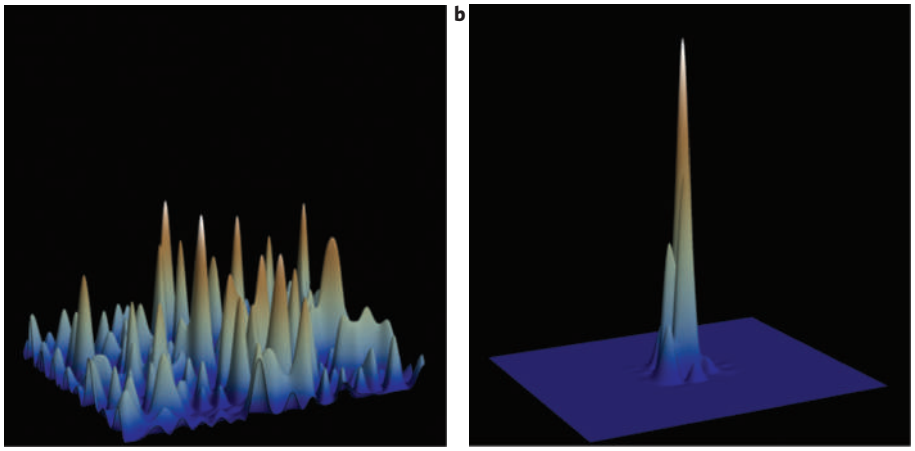

DIEDERIK S. WIERSMA.

Figure 2 | Intensity distributions. **a**, An example of the spatial distribution of the intensity inside a random dielectric structure. The maxima and minima are due to interference between multiply scattered waves. **b**, In extremely strongly scattering materials a phenomenon known as optical Anderson localization can set in, in which case the spatial distribution of the intensity becomes confined to a small region of space.

Multiple scattering of light in disordered structures leads to very complex electromagnetic mode structures. In certain directions the interference between scattered waves will be constructive, leading to maxima in the intensity in those directions. The resulting spatial intensity pattern is that of laser speckle (Fig. 1), an effect that most people in optics know as the grainy pattern that is observed when a laser beam is reflected from, for example, a diffusive plate. The intensity distribution of the light at one specific wavelength inside a random structure shows the same type of distribution: it fluctuates strongly from point to point but covers a large area of the sample. A typical extended mode of a random dielectric structure is shown in Fig. 2a. In extremely strongly scattering materials an additional interference effect known as Anderson localization of light[4] can occur. In analogy to Anderson localization of electrons, this effect leads to highly confined photonic modes (Fig. 2b).

The first observations of narrow peaks in random laser spectra were explained in terms of Anderson localization[5]. The idea of localized modes is attractive as it reintroduces the concept of a (random) cavity. However, Anderson localization is difficult to achieve because of the extreme scattering that it requires. Only a few, very strongly scattering materials so far have shown experimental signatures of localization. Random lasing, on the other hand, has been observed from a broad scale of more modestly scattering materials. Alternative explanations were therefore proposed[6–8] to explain the observations of coherent and narrow-banded random laser emission from such materials. These models are based on the (extended) speckle modes that can occur in all translucent optical materials. In extended modes the intensity can build up to very high levels before the gain is depleted. Another point of interest is that the degree of coupling of a mode to its environment has an important influence on the mode lifetime and therefore its quality factor. In particular it was shown by Apalkov *et al.*[6] that one can have a high quality factor because a particular mode is only weakly coupled to its environment and light

therefore remains trapped inside for a longer time.

Fallert *et al.* made their measurements on samples of zinc oxide powder which are strongly scattering and in which, therefore, Anderson localization is not excluded. Zinc oxide was also one of the first materials in which random lasing was observed[9] and this was the trigger for today's debates regarding the nature of localization in such systems. Fallert and co-workers observed that both spatially localized and extended modes exist at the same time in zinc-oxide-based random lasers. The extended modes are found to be dominant in the central region of the gain curve where the gain is highest, and the spatially confined modes prevail in the lower-gain regions. Because the confined modes have a longer lifetime, they are the only modes that can lase in the low-gain region. On the other hand, the extended modes win the mode competition at the high-gain wavelengths because they can grow much higher in intensity before the gain is depleted.

While performing their experiments, Fallert *et al.* also observed another fascinating effect: the large samples showed huge shot-to-shot fluctuations due to a chaotic behaviour similar to that of regular lasers in which a large number of modes are coupled. The effect is very characteristic for random lasers around laser threshold, as the number of modes is usually very high and the coupling between modes is strong, particularly for the case of spatially extended modes that have a large spatial overlap. The result is that after each excitation shot, the random laser can lase in different modes and therefore at different wavelengths[10]. This behaviour has several very interesting fundamental aspects but was hampering the spatial mapping of modes that the researchers wanted to perform. Hence they used a trick to eliminate these shot-to-shot fluctuations: by limiting the sample volume they greatly reduced the number of modes that the sample could sustain.

Where do these observations leave us as far as the physics of random lasing is concerned? Fallert *et al.* convincingly show that the spatial extent of modes can be confined or extended. This outcome does not favour one specific random laser model; on the contrary, it is consistent with extended, localized and other types of modes. The fascinating and surprising aspect of these results is that such modes apparently are able to coexist in the same sample. The balance between gain, gain saturation and mode lifetime seems to determine which modes finally dominate. The existing models therefore do not seem to be wrong but incomplete, and the theoretical challenge has now become that of including crucial concepts such as the dynamics of the system and the saturation of the gain. It is fascinating to see how relatively simple materials such as amplifying powders can give rise to so much discussion and such intricate physics. ❐

Diederik S. Wiersma is at the European Laboratory for Non-Linear Spectroscopy, University of Florence, and INFM-CNR, Via Nello Carrara 1, 50019 Sesto-Fiorentino (Florence), Italy.
e-mail: wiersma@lens.unifi.it

References

1. Wiersma, D. S. *Nature Phys.* **4,** 359–367 (2008).
2. Fallert, J. *et al. Nature Photon.* **3,** 279–282 (2009).
3. van der Molen, K. L., Tjerkstra, R. W., Mosk, A. P. & Lagendijk, A. *Phys. Rev. Lett.* **98,** 143901 (2007).
4. John, S. *Phys. Rev. Lett.* **53,** 2169–2172 (1984).
5. Jiang, X. Y. & Soukoulis, C. M. *Phys. Rev. Lett.* **85,** 70–73 (2000).
6. Apalkov, V. M., Raikh, M. E. & Shapiro, B. *Phys. Rev. Lett.* **89,** 016802 (2002).
7. Mujumdar, S., Ricci, M., Torre, R. & Wiersma, D. S. *Phys. Rev. Lett.* **93,** 053903 (2004).
8. Vanneste, C., Sebbah, P. & Cao, H. *Phys. Rev. Lett.* **98,** 143902 (2007).
9. Cao, H. *et al. Phys. Rev. Lett.* **82,** 2278–2281 (1999).
10. Sharma, D., Ramachandran, H. & Kumar, N. *Opt. Lett.* **31,** 1806–1808 (2006).

DISPLAYS

Microfluidic electronic paper

Pigmented inks in a microfluidic structure provide a new approach for fabricating bright, colourful electronic paper with a reflectivity of greater than 50%. The challenge now is to combine the scheme with fully functioning drive electronics.

Paul Drzaic

Flat-panel electronic displays are a ubiquitous feature in modern society. Entire product categories in mobile electronics, including smart phones, electronic books and media players, could not exist without an integrated display. Displays are also a huge business: in terms of area, the fabrication capacity worldwide is about 1 m^2 of electronic displays every second, and it serves as the basis of an industry worth around 100 billion US dollars[1]. Nearly all electronic display applications are dominated by variations on a single technology: the backlit active-matrix liquid-crystal display (AMLCD). These displays are beautiful, inexpensive and engineered to a high degree of sophistication[2].

Despite this dominant position, the AMLCD falls short in many ways compared with that other ubiquitous display medium, ink on paper. Paper is superior to AMLCDs in properties such as general readability (particularly in sunlight), colour gamut, viewing angle, flexibility, power consumption and cost. There is substantial effort worldwide to develop electronic paper that combines the desirable properties of an electronic display with the benefits of paper. Nevertheless, no technology has yet met that goal. Entering the fray is a promising approach described by Heikenfeld *et al.* on page 292 of this issue[3], that uses an electrofluidic structure to generate a high-brightness display in a scalable device structure. Their electrofluidic display makes use of the motion of an aqueous ink to cover or uncover a reflective surface, and shows potential for high brightness, good colour and video-rate operation.

It is generally agreed that electronic paper should be a reflective display technology that operates with ambient light. The need for an internal backlight is the main source of power consumption in an AMLCD, and the mismatch in luminance between a backlit display and ambient lighting is a source of eyestrain when displays are used for long periods. A sensible approach is to develop a reflective frontplane technology (an electro-optical effect to modulate light) that is compatible with ambient light and existing AMLCD backplane technology (the millions of thin-film transistors on glass sheets that are used to control each individual pixel and that the display industry builds so well). Conventional liquid-crystal

technologies are not particularly bright when used in reflective mode displays, as the need for a polarizer robs the display of over half the available light before other losses are even considered.

In fact, a number of different display technologies have been developed that offer monochrome paper-like reflectivities and viewing angles, and are compatible with backplane technologies used in AMLCDs. The micro-encapsulated electrophoretic display technology[4] of E Ink Corporation has been the most successful so far, appearing in products such as the Amazon Kindle. Nevertheless, neither the electrophoretic technologies nor other competing approaches have successfully achieved two highly desirable properties: bright, saturated colour and greyscale similar to print, and video rate speed of operation. Bright, saturated colour is particularly challenging in a reflective display, owing to the usual architecture of a flat-panel display (Fig. 1).

The display cell described by Heikenfeld *et al.* makes use of a three-dimensional microfluidic structure, combined with pigmented inks and bright reflectors. The microfluidic cell is designed to contain a narrow but deep reservoir for the ink, coupled to a thin surface channel several hundred micrometres in length. A bright reflector made from aluminium covers the pixel, and because the reservoir subtends only a relatively small area (5–10% of the pixel), the viewer sees mostly the reflector when the ink is in the reservoir. Laplace–Young pressure (similar to the forces that wick fluids into a capillary) keeps the pigmented ink hidden. When a voltage is applied across the pixel, dielectric forces pull the ink from the reservoir and spread it across the pixel. This electrowetting effect covers the reflector with the pigment, changing the colour of the pixel. Once the voltage is removed, the Laplace–Young pressure forces the pigmented fluid to retract to the reservoir.

It is interesting to compare this system with the other main fluid-based display system, the electrowetting display pioneered by Liquavista[5]. That display relies on a hydrophobic surface causing a coloured oil to wet a pixel uniformly, hiding the reflector underneath. Applying a voltage causes a colourless water solution to displace the coloured oil and force it to the pixel edges, making the reflector visible. At present, the relative reflectivity values of the two systems are comparable, with each reporting pixel-level reflectivities greater than 50%. The Liquavista display currently has the edge in response time[6], with a reported switching speed of less than 10 ms for the application

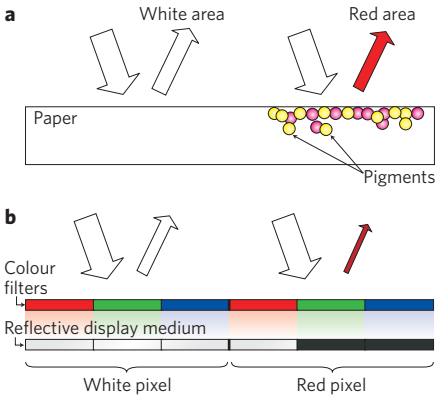

Figure 1 | How ink on paper generates colour, compared with a reflective electronic display. **a**, For ink on paper, white is generated by the absence of ink. Colour is generated by overprinting pigments onto the desired area; a red colour is generated by printing a combination of yellow and magenta pigments. **b**, For a simple reflective display, an individual pixel usually consists of three subpixels, each with a different colour filter (red, green or blue) over a voltage-controlled element that reflects strongly, or absorbs strongly. For white, the display element reflects strongly, but because each colour filter element only transmits 1/3 of the available light, the overall white state is not very bright. For a colour such as red, the display material under the red colour filter is bright, but the other elements are dark, leading to a coloured state that is coloured but not very bright.

of 15 volts, compared with the response time here of 50 ms at 12 volts. Calculations by Heikenfeld *et al.* for their electrofluidic display, however, point to the potential for a white reflectivity of 85% and a response time of about 1 ms by optimizing the microfluidic geometry and shrinking the pixel size. These properties would lead to substantial improvement in colour filter-based displays; although the display still would not have the same brightness and saturation as ink on paper, it could be a considerable step up from what is available today.

Another promising aspect of the design by Heikenfeld *et al.* is its relative simplicity. Hayes *et al.*[7] have proposed electrofluidic structures that use a non-visible reservoir behind the pixel, and a thin electrowetting channel to pull the colour fluid into the visible region. That approach, though, uses a multi-level structure that seems to require multi-step fabrication processes. In contrast, the three-dimensional structure described here by Heikenfeld *et al.* forms the mesa, channels and reservoir with a single photolithographic step, a great advantage in low-cost, high-yield fabrication.

Inevitably, caution is needed when evaluating new display technologies, and this technology is no exception. Full-colour operation has not yet been demonstrated, either with colour filters or using pigments with multiple colours. Another need is for the demonstration of reproducible and uniform greyscale, either through analogue driving signals or through pulse-width modulation. This greyscale response must be well behaved to allow accurate switching between grey levels without a reset pulse (for analogue video), or fast enough not to introduce artefacts for pulse modulation video. Video-rate colour performance with greyscale is the most prominent combination of features lacking in existing demonstrations of electronic paper technology, and it will be a key test for any new technology that desires to be seen as true electronic paper.

Other needs include compatibility with some form of manufacturable active-matrix backplanes for driving the pixels. Conventional glass-based thin-film transistors used in today's AMLCDs are perhaps the most obvious approach, but emerging flexible backplanes made from organic semiconductors, amorphous silicon or metal oxides could be another option. To be a success, the technology must be able to provide a high level of reproducibility across millions of pixels across a display face, and be stable for years and for at least millions of switching operations. Plastic cell construction and, even better, flexibility are also desirable features. Finally, it needs to be recognized that competing technologies are also improving their performance all the time, and that incumbent technologies like AMLCDs get better, cheaper and more entrenched every year.

Nevertheless, the high reflectivity, intense colouration and relatively simple fabrication process seen in this first attempt is impressive. The approaches described for improving brightness, developing greyscale and improving response time are sensible. The desire for the ultimate display material, electronic paper, is strong. Welcome to the fray. ❐

Paul Drzaic serves as a consultant to industries involved in electronic displays, materials science or nanotechnology, through Drzaic Consulting Services, 506 Calle Florencia, Morgan Hill, California 95037, USA.
e-mail: drzaic.consulting@gmail.com

References

1. www.displaysearch.com
2. Lee, J. H., Liu, D. N & Wu, S. T. *Introduction to Flat Panel Displays* (Wiley, 2009).
3. Heikenfeld, J. *et al. Nature Photon.* **3,** 292–296 (2009).
4. Johnson, M. T. *et al. J. Soc. Inf. Display* **14,** 175–180 (2006).
5. Hayes, R. A. & Feenstra, B. J. *Nature* **425,** 383–385 (2003).
6. Feenstra, B. J. *et al. J. Soc. Inf. Display* **12,** 293–299 (2004).
7. Hayes, R. A., Feenstra, B. J. & Massard, R. M. Display device. US patent 7,359,108 (2008).

CONDENSED-MATTER PHYSICS

Transparent sodium

One of the best-known features of metals is that they are usually opaque and reflect visible light. But now it seems that huge pressures comparable to those at the centre of the Earth can change everything. Yanming Ma of Jilan University in China, and colleagues from Switzerland, Germany, Russia and the United States, have demonstrated (*Nature* **458,** 182–185; 2009) that sodium becomes transparent to visible light at pressures of about 200 GPa (about two million atmospheres), and Matsuoka and Shimizu (*Nature* **458,** 186–189; 2009) have observed a 10,000-fold increase in the electrical resistance of lithium at 80 GPa.

The key to this feat is to compress metals into a new phase in which valence electrons are held hostage in pockets formed between now overlapping atomic cores. The 'metals' are no longer metals, but more like a semiconductor or dielectric.

Metals are usually thought of as a lattice of positively charged atomic cores surrounded by a sea of free electrons that form an electronic plasma. If light striking the metal has a longer wavelength than the plasma wavelength — corresponding to the resonant frequency of oscillation of the collective sea of electrons — the photons do not propagate within the metal, because the light's energy is drained into oscillation of the plasma, and the light is efficiently reflected. This is how all metallic mirrors work, and sodium and lithium are described well by this free-electron model under normal circumstances. At very high pressures, however, it now seems that the situation changes utterly.

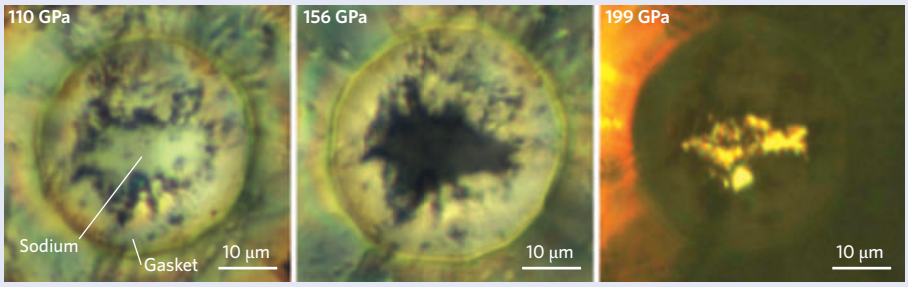

To achieve giant pressures, Ma's team clamped sodium with a metallic rhenium gasket between diamond anvils. Up to 100 GPa, the sodium showed the standard body-centred cubic phase, then passed through various other opaque phases (face-centred cubic, cI16, oP8 and tI19) before reaching a state of particular interest about 200 GPa. Photographs taken through the diamond anvil show that whereas sodium is typically a white metal at pressures below 110 GPa, it turns black at 130 GPa and becomes transparent at around 200 GPa.

The researchers could not definitively determine the structure of the new phase at 200 GPa, but theory corroborated by Raman spectroscopy suggests that it could be Na-hP4, a double-hexagonal close-packed lattice. The dense structure no longer resembles the free-electron model of metals; instead, the positively charged atomic cores are pushed so close together that negatively charged electrons are trapped in interstitial regions.

The demonstration of optically transparent metals shows that pressure places limitations on the typically assumed model of electronic behaviour of metals and provides opportunities to extend our understanding of matter. The researchers say that other metals are likely to show similar transparency under pressure.

DAVID PILE

ORGANIC SOLAR CELLS

Overcoming recombination

The construction of a polymer solar cell that can successfully collect an electron and hole for almost every incident photon suggests that great improvements in the efficiency of organic photovoltaics should be possible.

Michael D. McGehee

When a semiconductor in a solar cell absorbs light, electrons in the valence band are excited into the conduction band[1], and their absence in the valence band creates positive charge carriers known as holes. A goal of solar cell design is to transfer these separated charges out of the cell so that they can become a useful electrical current.

The common solution for collecting the charges is to use a pair of opposing electrodes and an electric field to pull electrons towards one electrode and holes towards the other. One of the greatest obstacles that researchers face when trying to make solar cells efficient is ensuring that the electrons and holes reach the electrodes before undergoing recombination — the process whereby an electron returns to the valence band and can thus no longer contribute to generating a current. When high-quality films of crystalline inorganic semiconductors are used to make a solar cell, it is usually not too difficult to collect all of the charge carriers because they travel quickly and encounter few traps on their way to the electrodes. The internal quantum efficiency, which is the fraction of the excited charge carriers that are collected before they recombine, can often be close to 100%. Unfortunately, growing such high-quality materials is expensive. Consequently, generating electricity

with today's state-of-the-art solar cells is three to five times as expensive as generating it with power plants that run on fossil fuels. There is great interest in reducing this cost by finding ways to print semiconductors in roll-to-roll coating machines similar to those used to make newspapers and photographic film[2]. One of the most promising families of materials for this application is semiconducting (conjugated) polymers.

On page 297 of this issue[3], Alan Heeger, who won the 2000 Nobel Prize in Chemistry for discovering conducting polymers, Kwanghee Lee and their colleagues report that it is possible to make solar cells with semiconducting polymers that have an internal quantum efficiency approaching 100%. The team use a new polymer, poly[N-9′′-hepta-decanyl-2,7-carbazole-alt-5,5-(4′,7′-di-2-thienyl-2′,1′,3′-benzothiadiazole)] (PCDTBT), developed by the research group of Mario Leclerc at the Université Laval. This finding is important because it shows that there is no fundamental problem that prevents nearly perfect collection of charge carriers in polymer solar cells. The breakthrough is a consequence of several factors. A high-refractive-index titania layer was used to prevent interference effects from reducing absorption in the polymer. The polymer layer was only 70 nm thick so that the electric field would be intense and the distance travelled by charge carriers would be small. The polymer absorbs strongly enough to capture most of the light even though the film is thin. For reasons that are probably not fully understood yet, the holes and electrons can be pulled away from each other with a relatively weak electric field.

In the past, researchers have encountered several problems that were thought by some to be potential showstoppers for polymer solar cell technology. In polymer solar cells, the absorption of light generates bound electron–hole pairs known as excitons. A common strategy for splitting the excitons is to mimic photosynthesis and use two molecules with offset energy levels, known as donors and acceptors[2]. When an exciton diffuses to the interface between a donor and an acceptor, the electron transfers from the donor molecule to the acceptor, which has a lower-lying conduction band. With the electron and hole on two separate molecules, the rate of recombination can be greatly slowed. The electron and hole, however, are still strongly attracted to each other because of their opposite charge and tend not to separate from each other unless there is an electric field to pull them apart. There has been concern that it would not be possible to separate nearly all of these electron–hole pairs without applying a negative voltage to the solar cell to provide a strong electric field[4]. To obtain efficient power conversion in a solar cell, however, it is necessary to collect the charge carriers with a very small internal electric field so that a large current and voltage can be generated. The findings presented here by Heeger *et al.* show that for at least one polymer it is possible to collect nearly all of the charge carriers under such conditions.

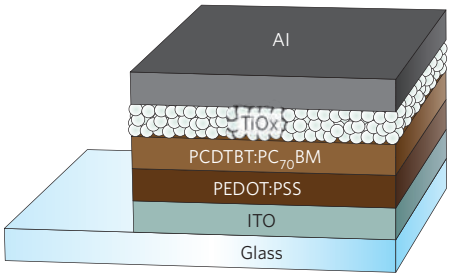

Figure 1 | Schematic of an organic solar cell with almost perfect internal quantum efficiency. It consists of layers of titania (TiOx) and the organic materials PCDTBT:$PC_{70}BM$ and PEDOT:PSS sandwiched between electrodes made from aluminium and indium tin oxide (ITO). The cell is fabricated on a glass substrate.

Another problem that has been identified is the build up of space charge[5]. If the mobility of one charge carrier is substantially greater than that of the other, then the faster charge carriers leave the device more quickly, leaving behind the slower carriers of opposite charge in the semiconductor film. When this happens, the space charge that builds up generates an electric field that opposes the built-in electric field that normally exists in the device. Consequently, the electron–hole pairs at the donor–acceptor interface tend not to separate before recombination occurs. A third, related but different, potential problem is bimolecular recombination, which is the process by which an electron excited into the conduction band by the absorption of one photon recombines with a hole formed by the absorption of another photon. There was concern that because the charge-carrier mobilities are relatively low in semiconducting polymers, the rate at which they leave the device would not be fast enough. If substantial charge-carrier densities built up under the Sun's illumination, electrons and holes would be highly likely to encounter each other and recombine before finding their way to the electrodes. It is well known that semicrystalline polymers have high enough charge-carrier mobility to prevent this problem. It has not been clear, however, that amorphous polymers could have sufficient charge-carrier mobility. The polymer used by Heeger *et al.* seems to have little or no crystallinity, yet its charge-carrier mobility is apparently high enough to prevent either of the kinds of recombination just described. It is encouraging that amorphous polymers can be used because it would be a great challenge for chemists to make molecules with exactly the right energy levels for a solar cell if they also had to make sure that the molecules had a very simple structure that enabled crystals to form.

With nearly 100% internal quantum efficiency for their polymer, Heeger *et al.* were able to obtain a power conversion efficiency of 6.1%. Although remarkable for a solar cell made by spin casting, this efficiency will need to be increased to at least 10% and probably 15% for polymer solar cells to have a noticeable impact on the way society generates its electricity. It should be possible to achieve 11% efficiency by optimizing the energy levels of the polymers[6]. Because the bandgap of PCDTBT is slightly too large, photons in the near-infrared part of the spectrum cannot be absorbed. However, chemists are rapidly developing polymers with smaller bandgaps which should remedy this drawback. Another opportunity for improvement is to reduce the amount of energy lost during electron transfer. In Heeger's solar cell 0.7 eV is lost when the electron is transferred from the polymer to the acceptor. Many in the research community working on polymer solar cells believe that this energy drop can be reduced to 0.4 eV, which is the exciton binding energy in most systems. If they are right, it should be possible to increase the open-circuit voltage (the voltage when the current is zero) of the solar cell from 0.9 V to 1.2 V, which is important because the power generated by a solar cell is proportional to the open-circuit voltage.

Another avenue for improving organic solar cells that should make it possible to attain power conversion efficiencies of 15% or higher is to stack solar cells with different bandgaps on top of each other[7]. With this tandem cell architecture, the higher-energy photons in the solar spectrum are absorbed in a layer with a larger bandgap so that the amount of energy that is lost when the excited carriers relax to the edge of the valence and conduction bands is reduced. This layer can

generate a larger voltage. Another layer with a smaller bandgap is used to harvest the lower-energy photons. The layers are connected in series so that the voltages can be added in much the same way that batteries are connected in series to attain a higher voltage.

This year the vast majority of solar cells being manufactured will be made of crystalline silicon[1]. As the prospects for reducing their cost radically are low, many companies are racing to develop alternatives — mostly inorganic thin-film solar cells based on amorphous silicon, CdTe and $Cu(In_xGa_{1-x})Se_2$. But all of these material systems have some drawbacks. It is hard to make amorphous silicon cells cost-effective because these films typically have to be deposited at an excruciatingly slow rate of a few ångströms per second. Films of CdTe and $Cu(In_xGa_{1-x})Se_2$ can be deposited faster, but simple calculations show that if all of the world's known reserves of tellurium and indium were used to make solar cells, one could only generate about 0.16 TW of power. More of these elements will surely be found, but it remains unclear whether these semiconductors will be one of the chief players in solving the world's energy problem. The limitations of these technologies may leave the door open for polymer solar cells to lead the market in 10 to 15 years and provide the world with several terawatts or more of clean electricity. The advance reported in this issue is an important step towards realizing this dream. ❐

Michael D. McGehee is in the Department of Materials Science and Engineering at Stanford University, 476 Lomita Mall, Stanford, California 94305-4045, USA.
e-mail: mmcgehee@stanford.edu

References

1. Ginley, D. S., Green, M. A. & Collins, R. *MRS Bull.* **33,** 355 (2008).
2. Mayer, A. C., Scully, S. R., Hardin, B. E., Rowell, M. W. & McGehee, M. D. *Mater. Today* **10,** 28–33 (2007).
3. Park, S. H. *et al. Nature Photon.* **3,** 297–303 (2009).
4. Blom, P. W. M., Mihailetchi, V. D., Koster, L. J. A. & Markov, D. E. *Adv. Mater.* **19,** 1551–1566 (2007).
5. Mihailetchi, V. D., Wildeman, J. & Blom, P. W. M. *Phys. Rev. Lett.* **94,** 126602 (2005).
6. Scharber, M. C. *et al. Adv. Mater.* **18,** 789–794 (2006).
7. Dennler, G. *et al. Adv. Mater.* **20**, 579 (2008).

MATERIALS

Ultraviolet-emitting gallium nitride fractals

Although fabrication of complex fractal structures remains immensely challenging in the lab, it is commonplace in nature: snowflakes, lightning and the shell of the nautilus sea creature all show fractal patterns. Now, researchers from the University of Tokyo in Japan have succeeded in fabricating gallium nitride (GaN) fractal nanostructures that emit ultraviolet light at room temperature (*Appl. Phys. Express* **2,** 031004; 2009). The nanostructures made by Shunsuke Yamazaki and his colleagues resemble dendrites — the tree-like extensions found on nerve cells.

The GaN fractals were grown at room temperature on a sapphire substrate by photochemical vapour deposition in a reaction chamber containing trimethylgallium and ammonia gases. The researchers used a fifth harmonic Q-switched Nd:YAG laser (λ = 213 nm) to initiate photodissociation and split the trimethylgallium and ammonia into their constituents, triggering the growth of gallium nitride.

Fractals have a self-similar structure in that they are characterized by the repetition of similar patterns at ever-diminishing scales. They occur naturally all around us, famous examples being snowflakes, dielectric breakdown (lightning), stalagmites and stalactites, sea urchins, starfish, broccoli, ferns and veins on some leaves. Even mountain ranges and shorelines can be loosely fractal.

Yamazaki's dendritic fractals were formed by diffusion: that is, the particles experienced Brownian (random) motion until they touched a solid structure and solidified onto it. Reiteration of the process results in the fabrication of the fractals. Dendritic fractals are known to have a fractal dimension — a 'packing' parameter describing how much space the fractal fills — of about 1.7. And, indeed, scanning electron microscopy images of the GaN nanostructures gave a similar value, indicating their dendritic fractal character.

Photoluminescence spectra from the dendritic GaN fractals revealed peaks confirming the high quality of the GaN crystalline structure and a quantum confinement effect. The latter occurs when materials have features comparable in size to the electronic wavefunction, in this case indicating the ultra-fine fractal structure of the GaN.

Structures with nano-sized features often offer unique optical and electronic properties that are very different from those of bulk materials. This latest research not only provides new avenues for fabrication of nanostructures, but is yet another example of nature's endless inspiration to science.

DAVID PILE

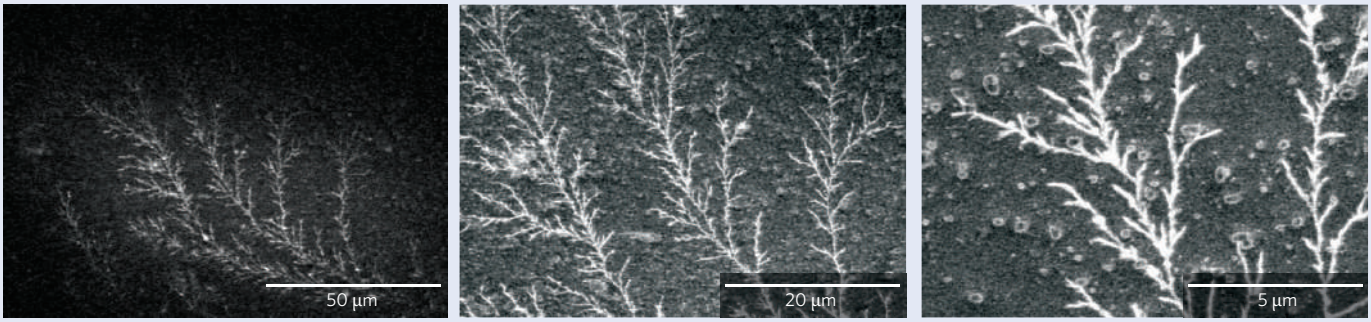

ERRATUM

Signal analyser on an optical chip

Christophe Dorrer

Nature Photonics **3**, 136–137 (2009), corrected after print 26 March 2009.

In the version of this News & Views originally published, Figure 1 was missing. It should have appeared as shown below. This has now been corrected in the HTML and PDF versions.

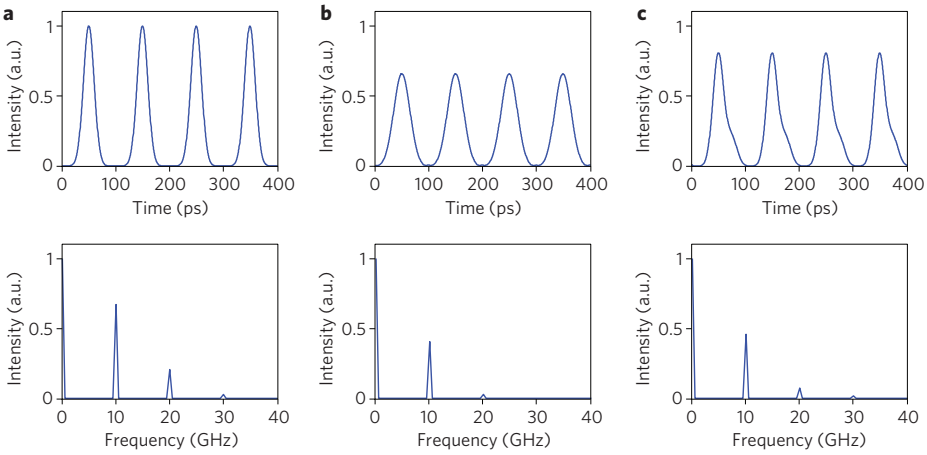

nature photonics

TECHNOLOGY FOCUS

MAY 2009

MATERIALS PROCESSING

nature publishing group npg

Nature Publishing Group
Physical Science subject portals

Focusing on your field

www.nature.com/chemistry

www.nature.com/earthsciences

www.nature.com/materials

www.nature.com/physics

npg nature publishing group

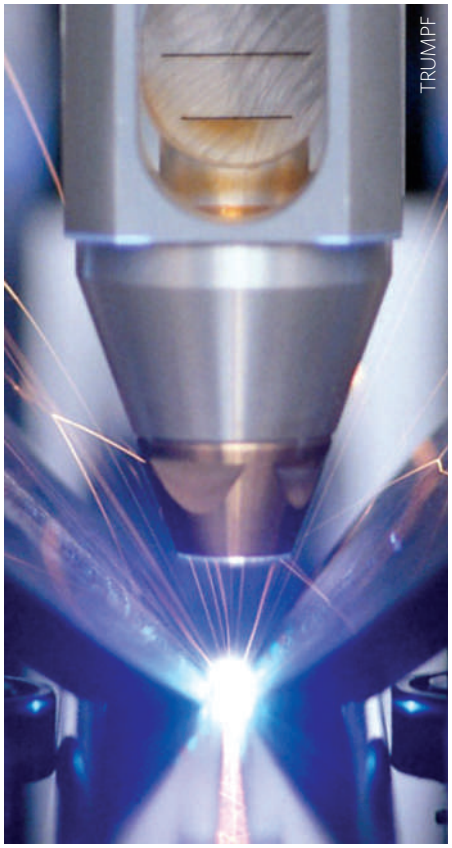

COVER IMAGE
The laser has become a popular and valuable tool for many kinds of materials processing.

NPG ASIA-PACIFIC
Chiyoda Building 2-37
Ichigayatamachi, Shinjuku-Ku, Tokyo
162-0843 Japan
T: +81 3 3267 8751
F: +81 3 3267 8746
naturephoton@nature.com

EDITORS
NADYA ANSCOMBE
OLIVER GRAYDON

CONTRIBUTING EDITOR
RACHEL WON

PRODUCTION EDITOR
CHRIS GILLOCH

ART EDITOR
TOM WILSON

SALES ACCOUNT MANAGER
KEN MIKAMI
T: +81 3 3267 8751
F: +81 3 3267 8746

nature publishing group

Limited visibility

In recessions, the manufacturing industry is always hit hard. So out of all the companies in the photonics industry, companies making laser systems used in manufacturing have been some of the hardest hit by the current financial crisis. What makes this downturn different from others in the past is the speed with which it has hit. Companies are reporting respectable results for the financial year up to the end of 2008, but then disastrous results for the first quarter of 2009 (see page 259).

All industries into which laser-processing equipment is sold have been affected, even the photovoltaics sector, which has, until now, seen double-digit growth for several years. But the news is not all bad. In hard times, the technologies that survive and ultimately flourish are those that have economical advantages over others. With this in mind, many laser-based manufacturing technologies should emerge from this recession stronger than ever. In almost every manufacturing environment, the laser can do things that traditional tools cannot and it can do them faster, cheaper and more efficiently. This is why the laser materials processing industry is faring better than the traditional machine tool industry in the current economic climate.

One example where laser technology is making itself indispensable is in the area of plastics welding. With the advent of diode and fibre lasers, system performance has improved and this non-contact technique gives higher-quality seams than are possible with conventional techniques (see page 270). For rapid prototyping, laser sintering enables complex shapes to be made that were previously not possible; it can not only make models but can also be used to manufacture functional products out of metal (see page 265). And for those metal parts that require strengthening, laser shock peening is now a proven successful process, especially in the aerospace sector (see page 267).

CONTENTS

Hours spent on information tasks a week: **9**

Decisions made based on library-provided information: **65%**

Dollars saved per interaction with the library: **$2,218**

The value of accessing the right information quickly adds up.

Your library plays a key role in putting the right information at your fingertips. Ask your librarian now about starting a site license to Nature Publishing Group journals and ensure you have the world's best science and medicine on your desktop when you need them most. An NPG site license is available for every organization. An NPG site license will save you time and money.

For more information visit **www.nature.com/libraries**

Source: 2007 Outsell, Inc.

nature.com

nature publishing group npg

Gloomy outlook ahead

Although many laser systems manufacturers have announced positive financial results for the end of 2008, they warn of bad news to come. The current economic crisis has hit many firms hard and, as is common in such situations, acquisitions and staff redundancies abound.

Positive results include IPG Photonics' revenues, up by 21% for 2008; Micronic's sales, up by 8% for 2008; and Ultratech fourth-quarter sales, up by 15%. But for some the figures are not so promising. Rofin Sinar has reported a 21% reduction in net sales and a 55% reduction in net income for the first quarter of fiscal 2009 compared with the same period in 2008. The company saw a decrease in sales of its products for macro applications (welding, cutting and surface treatment) of 32% and a decrease in micro (fine processing of small targets) sales of 14% for the first quarter of fiscal 2009. Günther Braun, CEO of Rofin Sinar, says, "With very few exceptions, we experienced diminished demand across all industries, even in the photovoltaic industry, which is something we have never seen before."

Laser materials processing systems are used in a huge variety of industries, each with their own dynamics, so identifying market trends is difficult. However, it seems that both macro and micro materials processing have been affected.

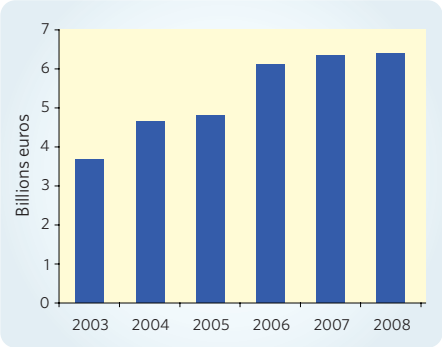

The world market for laser systems (in billions of euros) has flattened in recent years and may well decline in 2009.

"While many companies are reporting growth in 2008 compared with 2007, order logging started to decrease by mid-2008," says Arnold Mayer, whose company, Optech Consulting in Switzerland, specializes in tracking the laser materials processing market. "Production volumes started to decrease in the third and fourth quarter of 2008 and we will only see the full effects of the crisis in the financial results for 2009."

Many companies, mainly in the microprocessing markets, are already making redundancies. For example, laser micro-engineering systems supplier ESI has cut its workforce by 12%; Swedish photomask manufacturing equipment vendor Micronic has cut 96 staff despite growth in 2008; and lithography tool supplier Cymer has announced 100 job cuts just a few months after making 85 people redundant (see news story below).

Mayer points out that the laser microprocessing market so far has weathered the downturn better than the semiconductor equipment market, as it also includes equipment for manufacturing solar cells and flat-panel displays. And although the crisis is also severely affecting macroprocessing markets, Mayer says it could be worse. "The laser macroprocessing market is still developing better than the machine tool market," says Mayer. "This downturn has taken hold vigorously, and companies have felt an effect within two quarters. Nobody knows how long or deep this downturn will be."

Cymer reports job losses

Cymer has announced a net income of US$36.5 million for 2008 compared with a net income of US$88.4 million for 2007. The fourth-quarter performance was particularly poor with net income of US$4 million compared with US$21 million in the same quarter of the previous year.

Bob Atkins, Cymer's chief executive officer, says, "Cymer employees executed well in a very difficult business environment. We extended our argon fluoride (ArF) immersion market leadership and made continued progress towards the development and commercialization of our extreme ultraviolet (EUV) light source technology."

For the full year 2008, the company shipped a total of 100 light sources, for advanced chip-making applications.

Commenting on the outlook, Atkins states, "The current business environment is quite uncertain, characterized by shrinking lithography-tool demand, and decreasing chip-maker factory utilization in the second half of 2008. Looking at the first quarter of 2009, demand for new light sources and installed base products has declined further since our mid-January preliminary revenue estimate."

In the meantime, the company has taken some cost-cutting measures. These include a 10% reduction in personnel or an approximate 100 headcount reduction; temporary 10% reduction in employee base pay; and considerable reduction in non-essential operating and capital expenditures.

Based on the limited information that exists, the company currently anticipates that its first-quarter 2009 revenue could decrease by 30 to 35% compared with revenue for the fourth quarter of 2008.

IPG responds to downturn

IPG Photonics, the fibre laser specialist, has reported that revenues for the full year 2008 increased by 21% to US$229.1 million from US$188.7 million in 2007, and net income increased by 23% to US$36.7 million from US$29.9 million last year. For the fourth quarter of 2008, revenues increased by 6% to US$58.2 million and net income increased by 9% to US$9.1 million compared with the fourth quarter of 2007.

The company saw particular strength in Germany, where it increased fourth-quarter sales by 48% year over year, and Japan, where it saw 25% sales growth. Despite the strength in Japan, overall sales to Asia were down 10% as a result of weakness from marking applications in China. Overall sales in Europe and the Rest of the World were up, with North America relatively flat for the quarter.

Despite the positive revenue figures, IPG certainly has not been immune to current turmoil in the world economy. Over the past six months (October 2008 to March 2009), IPG's stock has halved in value from US$16 to US$8.

To cope with the current global financial crisis, the company has put in place several cost-cutting procedures. "First, we are decreasing our costs of goods by lowering component costs through technological improvements and implementation of in-house production of several critical parts that have been previously outsourced. In addition, we are cutting expenses by freezing new hiring, cutting overtime, curtailing bonuses, lowering headcount through attrition and implementing tighter spending controls," says Valetin Gapontsev, IPG's chief executive officer. "With these initiatives, we estimate that we can generate $4.0 to $6.0 million in annual operating expense savings."

For the first quarter of 2009, IPG Photonics expects revenues in the range of US$45 million to US$50 million.

Preserving non-crystallized metallic glasses

Appl. Surf. Sci. **255,** 6641–6646 (2009)

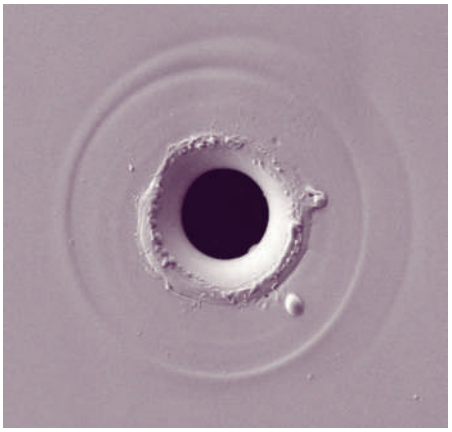

Researchers from Spain and the United Kingdom have demonstrated that it is possible to use both microsecond and picosecond pulsed lasers to machine amorphous nickel alloy samples without crack or defect formation. Amorphous alloys are metallic glasses that have short-range atomic ordering and hence non-crystalline microstructure. These materials have been preferred to crystalline alloys for applications in microelectronics mechanical systems and die components because of their ease of formability and excellent mechanical properties. To maximize their potential, it is essential to maintain their non-crystalline nature during micromachining processes. The study by Iban Quintana and co-workers involves creating single-pulse craters and drill holes on amorphous and polycrystalline nickel alloys using both microsecond and picosecond pulsed lasers with different average laser powers. Craters with a bigger diameter and a more pronounced redeposition of molten material around their edges are obtained in amorphous alloys under microsecond-laser processing. The researchers report no crack formation around the hole drilled in amorphous alloys, showing no evidence of crystallization but high surface integrity, unlike the case in polycrystalline alloys. "This is the first comparative study of the machining response of an amorphous material and its crystalline counterpart. We show that the non-crystalline microstructure of amorphous alloys can be preserved under microsecond and picosecond laser processing and that amorphous alloys give significantly better results than polycrystalline alloys under equivalent processing conditions," Quitana told *Nature Photonics*.

Laser annealing for silicon photonics

Appl. Phys. Lett. **94,** 082104 (2009)

Conventional SiGe growth techniques require high temperatures and are often expensive and time-consuming. In view of the growing demand for Ge-on-Si devices in the optoelectronics sector, alternative low-temperature fabrication approaches are desirable. A group of researchers from Singapore has now developed a low-cost, ultrafast scheme for forming epitaxial SiGe structures on a silicon substrate. In a technique based on laser annealing with a 248-nm pulsed KrF excimer laser, C. Y. Ong and colleagues demonstrate crystallization of an amorphous germanium layer deposited directly on a Si^+ pre-amorphized implanted Si (PAI-Si) substrate. The team observe that when the sample is annealed with an appropriate energy density, polycrystalline SiGe is formed by explosive recrystallization. For an energy density of 0.9 J cm^{-2}, the entire amorphous layer melts into the crystalline Si substrate, leading to a liquid-phase epitaxial regrowth of SiGe and therefore a fully strained and activated epitaxial SiGe.

Multispot writing in fused glass

Opt. Express **17,** 3531–3542 (2009)

Owing to its highly deterministic and nonlinear absorption process, infrared femtosecond laser writing offers the means to create buried, localized structural modifications in transparent materials. By moving the sample with respect to the laser's focal point, three-dimensional structures can be inscribed. However, the fabrication of complex structures often involves long processing times. Cyril Mauclair and co-workers from France and Germany have now demonstrated that the problem of speed can be solved by parallel photoinscription that uses multiple laser spots with reconfigurable patterns. The trick is to use a periodical binary phase mask to spatially modulate the wavefront of the laser beam. By varying the period (cycling frequency) of the binary phase, the team show that a simple grating phase mask and therefore dynamic double-spot operation can be achieved. The team use a liquid-crystal spatial light modulator, addressed optically, to create the binary phase mask. A 800-nm Ti:sapphire laser emitting 150-fs pulses at a

Rapid-micropatterning hydrogel

Adv. Eng. Mater. **11,** B20–B24 (2009)

Generally, fabrication of two-dimensional periodic arrays of micropatterns on hydrogels involves sequential procedures and is thus lengthy. A direct patterning approach based on multibeam laser interference taken by researchers from the United States and Germany looks set to speed up and also improve the throughput of the process. "Periodic structures can be processed in one step in a few milliseconds over large areas using high-power lasers on a wide range of materials including ceramics, metals and polymers", Andrés Lasagni told *Nature Photonics*. The approach by Lasagni and co-workers relies on multibeam interference and the use of a 10-ns pulsed Nd:YAG laser at 355 nm and a 95-fs pulsed Ti:sapphire laser at 800 nm with a repetition rate of 1 kHz. The hydrogel they study is polyethylene glycol diacrylate (PEG-DA), a biocompatible hydrogel that is useful for a number of biomedical applications. The team find that the use of femtosecond laser pulses allows the creation of structures with a higher aspect ratio and resolution than for longer-duration pulses. They attribute this to polymerization induced by two-photon absorption and to the increased energy difference between the interference minima and maxima with increasing beams. In the case of nanosecond pulsed patterning, interconnections between periodic structures are found, possibly owing to the low polymerization threshold of the material at short laser wavelength.

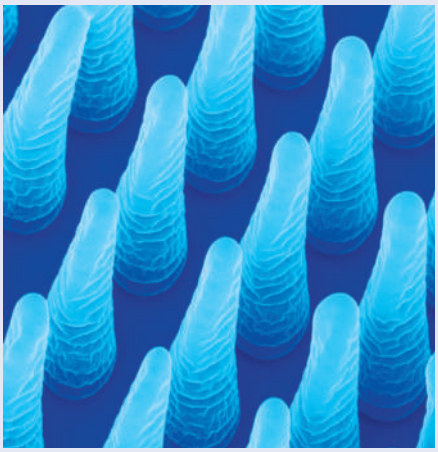

This rapid fabrication technique is expected to diversify the biomedical applications of hydrogels.

repetition rate of 10 kHz and with a power of 30 mW is used for the process. By controlling the motion of the sample, the team succeeded in manufacturing three-dimensional light dividers and fabricating wavelength-division demultiplexing devices in fused silica. They are confident that with sufficient energy, more machining foci can be used.

Optical tweezers boost direct-write nanolithography

Opt. Express **17,** 3640–3650 (2009)

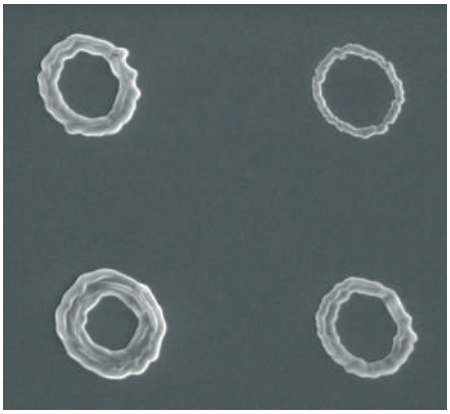

By integrating a Bessel beam optical trapping scheme into a laser nanolithography process, researchers from Princeton University in the United States have shown that arrays of identical arbitrary patterns of nanostructures can be generated with high uniformity and high positional accuracy. Despite advances in nanofabrication technology, generating arbitrary nanopatterns with high throughput has proved challenging. Now, Euan McLeod and Craig Arnold demonstrate parallel fabrication of arrays of patterns by using two lasers for patterning: one Bessel beam converted from a 7-W continuous-wave laser beam at 1,064 nm to optically trap a microsphere lens (probe) near a surface, and one 355-nm pulsed laser with pulse energies of 150 nJ to 8 mJ to illuminate the trapped bead and surrounding surface. Arrays of simultaneous traps are created using beam splitters, which separate the trapping laser beam into four parallel beams. Through the parallel writing scheme, the team say that they are able to eliminate errors due to mechanical vibrations and imperfect positioning equipment. Moreover, patterns with varying feature sizes can also be generated by using spheres of different sizes in the array. Fabrication of 100-nm structures can be achieved when the microsphere probe is self-positioned near a surface by the Bessel beam optical trapping. The team report that they have obtained a feature size uniformity and relative positioning accuracy of better than 15 nm. They are also confident that the use of more powerful and narrower Bessel beam optical traps will further improve the uniformity and accuracy of the proposed technique.

Thermochemically welding silver alloys

Opt. Laser Eng.
doi:10.1016/j.optlaseng.2009.02.003 (2009)

A study presented by a team of Italian researchers shows that high-power diode lasers could serve as an alternative technology for welding silver alloys, replacing conventional techniques. Silver alloys are known to have high reflectance in the visible and near-infrared wavelengths, making it difficult to weld them using a diode laser. However, it is also known that thermochemical interactions in these alloys can boost the absorption and maximize the transfer efficiency between the laser source and substrate. Using a diode laser with a wavelength of 940 nm and maximum power of 1.5 kW, Annamaria Gisario and co-workers investigated the interactions between the laser and two different silver–copper alloys. They confirm that thermochemical effects induced by diode lasers could lead to a chain of sustainable exothermic reactions — formation of an oxide layer, which results in an increase in absorption and substrate temperature and thus further formation of an oxide layer. The researchers say that a good welding strategy for reducing defects is a pre-heating step at constant power, decreasing power along the laser pattern and appropriate laser scanning speeds.

Burst-mode benefits

Appl. Phys. Exp. **2,** 042501 (2009)

Groups of femtosecond laser pulses provide more control over the pulsed laser deposition process in nanomaterials and thin films, according to researchers from IMRA America in the United States. The approach by Makoto Murakami and colleagues uses a burst of femtosecond laser pulses. Groups of 700-fs laser pulses each with a pulse energy of up to 10 μJ and a total average power of up to 2 W are produced by a chirped pulse amplification system based on optical fibre technology equipped with an acousto-optic modulator. A burst of pulses is released at a repetition rate of 0.1–5 MHz with a separation of 20 ns between neighbouring pulses within each burst. Three different bursts of pulses — 1 pulse per burst, 5 pulses per burst and 10 pulses per burst, at repetition rates of 1 MHz, 200 kHz and 100 kHz, respectively — are used to produce the same pulse energy of 0.4 μJ and average power of 0.4 W. The team demonstrate that the use of a custom-designed optical pulse train enables them to tune the size of nanoparticles in the deposited film in a continuous manner and produce high-quality thin films. Interestingly, the researchers report a reduction in particle size with increasing number of pulses in each burst, even when the same total average power and individual pulse energy are used.

Sloping design perfects dissimilar joint

Opt. Laser Eng.
doi: 10.1016/j.optlaseng.2009.02.004 (2009)

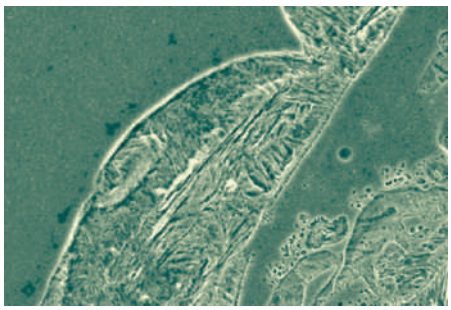

Copper–steel conductors are attractive for power-generation industries because of the combined high mechanical resistance of steel, and the conductivity and resistance to corrosion of copper. But joining these two materials using conventional and laser welding techniques has not been easy owing to the mismatch in material properties. This problem can now be overcome, according to a group of researchers from China. In the butt-welding scheme by Chengwu Yao and co-workers, the Cu–Fe dissimilar joint is designed in a scarf joint geometry and a CO_2 laser with a maximum output power of 15 kW illuminates the steel side. The researchers show that through the use of the laser they can control the dilution ratio between copper and steel, and hence obtain different microstructural features in the interface between the two metals. In particular, they report that a transition zone with a large proportion of granular phases is formed near the intermixing zone when the welded joint has a high percentage of copper. Defect-free joints with high tensile strength can be achieved when the copper is dissolved in small amounts in the molten steel. The team envisage that their findings will help to optimize the laser welding of joints of dissimilar metals.

Beating the downturn

Laser systems manufacturer Trumpf believes it can survive in the current economic climate with its strategy of diversification in both the laser technologies it is able to offer clients and the wide range of end-user applications that it serves. **Nadya Anscombe** finds out more.

In tough times it sometimes helps to be different. Trumpf, the German materials processing specialist, is different from many large engineering companies in that it is still privately owned. It is this fact, together with the company's strategy of having products covering a diverse range of applications, that is keeping the company thriving while many have fallen by the wayside.

The past financial year (2007/08) saw Trumpf's laser division grow by 16%, with the entire Trumpf group reporting sales of 2.14 billion euros and adding 700 new jobs in Germany and abroad. Jens Bleher, managing director of Trumpf Laser and Systems Technology, believes that the success in his division is because the firm has such a broad spectrum of laser sources — from CO_2 lasers, disk lasers and rod lasers up to and including fibre lasers. "This is how we differentiate ourselves from the many competitors in the market, some of whom offer only one or two platforms and then, of course, praise these as the latest and the greatest," he says.

He also believes that being a family-run business helps in this economic climate. "The family takes a long-term view of the company and makes decisions that will sustain the company," he says. "We are not dependent on the stock exchange and the money the company makes does not leave the company but instead gets reinvested."

Jens Bleher, managing director of Trumpf Laser and Systems Technology.

The company now has more than 8,000 employees worldwide. Most of Trumpf's growth over the years has been organic, with one or two strategic acquisitions along the way. With its recent purchase of UK fibre laser company SPI Lasers, Trumpf has now become a one-stop shop for anyone looking for laser systems for materials processing. Whether you need a laser for cutting, welding, marking, surface treatment or microprocessing, Trumpf has a solution for each application.

Whether this strategy will deliver similar growth this financial year (2008/09) remains to be seen, but Trumpf believes it is this diverse range of products that means the company can survive in the current economic climate. The automotive industry, one of Trumpf's largest clients, has been hit very hard in the past year. Bleher admits that this has also affected sales of laser systems into this industry. "But it has not affected us as strongly as some might think," he says. "Our lasers go into new product lines and our customers are still launching new products." He admits that Trumpf is having to adapt its own manufacturing capacity, with reduced working times for some of its staff. But he points out that this only brings the staff down to normal working times, as they have been working extended hours to cope with demand until now. In fact he believes that the economic downturn could even benefit laser technology in the long term. "Displacement of conventional technology in manufacturing is being led by the laser," says Bleher. "In general manufacturing there is still room for growth for laser technology. Many companies are beginning to recognize the economic advantage of investing in this technology."

Disk lasers

A disk laser is a diode-pumped solid-state laser where the gain medium (laser crystal) has the geometry of a thin disk rather than a rod or slab as is the case in conventional solid-state lasers. The benefit of the disk geometry is that the disk has a large surface area which allows improved cooling of the gain medium. This helps combat detrimental thermally induced optical effects, such as thermal lensing, which degrade laser performance at high powers. The concept of the disk laser was first demonstrated by Adolf Giesen and colleagues at the University of Stuttgart, Germany, in the early 1990s. It has since been commercialized by companies including Trumpf and proved to be a popular design for kilowatt-class lasers.

Trumpf has now increased the power of its disk laser up to 16 kW. Offering a beam parameter product of 2–8 mm mrad, the new-generation TruDisk lasers maintain beam quality regardless of increases in power, resulting in a scalable design. The company claims that the TruDisk's integrated power sensors and real-time power feedback control guarantees continuous, steady and reliable power at the workpiece.

A unique modular design allows individual diodes and laser components to be serviced onsite, an impossible feat for comparable technologies. Greater access to fibre optic cables allows the system to be serviced while the laser is in operation. This permits parallel fibres to maintain production without interruption. The design also makes it possible to upgrade laser power with additional diodes. This increases production capabilities as needed without requiring an additional laser unit. The company claims that the diode life expectancy is over 50,000 hours and that the system has a wall-plug efficiency of up to 30%.

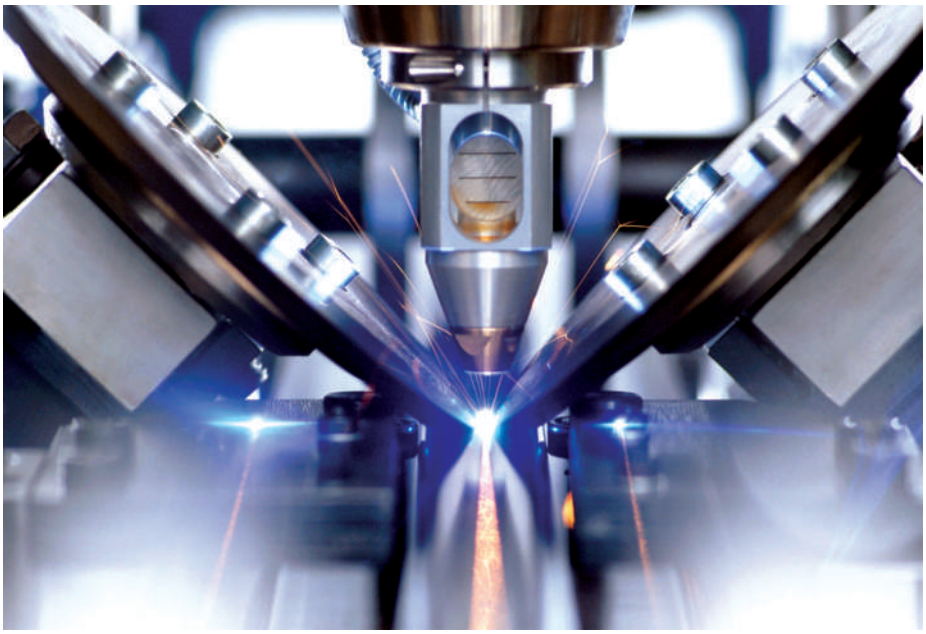

TRUMPF

An example of welding with a Trumpf laser.

For example, Trumpf has seen particularly high growth in sales of lasers to the photovoltaics industry and also some areas of the electronics industry. These are markets particularly suited to the disk and fibre laser.

Trumpf pioneered the commercialization of the disk laser (see Box), but until its purchase of SPI Lasers last year, the company had only a limited offering in the fibre laser field. This was seen by some as a rejection of fibre laser technology, and Trumpf's purchase of SPI Lasers took some people by surprise. But for Trumpf, the acquisition makes perfect sense. "We continue to believe that higher powers are and will remain clearly the domain of the disk laser," says Bleher. "It is the right design for industrial applications in the high multi-kilowatt continuous-wave power range. The disk is a robust and easily scalable platform that cost-effectively allows good to very good quality beam generation. It has great potential for the future."

TRUMPF

A solid-state laser cutting a series of fine patterns in a medical instrument.

In contrast to the fibre laser, the power density inside the resonator of a disk laser remains far below the critical destruction threshold of the laser medium, even at high powers. The disk laser user need not fear a beam source failure in the event of reflection from the component because it was especially designed to be insensitive to reflection. For this reason, Trumpf believes that, for higher powers, the disk laser allows better system use and considerably higher productivity.

The company is marketing its fibre lasers in a lower power range than its disk lasers and therefore feels that the two ranges fit very well together. For fibre lasers, applications include welding and cutting when very precise contours are needed in thin sheet metal. "We will continue to offer our TruFibre 300 product and will integrate SPI Lasers' products into our line and extend it," says Bleher. "SPI has been a supplier of ours for several years and we will continue this relationship. SPI even supplied some of our competitors and we intend to keep these two business models. Two brands, two companies."

Bleher is not keen to enter into a discussion about which laser — disk or fibre — is best. As he points out, many of Trumpf's customers just want a system that is appropriate for their application and the laser technology itself is not the primary concern of the customer. "Every technology has its advantages that we need to exploit based on the customer's needs," says Bleher. "That is why Trumpf uses every available technology and continues to develop them."

As well as fibre and disk lasers, Trumpf also sells CO_2 lasers and most recently has added direct diode lasers to its portfolio. For two-dimensional laser cutting, the CO_2 laser remains the gold standard for Trumpf. "At present, we don't understand why people feel that the 1-μm wavelength of the solid-state laser is preferable. The cutting behaviour of the CO_2 laser with a 10-μm wavelength offers a high degree of flexibility when cutting sheet metal of different thicknesses," says Bleher. In addition, the high edge quality is an argument for the CO_2 laser as a universal cutting machine.

But he also sees that the key technology of the near future is undoubtedly the diode. "Diode-pumped solid-state lasers and direct diode lasers will play an increasingly important role, in our opinion. The diode will become the central element for all lasers," says Bleher. "In fact it already is."

At the beginning of this year, Trumpf announced record output performance from its TruDiode diode direct laser series: 100 W output from a single fibre optic and a divergence of less than 120 mrad. Because of their high beam quality, even in the multi-kilowatt range, lasers in the TruDiode series are intended for welding applications where lamp-pumped solid-state lasers are currently used. With a wall plug efficiency of 40%, diode lasers work far more efficiently than lamp-pumped solid-state lasers. Another advantage is the small size of the diode module, at only 8 × 6 × 3 cm, which contributes to the very compact and space-saving design of the TruDiode series.

With continued innovation such as this, Trumpf aims to offer its clients a broad and comprehensive range of products to suit their application. "We are currently not of the opinion that a 'disruptive technology' will appear in the near future," says Bleher. "By that I mean a new laser technology that will replace all other beam sources. A broad range of different laser technologies will continue to be used in the future. For this reason, a laser manufacturer needs to be proficient in all types of lasers and be able to offer his customers the relevant technologies. Trumpf will continue to develop all varieties of laser technology in order to offer its customers the best laser for every application in material processing— regardless of the beam source." ❐

Darwin 200 nature insight

Published in 12th February issue of *Nature*, with selected content available free online.

Nature celebrates the birthday of Charles Darwin with a Darwin 200 special, published alongside a *Nature Insight* on Evolution, which focuses on Darwin's theory of descent with modification by means of natural selection. All Darwin-related content, including a *Nature Video* interview with Sir David Attenborough and a special *Nature Podcast* can be accessed within our Darwin 200 special.

Bookmark the Darwin 200 special www.nature.com/darwin, for a growing collection of news, research and analysis on Darwin's life, his science and his legacy.

nature

nature publishing group npg

LASER SINTERING

Layer by layer

Christof M. Stotko

With its intense power and flexibility, the laser has revolutionized sintering technology and made possible the rapid manufacture of prototypes and components from electronic data.

Manufacturers have traditionally used machine tools to produce prototype components by removing material from solid blocks of metal (or plastic), or from castings, forgings or extrusions. When machining a solid, it is not unusual to take away over 90% of the original material, which is both inefficient and expensive in terms of the material used and the swarf that has to be removed and recycled.

In contrast, building a prototype by 'growing' it layer-by-layer has enormous advantages in terms of lowering manufacturing costs and lead times. Such additive layer manufacturing (ALM) has now come of age thanks to laser-sintering technology.

By using a laser to solidify fine metal or plastic powders, fully functional parts can be produced directly without the expense of producing mould tools. There are even laser-sintering machines for direct manufacture of sand cores and moulds for metal casting.

Although other rapid prototyping techniques such as stereolithography, laminar paper modelling, fused deposition modelling and three-dimensional printing are useful for visualizing what a component will look like, the resulting models are too soft or brittle to be used for the intended application.

The ever-increasing complexity of components used in industry is one of the key drivers for the development of advanced laser-sintering technology. Many parts have difficult-to-machine surfaces and internal walls that are easy to produce using ALM. It is even possible to design parts with internal features that can only be made by additive techniques, as subtractive machining would not be able to access some areas.

In the early days, laser sintering, in common with other ALM processes, was regarded as just a rapid prototyping tool, but today it is becoming widely adopted for fully fledged rapid manufacturing. This is termed 'e-manufacturing' — the fast, flexible and cost-effective production of products, patterns or tools directly from electronic computer-aided design (CAD) data.

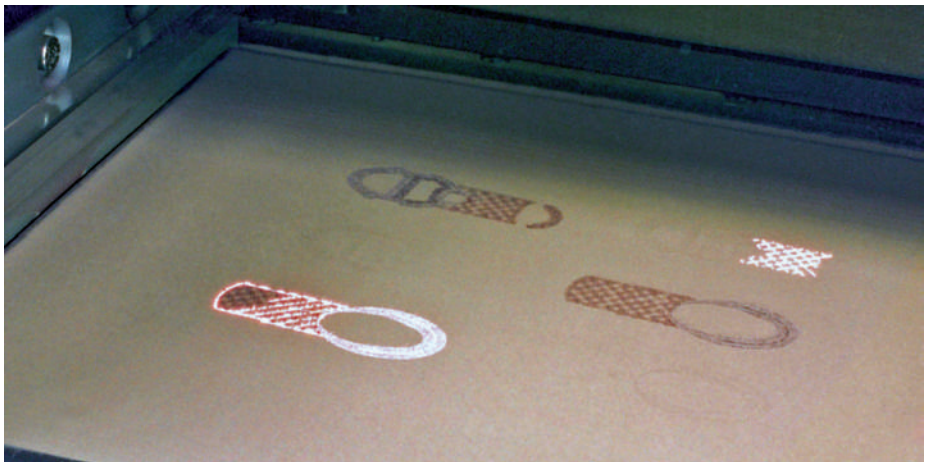

EOS

Figure 1 | Laser sintering in action. A laser beam melts a layer of metal powder which then solidifies. By repeating the process a three-dimensional part can be made.

The technology is making inroads in many areas of manufacture. For example, a plastic injection mould tool is traditionally milled, and conformal cooling channels are then drilled in straight lines near to the surface. Now, the mould can be laser-sintered in a single operation, including the conformal cooling channels, which can accurately follow the contour of even the most complex mould surface. This reduces injection-moulding cycle times and improves the quality of the plastic components that are produced. Another area of saving is product assembly, which can often be eliminated by using ALM to make complex components in a single operation.

To start the laser-sintering process, a very fine layer of powder is spread over a build platform in the process chamber. The layer is typically 20 μm thick for metal and 100 to 150 μm thick for plastics, depending on the required resolution and surface finish. The powder is solidified by a laser (Fig. 1) that is driven using data derived from the CAD model of the component, which has previously been sliced horizontally into layers of the same thickness.

The platform is lowered by the same amount as the layer thickness, a fresh coating of powder is swept over the previously laser-sintered layer, and this in turn is laser sintered. The process continues until the component is complete.

It is noteworthy that this is not conventional sintering using pressure and heat below a material's melting point to bond and partly fuse the powdered particles. In laser-sintering machines, a laser directed by a lens-based optics system melts the metal particles at the laser beam focal spot.

The mechanical properties of finished metal components are as good as, if not superior to, their cast and wrought equivalents. This is largely due to the very small pool of molten material produced, which allows cooling to take place in microseconds after the laser has moved away. Metal parts produced on laser-sintering machines have a homogeneous grain across the entire part. They can be welded, machined, shot-peened, polished and coated afterwards, if required.

An important characteristic of the laser source is the wavelength, which should be well matched to the absorption characteristics of the powder material. The current standards are CO_2 lasers with a wavelength of roughly

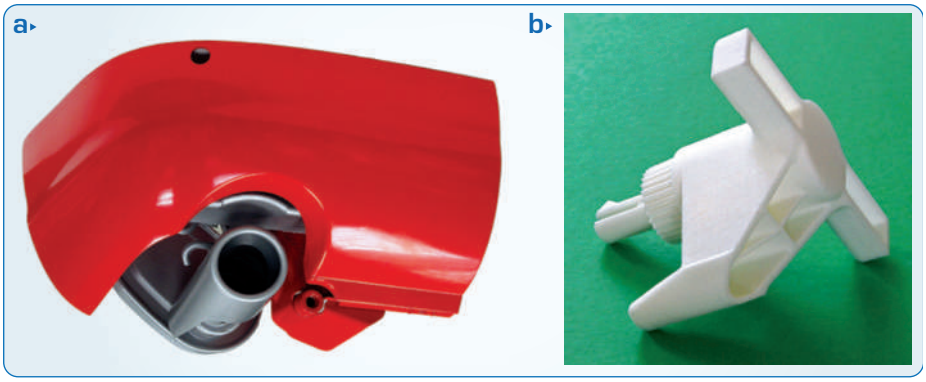

EOS

Figure 2 | Laser sintering and cars. **a**, Close-up of the laser-sintered prototype bumper section for the Jaguar XJ. The painted model was used to visualize the fit and finish of key components before production. **b**, The laser-sintered plastic tool that assists operators working on the new Jaguar XK production line to position window lift mechanisms during assembly.

10.6 μm for processing plastic materials, and ytterbium fibre lasers with a wavelength of about 1.1 μm for processing metals.

Normally, continuous-mode operation is used. Additional important criteria are a laser with excellent beam quality and focusing ability, and good stability in terms of beam power and position.

The diameter of the focused beam in a state-of-the-art laser-sintering machine for metals is less than 0.1 mm. The laser must be sufficiently powerful to guarantee good laser sintering. For processing plastics a range of machines is available, from small, entry-level machines with a small build volume and a 30-W laser, up to systems that use two 50-W lasers working in parallel.

The development of laser-sintering systems so far gives an indication of what can be expected in the future. Component quality and productivity have been considerably upgraded, partly through increasing laser power and improvements in the optical system such as the laser control. The range of machine sizes and types has widened and will continue to do so.

Furthermore, the range of powder materials continues to increase, while new machine options and peripheral devices continue to improve productivity and user-friendliness. In general, laser-sintering technology will keep maturing in terms of quality, productivity, reliability and economics, making it more and more accepted for an increasing variety of applications. Two highly important application areas are the automotive, and medical sectors which will now be briefly described in turn.

DEPUY SPINE

Figure 3 | Prototype plate bender, used to contour plates for spinal surgery, built by DePuy using a laser-sintering system.

AUTOMOTIVE SECTOR

Jaguar Cars is making increasing use of laser-sintering technology at its Whitley Engineering Centre near Coventry, UK, to speed the development of new vehicles by making plastic parts directly from CAD models, eliminating the expense of producing mould tools. It is using the technology for the production of prototype trim and even engine parts from nylon powder (polyamide PA 2200).

The resulting components, such as the air-intake manifold, door inners, fascia substrate, interior air vents and exterior light housings, are robust enough to be used on test vehicles running around a test track, allowing more data to be collected early in the development process. Other rapid prototyping techniques that use materials such as epoxy resin and the thermoplastic ABS produce relatively fragile parts that are best suited for visualization only.

Take the V8 air-intake manifold prototype for a recently introduced Jaguar car. In the past, hundreds of thousands of pounds would have been invested in hard tooling for its manufacture. Following every design change, it would have cost thousands of pounds to alter the tool, a process that took several weeks each time. For substantial changes, a completely new tool might be needed.

Using laser-sintering technology, two design iterations of the manifold were produced and 17 were subsequently built in nylon for less than £1,000 each and in a lead time of one and a half days per manifold. This represented an enormous financial saving in the development of this vehicle component alone and has halved the time needed to perfect it, from one year to six months.

An example of a laser-sintered component for the XJ saloon is a bumper section built in two pieces (Fig. 2a) that was used for visualizing the assembly of key parts such as the exhaust pipe and tow eye fixing. The aesthetics of this part of the vehicle could therefore be evaluated before progressing to hard tooling.

The nesting flexibility afforded by the plastic laser-sintering machines makes it easy to incorporate dozens of parts in each sintering cycle. An interesting component that is regularly added around other parts is not a prototype at all, but a complex plastic assembly aid that assists operators working on the Jaguar XK coupé and convertible to position the window lift mechanisms during build (Fig. 2b).

The manufacturing plant required a stock of 3,000 of these parts, as once fitted, the assembly aid remains on the vehicle throughout the build process.

MEDICAL SECTOR

In the medical sector, one of the world's largest producers of implants and instruments for spinal surgery, DePuy Spine of Raynham, Massachusetts, is using a metal-sintering system to reduce lead times for making new and customized equipment for minimally invasive surgery.

The traditional process of prototyping, design revisions, materials selection, cadaver testing and manufacturing normally results in a lead time of many months. This has been greatly reduced using a metal laser-sintering system. In the first year, DePuy processed 2,000 prototype parts in the machine, including benders (Fig. 3), extractors, surgical screws, clamps and reduction devices. Delivery times for surgical tool prototypes have shrunk from several months to less than a week in some cases.

Surgeons can be very demanding about their requirements for tools such as blades, racks, tweezers and calipers. When they review the parts, they may ask for different handle angles or different spring strengths. It is very easy to adjust the CAD design and make another iteration. DePuy claims that laser sintering lets it make virtually anything surgeons ask for. ❐

Christof M. Stotko is at EOS GmbH Electro Optical Systems, Robert-Stirling-Ring 1, 82152 Krailling, Germany.
e-mail: info@eos.info

SURFACE TREATMENT

Shock tactics

Richard D. Tenaglia and David F. Lahrman

Laser shock peening is a surface treatment process for increasing the strength and reliability of metal components. Traditionally applied to aircraft parts, the technology also shows great potential for automotive and medical applications.

Laser shock peening, or more simply laser peening, is an effective method of increasing the resistance of gas turbine engine compressor and fan blades in aircraft to foreign object damage and improving high-cycle fatigue life. The successes achieved in preventing fatigue failures in turbine blades are driving efforts to expand the application of laser peening to other aircraft structures, helicopters, land vehicles and military equipment, and general industrial uses.

Laser peening forces a high-amplitude shock wave into a material surface using a high-energy pulsed laser. The effect on the material comes from the mechanical 'cold working' effect produced by the shock wave, not a thermal effect from heating of the surface by the laser beam. In fact, the laser beam only makes contact with a temporary protective coating placed on the surface of the part, and no significant heating occurs because of the very short duration of the laser pulse (see Box 1).

The common laser system used for peening is a high-energy, pulsed neodymium-glass laser system with a wavelength of 1.054 μm. Suitable laser peening systems produce short laser pulses, from about 8 to 30 ns in duration, with a beam energy in the range of 10 to 50 J. Although laser systems with lower energy and small spot size or with ultra-short pulse durations have been considered, these systems typically do not provide enough power to create the desired effect. Either circular or square-shaped laser spots may be used, depending on the configuration of the laser system and optical components. The laser spot size may be adjusted with lenses, but it is typically an area in the range of 0.03 to 0.28 cm^2 that is applied to the part. The laser-peening parameters are typically selected to achieve a power density or laser irradiance of 5 to 10 GW cm^{-2}. A two-beam laser system may be used advantageously to laser peen the opposite sides of thin parts, such as the edges of turbine engine airfoils. Laser peening one side of a thin blade completely and then the opposite side can result in excessive distortion, but this can be avoided by using an alternating scheme in which a laser spot is applied first to one side of the blade and then a second beam is applied to the opposite side. Figure 1 shows a two-beam laser system that operates at 50 J per beam.

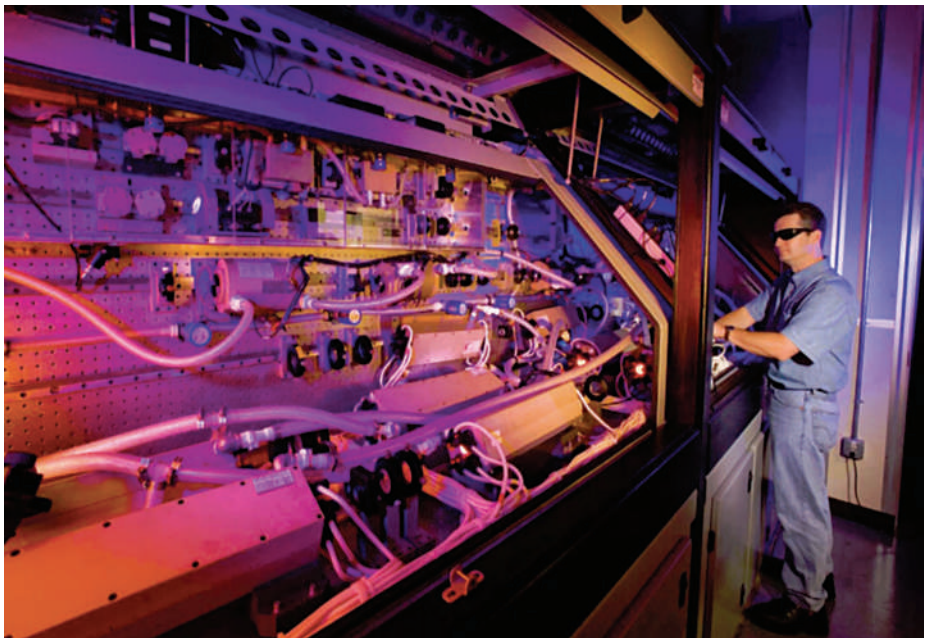

LSP TECHNOLOGIES

Figure 1 | A two-beam, pulsed neodymium-glass laser system (LSP Technologies) that operates at up to 50 J per beam.

In the early 1990s, laser systems were not commercially available with the power or laser repetition rate to make laser peening practical. Typically, laser fluence in the range of 100–200 J cm^{-2} is required to create the desired effect in most materials. Early laboratory-based systems had a repetition rate of only one pulse every 8 minutes. As a consequence, the coverage rate for laser-peening parts was far too slow. The first generation of laser-peening systems was designed with a series of laser amplification stages (all using flash lamps) and an advanced electronic control system. This boosted the laser beam from an oscillator to produce two beams having beam energy up to 50 J per beam and a laser repetition rate of one pulse every 8 seconds (0.125 Hz).

To create the first practical industrial laser-peening systems, the life and reliability of the laser system components had to increase. The electronics for the pulse-forming networks were redesigned to produce a laser repetition rate of one pulse every 4 seconds (0.25 Hz) and assembled into modules for easy replacement in case of failure. The materials used for the flash lamp reflectors and the procedures used to produce the laser rods were optimized to boost efficiency and to extend component life. With support from the US Air Force

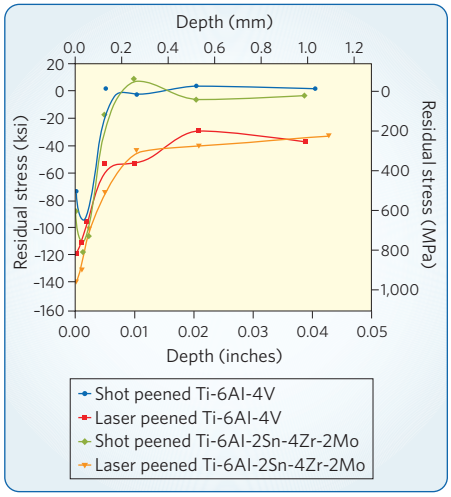

LSP TECHNOLOGIES

Figure 2 | Comparison of residual stress profiles for laser peening and conventional metal shot peening (ksi, kilopounds per square inch).

ManTech programme, LSP Technologies refined laser peening technology by building a system with industrially hardened environmental controls and many quick-change features for parts requiring repair or routine maintenance, and boosting the laser repetition rate to one pulse every 0.8 seconds (1.25 Hz). Each increase in repetition rate required further improvements to the optical system components to avoid damage during operation. Even higher laser repetition rates for laser-peening systems are possible (3 to 5 Hz), although at lower energy levels and using smaller spots. However, laser repetition rate is not the complete answer to boosting the coverage rate. One must also consider the requirements for applying and replenishing the opaque overlay coating and handling the parts. Depending on these requirements and the laser system used, practical laser-peening coverage rates are typically 10–20 $cm^2\ min^{-1}$.

The latest laser-peening systems incorporate improved diagnostics to monitor and control the beam's spatial profile (to assess the energy distribution within the laser spot) and temporal profile (to measure the uniformity of the laser pulse timing). These systems also include electronic features for optimizing the shape of the laser pulse to create a uniform shock wave at the surface of the part. This provides a more uniform compressive residual stress distribution in the part being treated.

Laser peening produces a number of beneficial effects in metals and alloys. Foremost among these is an increased resistance to surface-related failures, such as fatigue, fretting fatigue and stress corrosion cracking. Many metals and alloys have been laser peened successfully, including titanium alloys, steels, aluminium alloys, nickel-base superalloys and cast irons.

The material property changes are derived from the deep compressive residual surface stresses imparted by laser peening. Figure 2 shows an example of the stresses achieved in two titanium alloys and compares these with the shallower compressive stress profiles produced by metal shot peening (the conventional technology, which involves firing small metal spheres against the surface of a part). The compressive residual stresses produced by laser peening extend more than 1.0 mm deep into the surface, whereas the compressive stresses for metal shot-peened samples are present to a depth of only about 0.2 mm.

Box 1 The laser-peening process

To prepare a part for laser peening, an overlay opaque to the laser beam is applied to the material surface to be treated. Opaque overlays can be of a variety of forms; paint (dry or wet), black tape and metal foils (sometimes with adhesive backing) have all been used with varying but similar results in terms of the pressure pulses generated. The opaque overlay protects the surface from direct thermal contact with the laser-induced plasma and provides a consistent surface condition for interaction with the laser beam, independent of the actual material being treated. Direct contact of a metal surface with the plasma will, in most cases, form a thin melt layer on the surface of the metal, ranging from a surface discoloration to a surface melt layer 15 to 25 μm thick, depending on the laser irradiation conditions and metal properties.

A material that is transparent to the laser beam is then placed over the opaque overlay. The simplest and most cost-effective transparent overlay is water flowing over the surface from an appropriately placed nozzle. The water is not used to cool the part but serves the key function of confining the plasma generated when the laser beam interacts with the opaque overlay surface. The confinement increases the pressure developed by the plasma on the surface. This pressure can be up to 10 times the surface pressure developed if the plasma is unconfined and allowed to accelerate away freely from the material surface.

With the two overlays in place, the laser pulse is directed through water and interacts with the opaque overlay, as shown in Fig. B1. The laser energy is absorbed in the first few micrometres of the opaque overlay surface, vaporizing the material and forming a plasma. The plasma temperature rises rapidly through further heating from the incoming laser beam, but thermal expansion of the plasma is limited by the transparent overlay material. The pressure in the confined plasma increases rapidly (up to 6,900 MPa), causing a shock wave to travel into the material through the opaque overlay, and outward through the water overlay. Before the water can be ejected from the surface, the high-pressure shock wave is essentially 'tamped' or concentrated into the material surface. One may think of laser peening as a technique for micro-forging the surface of a material, spot-by-spot, in a highly controlled manner with laser light energy.

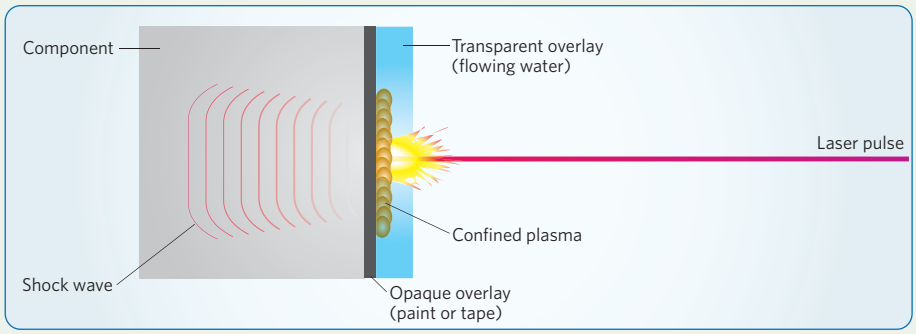

LSP TECHNOLOGIES

Figure B1 | Schematic of the laser-peening process.

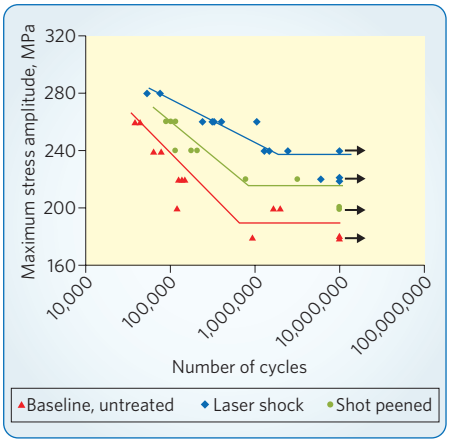

LSP TECHNOLOGIES

Figure 3 | Comparison of the fatigue property improvements for laser peening and shot peening.

LSP TECHNOLOGIES

Figure 4 | LSP Technologies' RapidCoater system positioned for processing a turbine engine blade.

Figure 3 shows a comparison of laser-peening and shot-peening fatigue properties for 7075-T7351 aluminium. For these tests, the specimens were fabricated with a notch to increase the stress concentration, thus making the test more severe. The data illustrate the typical fatigue enhancement of laser-peened parts, including a 30–50% increase in fatigue strength and about a tenfold increase in fatigue life.

Production applications of laser peening focused initially on aircraft engine parts such as turbine engine airfoils or integrally bladed rotors because of the benefits of preventing fatigue failures and improving damage tolerance for critical parts. GE Aircraft Engines (GEAE) used laser peening in 1997 to address a problem experienced with the B-1B Lancer F101 engine. Foreign object damage caused by hard objects ingested into the engine led to failures of first-stage titanium turbine engine blades. In some cases, sections of blades that broke loose caused irreparable damage to the rest of the engine. To avoid grounding the B-1B fleet, manual inspection of all the fan blades was required before each flight. The time-consuming inspections involved rubbing the leading edge with cotton balls, cotton gloves and even dental floss. If a single snag was detected, the blade was replaced before the next flight. More than one million man-hours per year were required to complete the engine inspections and keep the B-1B aircraft flying.

Laser peening was found to restore the fatigue performance of damaged blades to a standard equal to or better than the performance of new blades. Sensitivity to foreign-object damage up to about 6 mm deep in F101 blades was virtually eliminated. Using laser peening in this way avoided the costs of blade replacement, repair of secondary damage to engines and the severe consequences of catastrophic engine failures. Because of this success, laser peening was applied to solve problems caused by foreign-object damage for F-16 Falcon/F110 engine blades. In 2003, the use of laser peening was extended to more complex engine parts and laser peening began to be used during production of an integrally bladed rotor for Pratt and Whitney's F119-PW-100 engine, which powers the F/A-22 Raptor. The Metal Improvement Company also now operates laser-peening facilities and has used these to improve the performance of Rolls-Royce Trent series engine blades.

In addition to turbine engine components, numerous potential uses of laser peening for airframe structures exist, including fatigue-critical components such as F-16 bulkheads, wing attachments, flight control mechanisms, wheels, brakes and landing gear. The peening treatment is also commonly applied to improve the strength and reliability of welded ageing aircraft parts, fasteners and fastener holes, titanium and aluminium welded parts, and cost-effective castings for replacing forged parts.

Mobile laser-peening systems are now deployed at repair depots for treatment of large structures. The challenges for developing such a system primarily lie in providing control of the operating environment for the laser system. A mobile system must have embedded capabilities for vibration isolation, air and water temperature control, and air and water filtration, as well as protecting the operator and nearby personnel from laser light energy. LSP Technologies is developing a robust mobile system that is suitable for use in industrial settings and which is expected to be introduced in 2009.

Beyond the aerospace industry, numerous other industrial applications for laser peening are also emerging. Laser peening offers opportunities for weight reduction, increased reliability and improved fuel economy in automotive and truck parts such as transmission gears and axles, rotating engine parts and impellers. Medical applications include treatment of orthopaedic implants to improve the fatigue performance of hip and knee replacement joints and spinal fixation devices. Laser peening is also under development for applications in equipment for land-based power generation.

The future of laser shock processing is one of continuing advancement in applications, technology development and scientific research. The biggest barrier to wider application of laser peening in manufacturing has been the cost of high-power laser systems and, to a lesser extent, the slow throughput of the process. This situation has improved rapidly with the development of production laser-peening systems that are more reliable and easier to maintain, and with advances in processing technology such as LSP Technologies' RapidCoater system (shown in Fig. 4) for automating the application and removal of the process overlay coatings. The variety of potential uses continues to increase and is expected to expand rapidly over the next five years.

Many researchers are working on advanced modelling methods to predict and tailor the residual stress profiles that can be achieved with laser peening. Once these models are correlated and validated with fatigue performance, design engineers will be able to consider design life credits for incorporating laser peening into their component designs. ❐

Richard D. Tenaglia and David F. Lahrman are at LSP Technologies Inc., 6145 Scherers Place, Dublin, Ohio, United States.
e-mail: rtenaglia@lspt.com

WELDING

Welding plastic with lasers

Manuel Sieben and Frank Brunnecker

Laser welding of plastics is now a convenient and flexible technique that is proving popular for joining automotive parts and medical equipment as well as consumer products.

Most people are familiar with the welding of metals. Less well known is that welding is also an established technique in the production of plastic components — a method that is now indispensable to industry overall. Joining thermoplastics involves heating the material in the welding zone above its melting point so that it becomes plasticized. Unlike the welding of metals, plastics are usually welded without dispensing any additional material into the joint line.

A wide range of methods are used today for plastic welding. The difference between the technologies is not so much in how they work, but in the nature and type of energy source involved. Processes include friction welding methods (vibration and rotation welding), ultrasonic welding, microwave welding, high-frequency welding, hot-plate welding and laser welding. The method best suited for a particular application strongly depends on the properties of the plastics used as well as the application and its associated requirements. For instance, if the direct hot-plate welding technique is to be used (in which the plastic is brought into contact with a heated plate) the plastic should not stick to the hot plate; polycarbonate has this tendency and is therefore unsuitable for this method. Vibration welding is only suitable for flat components because the relative movement of the components causes damage otherwise. Although laser welding also has some restrictions, it does have many advantages over other techniques.

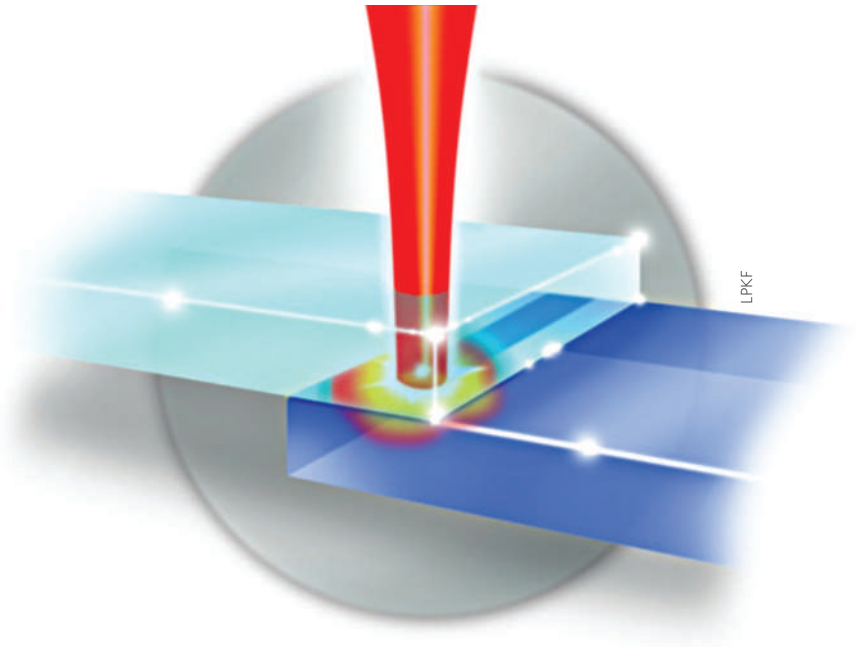

Figure 1 | Principle of laser transmission welding of two plastic components. The laser beam passes through the upper plastic layer but is absorbed by the lower one, generating heat that fuses the two components together, which then cool and harden.

LASER WELDING

People who recall the early years of laser welding technology tend to remember machines that took up a huge amount of space and required a great deal of maintenance. The solution to both of these problems lay in the further development of the laser sources. The breakthrough came with the replacement of the Nd:YAG laser by the modern diode laser which today typically offers a service life exceeding 20,000 hours, guaranteeing many years of problem-free industrial use. A prejudice that still lingers concerns the costs of a modern laser welding system, but the cost efficiency has been proven by usage in the highly cost-driven automotive industry.

The laser sources required for laser plastic welding are characterized by high output powers and continuous-wave operation. Wavelengths in the near-infrared range have proved particularly suitable for this purpose because in this wavelength region most engineering thermoplastics are transparent in an unpigmented state. These criteria were best satisfied in the past by Nd:YAG lasers with a wavelength of 1,064 nm. But because these solid-state lasers needed a lot of maintenance, they have been replaced by high-performance diode lasers. Modern systems achieve efficiencies of over 50% and completely dispense with complex and expensive water cooling — and thus benefit from reduced energy consumption.

When very fine seams are required, however, the diode laser reaches its limitations. Spot diameters of about 1 mm are realistic. To create even smaller weld seams, fibre lasers can be used. Because of their better beam quality and efficiency when compared with Nd:YAG systems, fibre lasers are clearly the better choice for this application, and seam widths of below 100 μm are achievable. These small seams are especially attractive for the medical industry and other fields following the trend of miniaturization. For example, microfluidics and 'lab-on-a-chip' systems are applications that cannot be welded by other technologies.

Laser welding of thermoplastics has moved on from niche applications to

become a highly interesting alternative to conventional methods. The hundreds of applications confirm the place that this technique has already earned itself in the industrial sector. Welding plastics using laser technology not only reduces the use of consumables, it also produces very good quality results compared with other welding techniques. Laser welding is a non-contact method that keeps mechanical stress on the components to a minimum. The only stress affecting the product being joined is the vertical joining pressure. There are absolutely no vibrations that could damage the plastic housing or any internal components. This is the key property that makes it so attractive for the production of electronic housings of all kinds, an application that largely drove the initial development of laser welding. To avoid any risk to the internal electronic components, electronic housings cannot be welded using ultrasonic methods. And because screwing or gluing the parts together is expensive, laser welding becomes the best choice.

TRANSMISSION LASER WELDING

Transmission laser welding is a very popular technique. The two parts to be welded together must have different transmission properties: that is, one of the components is transparent to the wavelength of the laser beam, whereas the other component absorbs the energy of the laser beam. Most lasers used today operate in the near-infrared range. During the joining process, the component is clamped, commonly using a sheet of glass. The laser beam passes through the clamping tool and the upper component, and when it hits the surface of the second component the light is absorbed and converted into heat (Fig. 1). This heat is then also passed into the transparent component by thermal conduction, causing the material of both components to melt. On cooling, the plastic hardens again to create a cohesive join. Absorption additives have now been developed to solve the problem of how to join two highly transparent components with the same transmission properties. An example is Clearweld, produced by Gentex Corporation. These green–yellow absorbers can be bound within suitable solvents and applied to the boundary surfaces. They have high absorption at the emission wavelengths of the laser beam used in each case. When the laser beam hits these absorbers, the absorber is heated up and plastifies the material by thermal conduction to produce a reliable join. The heat changes the optical properties of Clearweld, leaving behind a highly transparent seam (see Fig. 2). Transmission laser welding can be subdivided further according to the various means of guiding the laser beam along the joint line: simultaneous (described above), quasi-simultaneous and contour welding (both described below) are now all established in today's market.

QUASI-SIMULTANEOUS WELDING

Quasi-simultaneous welding — a mixture of contour and simultaneous welding — is particularly good for small components. The laser beam is guided along the welding line by a galvanometer scanner (Fig. 3). The beam is controlled in the x and y direction, and because of the high speed of the beam, the material along the whole welding seam melts 'quasi-simultaneously'. The programmability of the scanning unit makes this method very flexible: applying the process to new products or making corrections only requires that the machine is reprogrammed without having to change the optics or masks. Quasi-simultaneous welding is particularly good for components up to a maximum size of 400 mm × 400 mm, for larger components it tends to be unsuitable. Another restriction is that the third dimension of the component must not exceed the focusing depth of the laser. This method is therefore particularly good for welding flat parts, such as sensor and electronic housings.

CONTOUR WELDING

Contour laser welding makes it possible to join large components such as car body parts, car lights and solar panels. During contour welding, the laser beam is guided once along the weld line using a positioning system such as a robot. The robot either holds the laser itself, or is equipped with a fibre-coupled system and moves a focusing lens. This method is flexible and can be used in theory to join any size of component. Contour welding produces very shallow join depths, and the width of the welding seam is smaller than that produced using comparable processes. This makes it particularly interesting for transparent components and sunroofs, headlights, tail lamps or instrument units where weld seams are visible. Contour welding can also be used to process parts found in car engine compartments, with the advantage that the method produces no debris, so parts such as air-intake manifolds or liquid containers can be processed without having to carry out any post-process cleaning.

HYBRID WELDING

A recent development is 'hybrid' welding, which uses two emission sources to increase welding quality. Hybrid welding is an advanced form of classic contour welding and has already captured market share in many applications. This technique was jointly developed in 2005 as a result

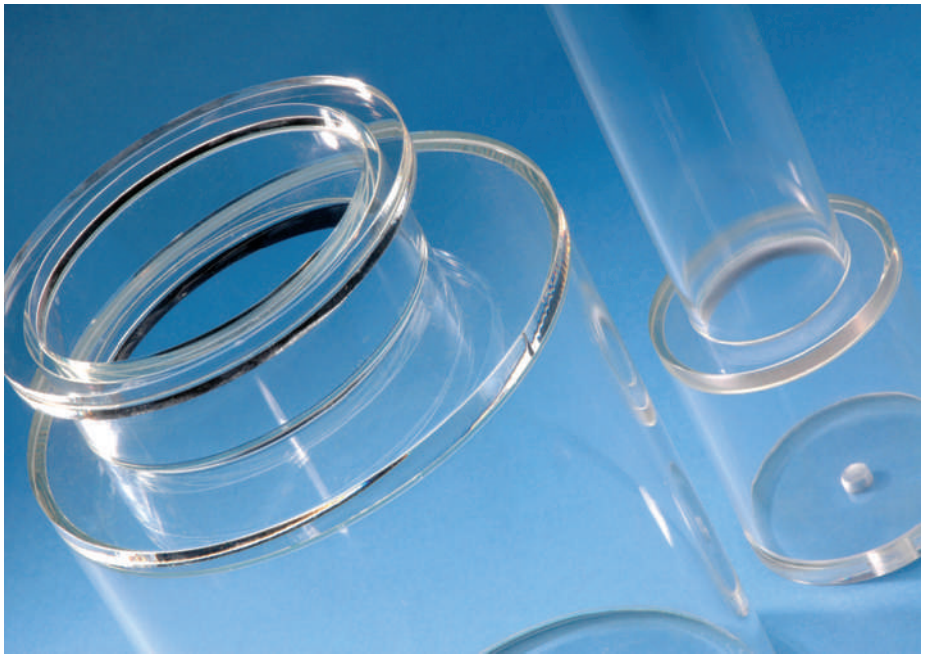

LPKF

Figure 2 | Example of high-quality laser welding of transparent plastic parts using the Clearweld technology. A light-absorbing dye is sandwiched between the components to be joined. On illumination with a laser it heats up, melting the interface between the parts. Advantageously, the dye becomes colourless in the process leaving a weld seam that is invisible to the naked eye.

LPKF

Figure 3 | Scanner-based welding system integrated into a conveyer line. The approach allows efficient mass production.

of cooperation between LPKF Laser and Electronics AG and the Bavarian Laser Centre (Erlangen, Germany). Instead of relying solely on energy provided by a laser, hybrid welding combines a laser beam with a secondary source of light that is polychromatic (wideband emission). Halogen lamps have proved to be suitable as the secondary source. In hybrid welding, the secondary radiation fulfils two different tasks. First, the spot diameter of the halogen light is much larger than the laser beam. So, when both sources are focused on the same point, they give a total radiation profile that decreases strongly on the outside with an intensity peak at the centre coming from the laser beam. When this set-up crosses a point on a welding line, the material is first slowly warmed, then melted by the laser beam, and then cooled slowly when it again passes into the area only influenced by the halogen light. The biggest advantage of hybrid welding is that it prevents a welding seam from cooling down too quickly, and so stops stresses building up in the material. Another advantage is the continuous spectrum of the halogen spot: whereas laser light passes almost completely unhindered through the transparent upper component, the upper layer absorbs a large proportion of the secondary radiation. This means that the upper transparent component is not exclusively warmed by indirect thermal conduction as is the case with the other laser welding methods. Direct absorption gives rise to a more homogenous temperature.

Hybrid welding is particularly suitable for components such as rear lights, tachometer units and other products where welding seams cannot be hidden. These joins mostly involve polymethylmethacrylate (PMMA) or polycarbonate as the upper component, and are currently usually joined by hot plate, vibration or ultrasonic welding. However, the advantages of the new hybrid welding technique are compelling and are attracting more and more attention. Conversion to the hybrid welding technology means that an entire processing step can be removed from a production line because annealing is no longer required. The system also has advantages in welding products where the priority is high productivity for small batches of products. By using a clamping roller to provide the required clamping force, hybrid welding completely dispenses with the otherwise essential upper tool (Fig. 4). This saves production costs, and the associated absence of any wear or contamination that otherwise increases the proportion of rejected goods.

LASERVISION

Figure 4 | A hybrid system with an example application of an automotive tail light.

LPKF

Figure 5 | Electric shaver welded by laser.

TOMORROW'S TRENDS

Different trends can now be observed in the market: the reduction in the cost of laser sources is increasingly making laser welding economical for more cost-sensitive applications such as consumer products (Fig. 5). There has also been growth in demand from the medical technology sector where guaranteed hygiene is often very important. Laser welding easily satisfies this stringent demand: unlike most conventional methods, laser welding produces absolutely no fluff or particles, a compelling argument for its use in the manufacture of infusion bags and similar products. The production of microfluidic systems is another large market involving the construction of the finest possible channels, which are difficult and expensive to produce using methods other than laser welding. The joint line here not only combines the components but can simultaneously create fluidic channels.

The size of components being welded is also growing steadily. It is now possible to use lasers to join plastic car body parts, rear lights or similar components. The automotive industry continues to be the main market for laser welding equipment. The current crisis affecting this industrial sector has made the search for cost-cutting measures even more important. The economic efficiency of traditional processes is now undergoing stringent analysis, and laser plastic welding is proving to be the most cost-effective alternative in many cases. If this trend continues, modern laser welding machines are set to capture even more of the market for plastic welding. ❐

Manuel Sieben and Frank Brunnecker are at LPKF Laser and Electronics, Gundstraβe 15, 91056 Erlangen, Germany.
e-mail: m.sieben@lpkf.de; f.brunnecker@lpkf.de

Profiling tool for metallic devices

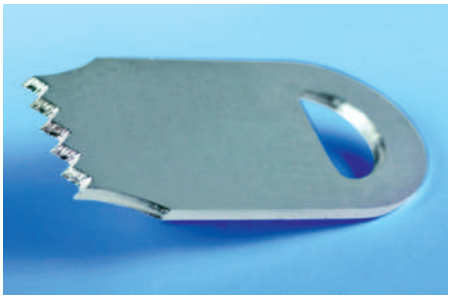

ROFIN-BAASEL UK LTD

Designed for high-precision profiling and cutting of metals used for making medical devices, the ES-CUT150 system is the latest release from ES Technology Ltd in the United Kingdom. The system, equipped with a 150-W pulsed YAG laser, is able to cut through metals up to 5.0 mm thick, and create a kerf width of only 18 μm with minimum burr, on materials such as stainless steels, titanium, aluminium, gold, silver and brass. The system operates at an accuracy of ±10 μm and speeds up to 35.0 mm s^{-1}, offering high-quality profiling at high speeds. The position of the workpiece to be processed is controlled by a servo-driven x–y table, and computer-aided design (CAD) data for the part to be produced can be imported quickly into the system. Other benefits include a computer-based operator–user interface, a full integrated standalone design, and an optional facility for fine dust removal.

www.estechnology.co.uk

Plug-and-play fibre laser

Following the recent opening of an application facility in Silicon Valley, California, in February 2009, IPG Photonics has announced a new line of fibre lasers designed for high flexibility and reliability at low cost. In addition to the fibre-delivered direct-diode lasers, the company now also supplies cost-effective customized fibre lasers that offer plug-and-play operation with rapid fibre replacement and switching capability. The new, compact YLS-CL series gives users choice over delivery fibre shape, output fibre core sizes and beam shapes. Compared with the direct-diode systems, the custom lasers offer high flexibility and reliability. Available at 2, 3 or 4 kW of output power, the lasers are specifically designed for cladding, brazing, hardening and annealing applications in the automotive, aerospace, oil and heavy industries. Mass production of this new-line fibre lasers is scheduled to be in the second quarter of 2009. The company says that the new line will be price-competitive.

www.ipgphotonics.com

Green laser offers high-precision micromachining

Coherent, a Californian company based in Santa Clara, has unveiled a new pulsed green laser: the AVIA 532-23. The announcement extends Coherent's AVIA 532 high-power laser series into the region of more moderate output power. Operating at a wavelength of 532 nm, the new AVIA laser is a frequency-doubled, Q-switched, diode-pumped solid-state laser that offers an average power of 23 W. It produces pulses with a pulse width of less than 40 ns at a repetition rate of 100 kHz. Just like other products in the series, the device comes with drift-free resonator optics and pump laser diodes with aluminium-free active area. It also features the ability to deliver constant pulse energy over time and at varying repetition rates, and promises uniform pulse energy when the laser is operated in burst mode (operation with groups of closely spaced pulses). Designed with excellent beam quality factor $M^2 < 1.3$ and high repetition rate of up to 300 kHz, this laser is capable of minimizing the heat-affected zone on a workpiece and is a cost-effective tool for a wide range of demanding, high-precision micromachining applications, such as solar-cell manufacturing, micromachining of micro-secure-digital (SD) cards, microelectronics package processing, and silicon wafer sawing and scribing.

www.coherent.com

Modular design for photovoltaics

4JET GmbH, a German supplier of laser systems for surface treatment of thin-film solar panels, has extended its range for products serving the photovoltaic industry with the INLINE system. Equipped with several laser technologies, the modular design of the INLINE system performs abrasion-free laser edge deletion, pattern-4 isolation cutting, selective perforation of semitransparent solar panels for building integration, marking and molybdenum exposure of thin-film panels, all from within a single unit. The design of the unit allows full-area processing including the inside of coated glass surfaces. Diode-pumped solid-state or fibre lasers are used, depending on the application. The laser edge deletion process provides a clean surface that has a resistance of several gigaohms and removes the need for further treatment before the lamination process. The system is suitable for processing amorphous silicon, cadmium telluride (CdTe) and copper–indium–gallium diselenide (CIGS) thin films, as well as all typical glass formats in use including G8 formats with 2,600 × 2,200 mm dimensions. The INLINE's combination of a high level of automation, cost-efficient design and abrasion-free precise ablation process not only reduces the cost of processing a panel, but also improves panel quality. Other features include an optical positioning system, vapour evacuation, integrated power measurement and optional modules for process validation.

www.4jet.de

Beam shaper suits industrial needs

MOLTECH GMBH

MolTech GmbH, based in Berlin, has released a new collimator model, the πshaper 37_34_1064, that provides highly efficient laser-beam shaping for high-power lasers. The device is designed to be compatible with powers of up to 6 kW from fibre-coupled solid-state or diode lasers, and near-infrared fibre lasers. It transforms a Gaussian or similar intensity distribution of the source laser beam to a flat-top beam with nearly 100% conversion efficiency and also accepts divergent TEM_{00} or multimode laser beams. The collimator maintains the diameter of the output beam at 30–34 mm over long distances with a uniformity of within 5%. Although it is designed for operation wavelengths of 1,020–1,100 nm, other optional wavelengths at 830 nm, 980 nm and so on are also available. The device is based on a Galilean design and no internal focusing of a beam is involved. Together with the ease of integration in systems and high damage threshold, the πshaper is attractive for applications in welding of metals and plastics, annealing, hardening, cladding, marking and engraving, and ablation.

www.pishaper.com

Combining fire and water

Swiss company Synova is commercializing an innovative materials processing technique that uses a water-guided laser beam to allow 'cold laser cutting'. **Nadya Anscombe** talks to the company's chief technical advisor, Alexandre Pauchard, to find out more.

What makes your company's laser MicroJet technology unique?

The technique combines the advantages of water and laser cutting for the first time in one operation. In the machine tool industry, water has been used for many years to cool a workpiece and remove waste. It has also been used as high-power jets for cutting. In our technology, the water does not cut, but instead a narrow jet simply guides the laser beam to the workpiece, cools the workpiece and removes waste. The water jet acts like an optical fibre, completely surrounding the laser beam and guiding it by internal reflection. This prevents the divergence of the laser beam and means the cutting head can be up to 10 cm away from the workpiece, giving the system great flexibility. The water jet is very thin — between 30 and 150 μm in diameter — and this allows precision cutting of sensitive material with negligible thermal influence.

What advantages does it have over conventional laser materials processing technology?

A conventional focused laser beam has a limited working distance of just a few millimetres, owing to beam divergence. In addition, the conventional laser generates a heat-affected zone in the material, causing damage. Contamination can also be an issue, as the molten material can be redeposited on the surface. Unlike conventional laser cutting where thermal damage is a problem, our cut is cooled by the water jet between laser pulses, producing what is effectively 'cold laser cutting'. This method significantly reduces deformation and heat damage, allowing the material to retain its original structure. With our system, complex three-dimensional cutting is also possible because of the long working distance and fibre-like delivery of the laser beam. It can be used effectively with complex profiles and contours where normal access would be impeded or impossible.

What are the main markets for your technology?

Our technology has a diverse range of applications. For example, in the photovoltaics industry our systems are used for omnidirectional cutting, drilling, scribing, grooving, edge grinding and marking. The semiconductor industry uses our systems for applications including wafer dicing, via-hole drilling, isolating and edge grinding of thin wafers. It can also be used in the medical industry for making stents, in the watch industry for fine cutting and in the automotive industry for the production of fuel injection nozzles. There has definitely been a slowdown in capital expenditure in most industries, but our sales into the automotive industry have not been as badly affected as other materials processing technologies. This is because fuel injection nozzles need to be changed regularly on all cars, so there is still a demand for making them. Our systems can make the nozzles much faster than conventional electro-discharge machining, so even in tough times it makes economic sense to invest in new equipment. And in the semiconductor industry our systems are replacing the well-established diamond saw technology because ours can cut any shape — hexagon or circle — so our system has a clear advantage.

Synova's Alexandre Pauchard: "With our system, complex three-dimensional cutting is possible because of the long working distance and fibre-like delivery of the laser beam."

What laser technology do your systems use?

The wavelength of the laser we use is limited by the absorption characteristics of water. Water has a minimum in its absorption coefficient at 530 nm. By a happy coincidence this wavelength corresponds to that of frequency-doubled YAG lasers. At a working distance of 2.5 cm, water has a 0.1% absorption in the green area of the spectrum, so this region is ideal. For some applications we use the standard YAG wavelength of 1,064 nm, where absorption by water is about 40%, and this is still acceptable for most applications. The maximum average power we use at the moment is about 200 W. We would ideally want up to 500 W power from a green laser, but this just does not exist at the moment. We are investigating the use of disk lasers, which would increase the available power at the required pulse width and allow even faster processing. We have also started using shorter pulsed lasers (10-ns duration), but because the water cools the workpiece, there is no need to go shorter than this.

How about future development of the technology?

As well as using different laser sources, we are also looking at using different liquids, instead of water, to guide the laser beam. This allows a process we call laser chemical processing. Together with the Fraunhofer Institute for Solar Energy Systems in Freiburg, Germany, we are developing a technique for the selective doping of silicon solar cells. Using phosphoric acid instead of water, our system is able to perform local diffusion at high speed and accuracy without the need for masks or any high-temperature processes such as annealing. The laser melts the surface of the silicon; the phosphoric acid mixes with this molten material; and the doped silicon then recrystallizes. Research has shown that this process can produce high-efficiency silicon solar cells with up to 20.4% efficiency. Its industrial implementation is expected to greatly reduce the cost of manufacturing selective-emitter solar cells. This technology is now close to maturity and we hope to introduce it to the market by the end of the year.

INTERVIEW BY NADYA ANSCOMBE

Nadya Anscombe is a freelance science and technology journalist based in the United Kingdom.

nature photonics

Interested in quantum optics and cryptography?

Nature Photonics is a monthly journal dedicated to research in all areas of light generation, manipulation and detection. Coverage extends from research into the fundamental properties of light and how it interacts with matter through to the latest designs of optoelectronic devices and emerging applications that exploit photons.

Research areas covered in the journal:

- Lasers, LEDs and other light sources
- Imaging, detectors and sensors
- Optoelectronic devices and components
- Novel materials and engineered structures
- Physics of light propagation, interaction & behaviour
- Quantum optics and cryptography
- Ultrafast photonics
- Biophotonics
- Optical data storage
- Spectroscopy
- Plasmonics
- Nonlinear optics
- Fibre optics and optical communications
- Solar energy and photovoltaics
- Displays
- Terahertz technology
- Nanophotonics
- X-rays

Quantum optics and cryptography is one of the many topics that *Nature Photonics* covers, papers published to date include:

- **Robust photonic entanglement distribution by state-independent encoding onto decoherence-free subspace**
  Takashi Yamamoto et al. (Volume 2, No 8)
- **An avalanche-photodiode-based photon-number-resolving detector**
  Beata Kardynal et al. (Volume 2, No 7)
- **Superconducting nanowire photon-number-resolving detector at telecommunication wavelengths**
  Aleksander Divochiy et al. (Volume 2, No 5)
- **High-frequency single-photon source with polarization control**
  Stefan Strauf et al. (Volume 1, No 12)
- **Photon-number-discriminating detection using a quantum-dot, optically gated, field-effect transistor**
  Eric Gansen et al. (Volume 1, No 10)
- **Quantum key distribution over a 40-dB channel loss using superconducting single-photon detectors**
  Hiroki Takesue et al. (Volume 1, No 6)
- **Semiconductor quantum light sources**
  Andrew Shields (Volume 1, No 4)
- **Quantum communication**
  Nicolas Gisin & Rob Thew (Volume 1, No 3)

Submit your next paper to *Nature Photonics*

Nature Photonics **covers the entire spectrum of photonics research for scientists in academia and industry. Visit www.nature.com/naturephotonics and click on the guide to authors for further information.**

www.nature.com/naturephotonics

nature publishing group npg

Now showing.

Visit our new Multimedia Gallery at **www.Breault.com/movies** and see optical engineers as they discuss features and applications of the world's most sophisticated optical software, ASAP.

Topics covered include:

- NEW Solar Energy
- Aerospace / Sensing
- Architectural Lighting
- Automotive Lighting
- Aviation Lighting
- Bio-Optics
- Defense Systems
- Display Systems
- Electronics
- Optical Design
- Telecommunications

See firsthand why optical engineers and designers in 35 countries choose ASAP for their virtual prototyping needs, and witness the unmatched capability, flexibility, speed, and accuracy of ASAP.

Breault.com/movies

Breault Research — Taking Light Further

USA | Canada 1.800.882.5085
Worldwide 1.520.721.0500

Breault.com

nature photonics

LETTERS

PUBLISHED ONLINE: 26 APRIL 2009 | DOI: 10.1038/NPHOTON.2009.67

Co-existence of strongly and weakly localized random laser modes

Johannes Fallert*, Roman J. B. Dietz, Janos Sartor, Daniel Schneider, Claus Klingshirn and Heinz Kalt

Recent theoretical work on random lasing predicts that the occurrence of narrow lasing spikes can be caused by both localized and extended modes of light[1–3]. Typical random lasing spikes have been observed in powders of zinc oxide nanoparticles[4], but identifying the possible degrees of localization of such modes has until now been an open issue[5]. In this Letter we present an experimental procedure that directly extracts the area of localization of the modes. This method relies on the investigation of micro-structured fields of zinc oxide powder, which also allows direct correlation to the local structural properties of the ensemble of subwavelength particles by scanning electron microscopy. We find that lasing from both localized and extended modes can be observed simultaneously. Our observation also corroborates the prediction that localized modes have a lower loss rate than that of extended modes[5].

Random lasing is a phenomenon only recently discovered in various disordered media, which has potential for applications in photonics. In a random laser, light is confined within an amplifying disordered medium due to permanent scattering on a microscopic length scale. The light is thus retarded from leaving the active region up to the limit of localized light[6,7]. The localization of light is caused by constructive interference, because elastic scattering of light is a completely coherent process. Typically, amplification in such a laser is achieved by introducing a laser dye, or the scattering structure is excited to deliver optical gain itself[5,8]. One example of these bifunctional (scattering and amplifying) random media is nanocrystalline ZnO powder. ZnO powders are ideally suited for application in random lasers because of their relatively high refractive index ($n_{ZnO} \approx 2.3$ in the ultraviolet near-bandedge region) leading to strong light scattering in combination with an adequate optical gain if sufficiently excited[4,9]. The onset of lasing is demonstrated typically by a threshold-like behaviour of the optical emission[4], but only under certain conditions do narrow laser lines, similar to those of conventional lasers, occur[10]. The origin of such spectrally narrow laser lines is still open to interpretation. It has been attributed to strongly localized modes of the light in the sense of an Anderson localization[11] that cannot be explained in a purely diffusive model where interference effects are neglected[1]. However, numerical calculations in two dimensions have shown that extended modes can also lead to narrow laser lines in an amplifying random medium[2,3,12]. Recent experiments have shown that strongly localized modes can be found in a disordered medium of gallium phosphide filled with a laser dye[13]. In this experiment only a small local area with a diameter of 2 μm could be excited, so extended modes are in principle suppressed.

The focus of this work is to check the predictions of the conflicting theories by directly probing the degree of localization of random laser modes in a system where both kinds of modes can in principle be excited. As a model system we use nanocrystalline ZnO powder with a mean particle size of 260 nm (see Methods).

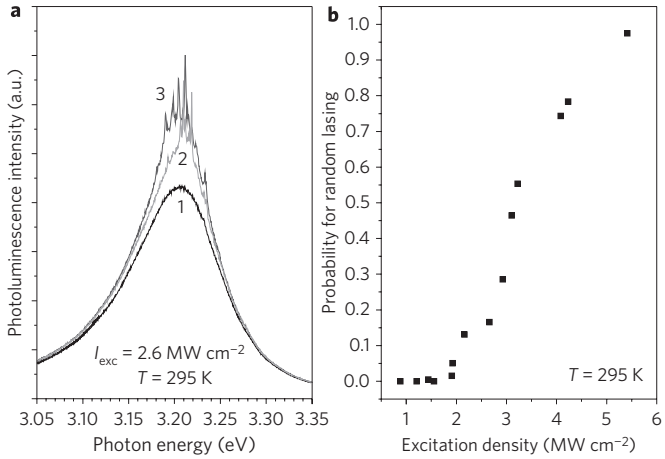

Figure 1 | Fluctuations of random lasing in extended samples. **a**, Photoluminescence spectra of an extended volume (2 mm in diameter, 1 mm thickness) of nanocrystalline ZnO powder, obtained by single excitation shots under the same condition of $I_{exc} = 2.6$ MW cm^{-2} and an excitation area with a diameter of 300 μm. The occurrence of random lasing can be identified by the change in the lineshape of the emission, which shows spectrally narrow spikes. Although spectrum 1 shows no random lasing it can be observed in spectra 2 and 3. **b**, The probability for the occurrence of random lasing shows a clear threshold behaviour. For the investigated ensemble a threshold value of ~2 MW cm^{-2} is observed.

For direct observation of the localization degree of random lasing modes it is essential to use investigation methods with high spatial resolution. We therefore used a micro-photoluminescence (μ-PL) setup in which the origin of stimulated emission can be determined with a spatial resolution of 1 μm. Second, we deposited the nanocrystalline powders in 10-μm-sized depressions etched into a GaAs substrate. This allowed the observed luminescence pattern to be matched directly to the corresponding structural image obtained using a scanning electron microscope (SEM). This was important to rule out the presence of microsized (≥1 μm) particles that could have served as single resonators.

To measure random lasing in a quasi-stationary regime we used a laser excitation source with pulses of 5 ns. This is well above the lifetime of the electron–hole plasma created under the relevant optical pumping conditions[14]. Typically for spatially extended fields of random laser media pumped by nanosecond excitation above laser threshold, there were strong fluctuations in the observed emission[15]. This is shown in Fig. 1a for the case of an extended area of ZnO powder in which the emission varies from shot to shot. However, a threshold-like behaviour can be identified when considering the shot-to-shot probability for the occurrence of random lasing (Fig. 1b). This situation improves dramatically when addressing the

Institut für Angewandte Physik, Universität Karlsruhe (TH), Wolfgang-Gaede-Strasse 1, 76131 Karlsruhe, Germany. *e-mail: jfallert@aph.uni-karlsruhe.de

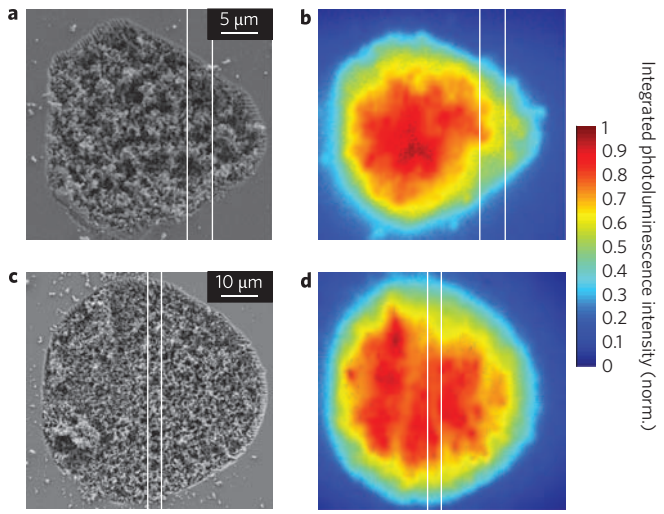

Figure 2 | Microscopically defined fields of ZnO nanoparticles. **a**,**c**, SEM images of two structured fields. Note the different length scales. The fields have different planar extensions, but a similar depth of 5 μm. **b**,**d**, Spatially resolved total photoluminescence of the respective fields at room temperature and an excitation density of 2.5 MW cm^{-2}. The signal is taken by an accumulation of 20 excitation pulses. The area between the white lines indicates the area from which the photoluminescence of Fig. 3 is taken.

spatially restricted ensembles in the micro-depressions. Here one observes only minor shot-to-shot fluctuation in the lasing spectrum.

We now focus on emission from these microscopically defined fields of ZnO nanoparticles. On the one hand the number of possible modes for random lasing is significantly reduced there compared to an extended sample. This allows the observation of individual modes defined by the microscopic arrangement of the nanocrystals, as shown in the following. On the other hand, the whole fields are optically excited from their top side, and the areas with diameters in the range of several tens of micrometres are still large enough to allow strongly localized and extended modes, in contrast to the experiment described in ref. 13. The depth of the optical excitation perpendicular to the surface is limited to the upper micrometre where the excitation light is absorbed. SEM images of two structured depressions filled with nanocrystalline ZnO powder are shown in Fig. 2a and c. Figure 2b and d shows the colour-coded spatial distribution of the luminescence intensity of the same fields. Clearly, the total photoluminescence intensity decreases in the vicinity of the absorbing GaAs boundary. More important, however, the main part of the emitting field displays distinct and stable fluctuations in the spatial intensity distribution.

To really extract the spatial extension of individual modes from these emission distributions it is necessary to add spectral resolution, as shown in Fig. 3. The modal structure of the emission is obvious from the occurrence of several spectrally narrow lines dominating the total photoluminescence. The spatial resolution in the vertical dimension allows the extraction of the extension of each particular mode in this direction.

It is found that most of the lasing modes are extended over the whole diameter of the ZnO field. Additionally, a smaller number of modes appears to be confined to a diameter of around 1 μm, as deduced from the full-width at half-maximum of the spatial profile. This is, for example, the case for the peak at 3.16 eV in Fig. 3a and the peak at 3.24 eV in Fig. 3b. This first interpretation is completed by a raster scan of the fields in the horizontal dimension. The strong confinement of the addressed modes is clearly verified, while the extended modes also have a large extension in the second dimension. Examples of both types of modes are shown in Fig. 4. Because the modes are located near the surface of the strongly scattering powder,

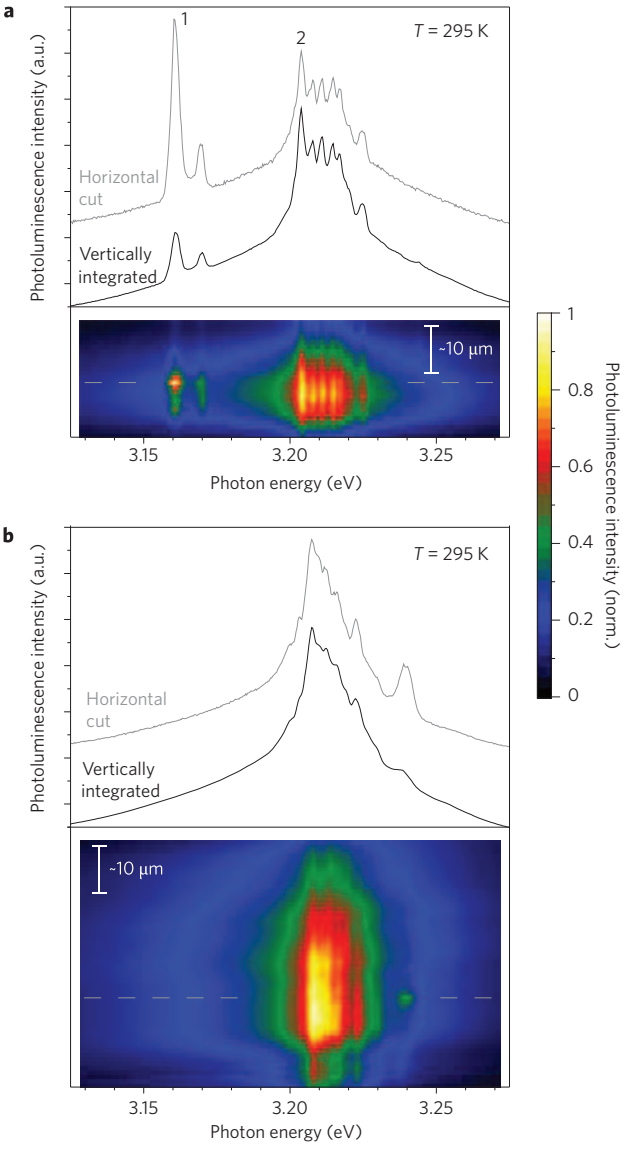

Figure 3 | Spectrally and spatially resolved photoluminescence. **a**,**b**, The spectrally resolved photoluminescence is taken from a vertically extended and horizontally limited (to 3.5 μm) spatial region, marked by white lines in Fig. 2a,b (**a**) and in Fig. 2c,d (**b**). In the bottom panels the photoluminescence intensity is shown colour-coded, with a spatial resolution in the vertical dimension. In the top panels, the vertically integrated photoluminescence is shown as well as for a cut along the dashed line in the bottom panels. The spectra have been taken as integration over 125 excitation pulses with $I_{exc} = 2.5$ MW cm^{-2}.

the measurement displays a valid determination of the mode extent, as elaborated in the Methods.

Because the mode pattern is stable for the integration over a multitude of excitation pulses it is safe to assume that the modes have a fixed correlation to the structural details of the ZnO powder. Owing to the fact that micro-structured fields were used, we can easily allocate the position of the strongly localized modes in the SEM images of the sample. At the relevant positions no grains can be found that have a shape and size that would be sufficient for them to act as individual isolated resonators. Thus the observed emission lines can be attributed to modes provided by the random but specific alignment of the ZnO nanoparticles at a certain position within the field.

Now we want to address the question of the type of localization leading to the observed lasing spikes in the spectrum. Anderson

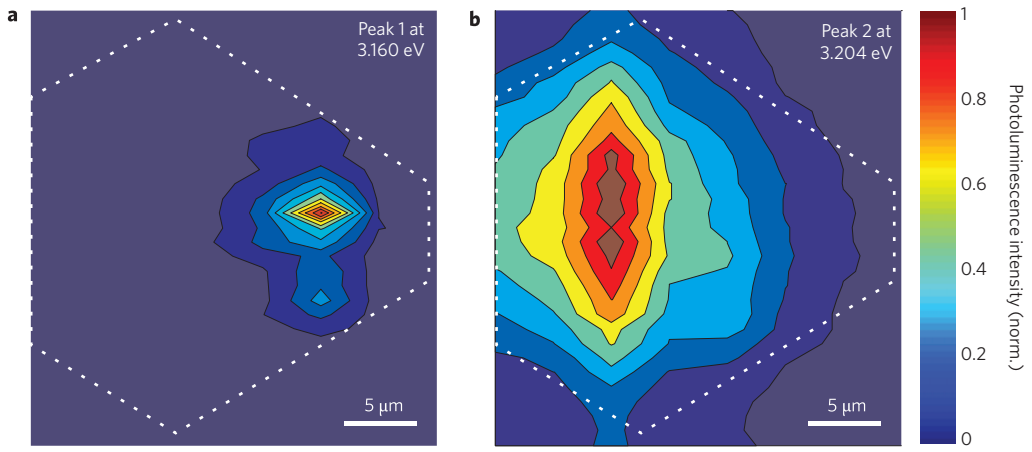

Figure 4 | Two-dimensional mode extent. a,**b**, Mode expansion in two dimensions for the two peaks labelled as 1 (**a**) and 2 (**b**) in Fig. 3a. The dashed line indicates the geometry of the structured field as shown in Fig. 2a.

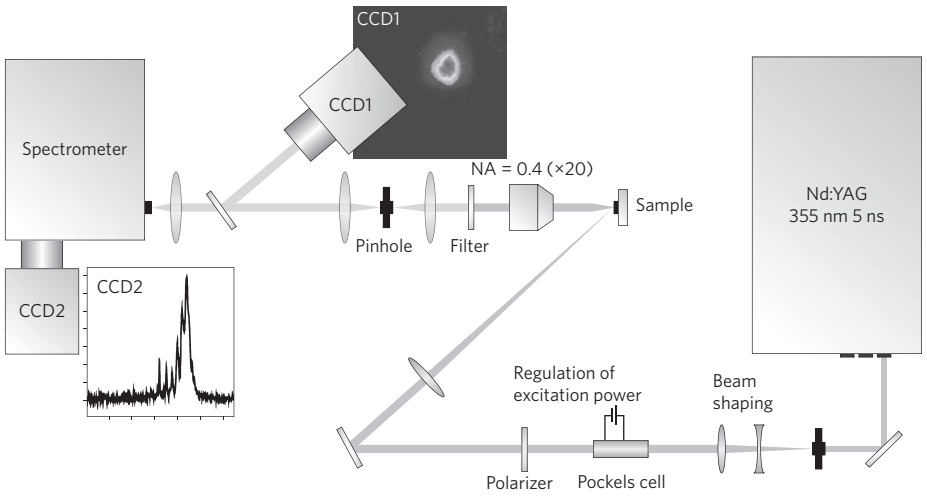

Figure 5 | The experimental set-up. CCD1 is used for the two-dimensional imaging of the spectrally integrated photoluminescence. CCD2 detects the spectrally resolved photoluminescence with a spatial resolution only in the vertical dimension.

localization of the light is a possible candidate to explain the observed strongly confined laser modes, because the random medium is strongly scattering. With average particle sizes just under the vacuum wavelength for the ZnO powder considered here, the borderline described by the Ioffe–Regel criterion $kl_m \leq 1$ is nearly fulfilled[5]. Here k describes the wavevector of light and l_m its mean free path. Considering that strong localization of light has been observed up to $kl_m \approx 4$ in time-resolved transmission measurements[16], it is plausible that Anderson localization can be achieved in the investigated sample. An alternative mechanism for the occurrence of strong spatial localization is based on fluctuations in the refractive index leading by chance to waveguiding structures; this was predicted in ref. 17. Both mechanisms lead to strongly localized modes that are connected with a high Q-factor (or a low loss rate), in contrast to the extended modes[3]. The result of this is that the localized modes that can be caused by the two mechanisms need a much lower gain to support lasing modes than do the latter. This is consistent with our experimental observations. All of the extended modes are found in the spectral region at 3.21 ± 0.02 eV. This is the region where the highest gain from an inverted electron–hole-plasma is observed in ZnO at room temperature for the considered excitation density, excitation wavelength and pulse duration, as can be extracted from Fig. 1a or is also found in ZnO nanorods[18]. Because saturation effects are predicted to be of less importance for extended than for localized modes[5], they can dominate the spectrum in this spectral region. Strongly localized modes, however, are observed at spectral positions below or above this interval where the gain is expected to be lower.

In summary, we have developed an experimental method that gives direct access to the localization degree of random lasing modes. We show for the case of ZnO nanoparticle powders that strongly localized random lasing modes co-exist with modes of much larger spatial extension. The extended modes are primarily found in the spectral region where the gain is expected to be highest, whereas the strongly localized modes are found in regions where the available gain is lower, consistent with the expected influence of the respective Q-factors.

Methods

The nanocrystalline ZnO powder. The nanocrystalline ZnO powder used in this research provided a mean particle size of 260 nm (Emprove, from Merck). We found that this particular powder had the lowest threshold for random lasing, when compared to several others with smaller or larger mean particle sizes. A comparison of the random lasing properties of powders with different particle size distributions can be found in ref. 19. Studies on the linear optical properties of these powders can be found in refs 20 and 21. The fact that the lowest threshold for random lasing is found for the powder with a mean particle size of 260 nm agrees

with scattering theory, which predicts the highest scattering efficiency for particles with sizes in the range of the effective wavelength in the medium[22,23].

Fabrication of structured fields of nanocrystalline ZnO powder. Micro-structured fields of nanocrystalline powder were fabricated by etching depressions into a GaAs substrate, which were then filled with the powder described above. The size of the depressions was defined by photolithography. After etching for 2 min in a solution of H_2O, H_2O_2 and H_3PO_4 (volume ratio 8:3:1), ~5 μm of GaAs was etched isotropically. After the resist was removed a mixed paste of ZnO powder and ethanol was swept over the whole sample using a razor blade. The ethanol was subsequently evaporated, leaving the bare ZnO powder in the micro-structured depressions with a depth of 5 μm.

Experimental details of the micro-photoluminescence measurement. The experimental setup for the performed optical measurements is shown in Fig. 5. The samples were optically excited by a frequency-tripled Nd:YAG laser at 355 nm (3.49 eV) with pulses of 5 ns duration to achieve a quasi-stationary excitation condition. Excitation power was regulated with a Pockels cell in combination with a linear polarizer. Owing to the high absorption coefficient $\alpha \approx 1\times10^5$ cm^{-1} (ref. 24) of ZnO, above its bandgap energy the excitation light will be absorbed in the upper region of the sample.

A microscope objective was used to resolve the photoluminescence emitted through the top surface of single micro-structured fields. The photoluminescence was dispersed and recorded by a spectrometer and a UV-enhanced charge-coupled device (CCD; CCD 2) in the imaging mode. In this setup the luminescence was spatially resolved in the vertical dimension of the CCD chip, with a high spatial resolution of around 1 μm. The signal was also spectrally resolved in the horizontal dimension with a spectral resolution of 1 nm. An additional CCD (CCD 1) allowed the simultaneous imaging of the spectrally integrated and two-dimensionally spatially resolved photoluminescence.

Direct measurement of the mode extent. The upper boundary of the spatial extent of random-lasing modes was determined by the fact that losses have to be compensated by optical gain. The losses occur on the characteristic length scale of the mean free path for light scattering. Monte Carlo simulations assuming mean free paths of up to 3 μm, which is a generous upper estimate for the ZnO powder used, showed that this is the maximum length scale of light propagation through the highly scattering medium without optical amplification. The latter is provided by the inverted electron–hole plasma[9], which was created only within a 1-μm-thick surface layer of the powder due to the strong absorption of the pump light. Thus we can exclude the possibility that optical modes extend deep into the sample. Also, it is not possible that a strongly confined mode appears as an extended one due to pure propagation of light within the powder. We can conclude that the spatial extent of the signal is a direct measure of the mode extent. We define the laser mode extent as the area in which the light of the specific resonance-wavelength is amplified significantly by means of stimulated emission.

Received 24 November 2008; accepted 23 February 2009; published online 26 April 2009

References

1. Vanneste, C. & Sebbah, P. Selective excitation of localized modes in active random media. *Phys. Rev. Lett.* **87,** 183903 (2001).
2. Mujumdar, S., Ricci, M., Torre, R. & Wiersma, D. S. Amplified extended modes in random lasers. *Phys. Rev. Lett.* **93,** 053903 (2004).
3. Vanneste, C., Sebbah, P. & Cao, H. Lasing with resonant feedback in weakly scattering random systems. *Phys. Rev. Lett.* **98,** 143902 (2007).
4. Cao, H. *et al.* Random laser action in semiconductor powder. *Phys. Rev. Lett.* **82,** 2278–2281 (1999).
5. Wiersma, D. S. The physics and applications of random lasers. *Nature Phys.* **4,** 359–367 (2008).
6. Wiersma, D. S., Bartolini, P., Lagendijk, A. & Righini, R. Localization of light in a disordered medium. *Nature* **390,** 671–673 (1997).
7. John, S. Strong localization of photons in certain disordered dielectric superlattices. *Phys. Rev. Lett.* **58,** 2486–2489 (1987).
8. Cao, H. in *Waves Random Media* **13,** R1–R39 (2003).
9. Klingshirn, C. ZnO: From basics towards applications. *Phys. Stat. Sol. (b)* **244,** 3027–3073 (2007).
10. Markushev, V. M., Ryzhkov, M. V. & Briskina, C. M. Characteristic properties of ZnO random laser pumped by nanosecond pulses. *Appl. Phys. B* **84,** 333–337 (2006).
11. Anderson, P. W. Absence of diffusion in certain random lattices. *Phys. Rev.* **109,** 1492–1505 (1958).
12. Türeci, H. E., Ge, L., Rotter, S. & Stone, A. D. Strong interactions in multimode random lasers. *Science* **320,** 643–646 (2008).
13. van der Molen, K. L., Tjerkstra, R. W., Mosk, A. P. & Lagendijk, A. Spatial extent of random laser modes. *Phys. Rev. Lett.* **98,** 143901 (2007).
14. Fallert, J. *et al.* Lasing dynamics in single ZnO nanorods. *Opt. Express* **16,** 1125–1131 (2008).
15. Anglos, D. *et al.* Random laser action in organic–inorganic nanocomposites. *J. Opt. Soc. Am. B* **21,** 208–213 (2004).
16. Aegerter, C. M., Störzer, M., Fiebig, S., Bührer, W. & Maret, G. Observation of Anderson localization of light in three dimensions. *J. Opt. Soc. Am. A* **24,** 23–27 (2007).
17. Apalkov, V. M., Raikh, M. E. & Shapiro, B. Random resonators and prelocalized modes in disordered dielectric films. *Phys. Rev. Lett.* **89,** 016802 (2002).
18. Fallert, J. *et al.* Lasing in single ZnO nanorods after fs- and ns-pulsed excitation. *Phys. Stat. Sol. (c)* **6,** 449–452 (2009).
19. Fallert, J. *et al.* Random lasing in ZnO nanocrystals. *J. Luminescence* in the press (2009).
20. Fallert, J. *et al.* Surface-state related luminescence in ZnO nanocrystals. *J. Appl. Phys.* **101,** 073506 (2007).
21. Hauser, M. *et al.* Absolute external luminescence quantum efficiency of zinc oxide. *Appl. Phys. Lett.* **92,** 211105 (2008).
22. Wu, X. H. *et al.* Random lasing in closely packed resonant scatterers. *J. Opt. Soc. Am. B* **21,** 159–167 (2004).
23. John, S. Electromagnetic absorption in a disordered medium near a photon mobility edge. *Phys. Rev. Lett.* **53,** 2169–2172 (1984).
24. Yoshikawa, H. & Adachi, S. Optical constants of ZnO. *Jpn. J. Appl. Phys.* **36,** 6237–6243 (1997).

Acknowledgements

This work was financially supported by the Deutsche Forschungsgesellschaft (DFG) in the framework of project KL345/23-2.

Author contributions

All authors have contributed to this paper and agree to its contents.

Additional information

Reprints and permission information is available online at http://npg.nature.com/reprintsandpermissions/. Correspondence and requests for materials should be addressed to J.F.

nature photonics

LETTERS

PUBLISHED ONLINE: 19 APRIL 2009 | DOI: 10.1038/NPHOTON.2009.47

Electrical detection of confined gap plasmons in metal–insulator–metal waveguides

Pieter Neutens[1,2]*, Pol Van Dorpe[1], Iwijn De Vlaminck[1], Liesbet Lagae[1] and Gustaaf Borghs[1]

Plasmonic waveguides offer promise in providing a solution to the bandwidth limitations of classical electrical interconnections[1–3]. Fast, low-loss and error-free signal transmission has been achieved in long-range surface plasmon polariton waveguides[4,5]. Deep subwavelength plasmonic waveguides with short propagation lengths have also been demonstrated[6,7], showing the possibility of matching the sizes of optics and today's electronic components. However, in order to combine surface plasmon waveguides with electronic circuits, new high-bandwidth electro-optical transducers need to be developed. Here, we experimentally demonstrate the electrical detection of surface plasmon polaritons in metallic slot waveguides. By means of an integrated metal–semiconductor–metal photodetector, highly confined surface plasmon polaritons in a metal–insulator–metal waveguide are detected and characterized. This approach of integrating electro-optical components in metallic waveguides could lead to the development of advanced active plasmonic devices and high-bandwidth on-chip plasmonic circuits.

The operation of surface plasmon waveguides has mainly been demonstrated using optical techniques such as scanning near-field microscopy and spectroscopy for mid- and long-range surface plasmon polariton (SPP) waveguides[8] and also for short-range metallic waveguides with high field confinement[9]. Although such methods provide excellent means to probe the properties of surface plasmons, none can be readily integrated into active plasmonic devices. Recently we demonstrated the electrical detection of surface plasmons by a GaAs photoconductor coupled to a plasmonic cavity[10]. Others, meanwhile, have realized SPP enhanced photodetectors[11,12]. These approaches, however, suffer from bandwidth limitations, or make use of weakly confined plasmonic modes. In this Letter we demonstrate remote electrical detection of a strongly confined SPP mode in a scalable high-bandwidth metallic waveguide. To this end we combine a metal–insulator–metal (MIM) waveguide with an inherently fast nanoslit metal–semiconductor–metal (MSM) photodetector, resulting in a scheme that is scalable down to the nanoscale, enabling a fully operational plasmonic circuit on a very small footprint.

MIM waveguides offer the prospect of combining high spatial field confinement and micrometre-range propagation lengths[13,14]. Metal-based waveguides provide a unique opportunity to send electrical and optical signals through the same guides. Here we make use of this feature by using metal slabs for direct electrical contacting of a MSM photodetector structure. MSM photodetectors provide an extremely fast photo response and a high signal-to-noise ratio[15,16]. A schematic of the waveguide-integrated MSM detector is shown in Fig. 1a. A detailed process flow is described in the Methods. The structures were fabricated on a semi-insulating GaAs wafer. By means of molecular beam epitaxy a 1-μm-thick undoped GaAs layer was grown as the active layer for the photodetector. The MIM waveguide consisted of a gold (100 nm)/hydrogen silsesquioxane (HSQ) (90 nm)/gold (160 nm) layer stack. A 300-nm-wide subwavelength slit was fabricated in the bottom gold layer, providing two detector contacts and at the same time allowing excitation of localized plasmonic modes in the slit. Excitation of a SPP mode in the waveguide was achieved with a 300-nm slit etched into the top metal layer. The distance between injection and detection slit was varied from 0 to 12 μm in steps of 1 μm. A side-view scanning electron micrograph (SEM) of a fully processed device is presented in Fig. 1b.

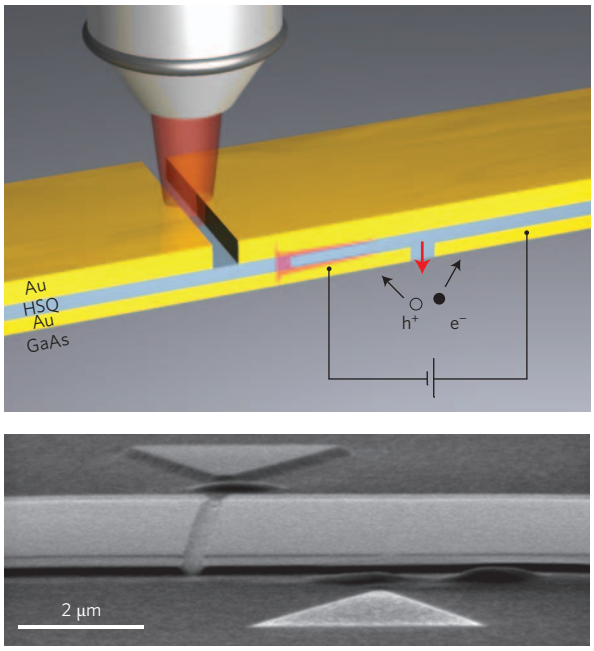

Figure 1 | Structure of the waveguide-integrated MSM detector. **a**, Schematic representation of the MIM–MSM device. **b**, SEM image of the device. The position of the injection and detection slit are marked by the large arrowheads.

We rigorously modelled and optimized the device by performing two-dimensional numerical calculations using Comsol Multiphysics (www.comsol.com; see Methods). Simulated normalized electric field profiles for transverse electric (TE) ($E \| z$-axis) and transverse magnetic (TM) ($E \perp z$-axis) polarization are shown in Fig. 2a and b, respectively. The entire structure is illuminated by a plane wave propagating in the $-y$-direction. Owing to the one-dimensional geometry of the injection slit, we do not expect efficient SPP excitation when E is set parallel to the z-axis (H perpendicular). Note that in experiments and calculations reported by another group[6] for silver/SiN_4/silver MIM waveguides, it has been found that

[1]IMEC, NextNS group, Kapeldreef 75, Leuven, Belgium, [2]Department of Physics, University of Leuven, Celestijnenlaan 200 D, Leuven, Belgium.
*e-mail: Pieter.Neutens@imec.be

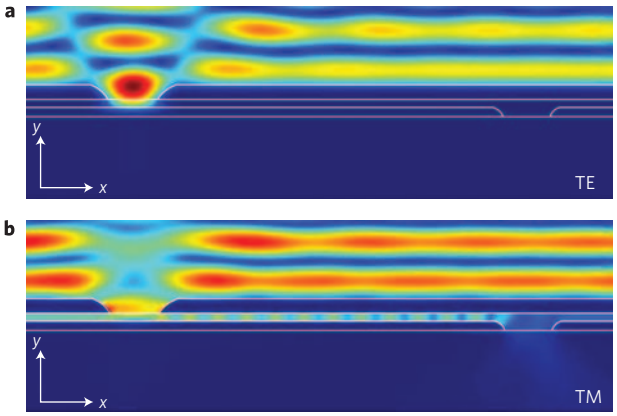

Figure 2 | Numerical calculations for plane wave excitation. **a**, TE polarization. The calculated normalized electric field profile for a MIM–MSM device with a 3-μm centre-to-centre distance between injection and detection slit shows no SPP transmission. **b**, TM polarization. Here, a local mode is excited in the injection slit, which couples efficiently to a propagating waveguide mode.

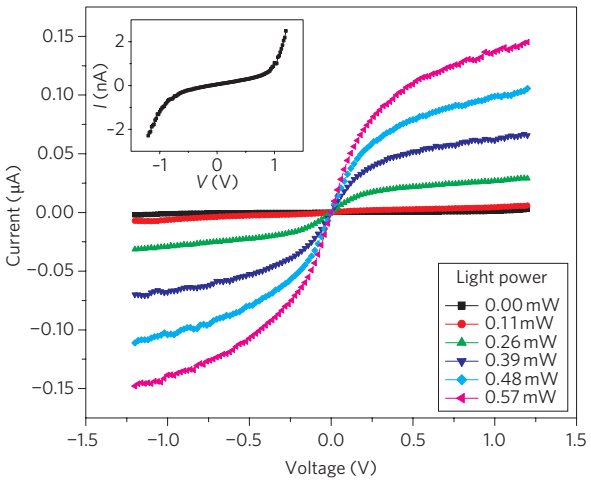

Figure 3 | *I–V* curves for different laser intensities. Current amplifications up to 600 are measured. The dark current is presented more clearly in the inset of the figure, revealing a clear back-to-back Schottky characteristic.

conventional waveguide modes with very short propagation distances can be addressed for small free-space wavelengths (<600 nm) in TE polarization where the thickness of the insulating layer exceeds 100 nm. Given the wavelength range of interest in our experiments (600–875 nm) and taking into account the lower-index HSQ core ($n = 1.43$), we do not expect contributions of conventional waveguide modes or plasmonic modes in the TE polarization. For TM polarization, the plane wave excites a local plasmonic mode in the injection slit that couples very efficiently to a propagating mode in the waveguide located in its near field. Simulations (data not shown) indicate that for excitation wavelengths from 650 nm to 875 nm, respectively, 40 to 65% of the light falling onto the slit couples to SPPs. The coupling mechanism is nicely illustrated in Fig. 2a, b by the interference patterns above the waveguide. Although the interference pattern vanishes above the slit for TM polarization (because there is little reflection due to a good modal coupling between the light incident to the slit and the waveguide mode), the interference pattern is still present for TE polarization.

SPP detection is established by coupling back to a local mode governed by the subwavelength detection slit. Coupling to the local plasmonic mode in the detection slit is achieved with an efficiency of more than 60% for wavelengths between 700 and 850 nm. The largest loss is caused by partial transmission of SPPs across the detection gap. Only a small ratio (<5%) is reflected (data not shown). The large index of GaAs leads to strong modal confinement in a volume of the semiconductor located right between the electrodes of the MSM detector. The modal confinement largely restricts photoabsorption to a small area in the semiconductor corresponding to the high-electric-field region, thereby greatly reducing the average collection distance and transit times.

Monte Carlo simulations performed previously on interdigitated epitaxially grown GaAs MSM detectors with narrow gaps[17] demonstrated intrinsic response times ranging between 0.25 and 3 ps for gap widths between 25 and 500 nm, making this type of detector very suitable for high-bandwidth applications. By fabricating MSM detectors with similar gaps and taking advantage of plasmon-enabled modal confinement, similar or shorter photoresponse times are feasible for our samples. For example, for our (experimentally realized) gap widths of 40–300 nm we can tentatively calculate the drift dominated response time of our MSM detector as $\tau = 0.3$–2.5 ps. To account for *RC* delays, we calculated the capacitance of our devices. Device capacitance is dominated by the parallel plate capacitance of the MIM waveguide. Based on work by Chou and colleagues[18] and using their equation $f_{3dB} = 0.441/t$, where t is the response time, we can also conclude that the resulting transit-time-limited bandwidth for these devices varies from 176 GHz for 300-nm-wide gaps to 1,470 GHz for 40-nm-wide gaps. The *RC*-limited bandwidth varies between 240 GHz (width of the waveguide, 5 μm; length, 20 μm) and 909 GHz (width of the waveguide, 1 μm; length, 20 μm), which means that for the present device the bandwidth is in practice transit-time limited.

All the experimental results presented here were obtained on MIM waveguides with a bottom metal layer width of 6 μm. To determine the optimum bias voltage for the detector, *IV* curves were measured as a function of the laser output power on a waveguide with a 300-nm gap and zero displacement between injection and detection slit. The resulting graphs are presented in Fig. 3. An autoscaled curve of the dark current is shown in the inset, revealing extremely low dark currents up to 300 pA in the linear regime, illustrating the high quality of the MSM detectors. The highest shot-noise-limited signal-to-noise ratio (1×10^3 at modest light intensity) is found when a voltage of around 0.5 V is applied across the detector. Consequently, the bias voltage is set to 0.5 V in all of the following measurements. By measuring the laser power incident on the detector and the corresponding photocurrent, we calculated the detectors' external quantum efficiency to be 8.9–34.3% for 1–10 V.

In a first set of experiments we demonstrate remote SPP detection using the GaAs MSM detector by means of polarization-dependent measurements. In Fig. 4a we present photocurrent maps normalized with respect to the laser intensity of a MIM–MSM device with an 8-μm separation between the slits for TE and TM polarization. The excitation wavelength is 800 nm. In the case of TE polarization (top panel) we only detect a very small absorption enhancement when the laser spot scans over the SPP injection slit, indicating that no surface plasmon modes or conventional waveguide modes are excited. In the measurement with TM polarization (bottom panel), a huge photoresponse is observed. We attribute this enhanced response to the remote detection of SPPs launched at the injection slit. In order to investigate the decay of the SPP energy along the waveguide, line scans in the middle of the waveguide are presented in Fig. 4b for MIM waveguides with injection–detection distances from 0 to 12 μm ($\lambda = 720$ nm). Owing to the field penetration in the metal parts of the waveguide, ohmic losses in the two metal layers cause the SPP energy to decay exponentially as it propagates along the waveguide, as is clearly observed in the

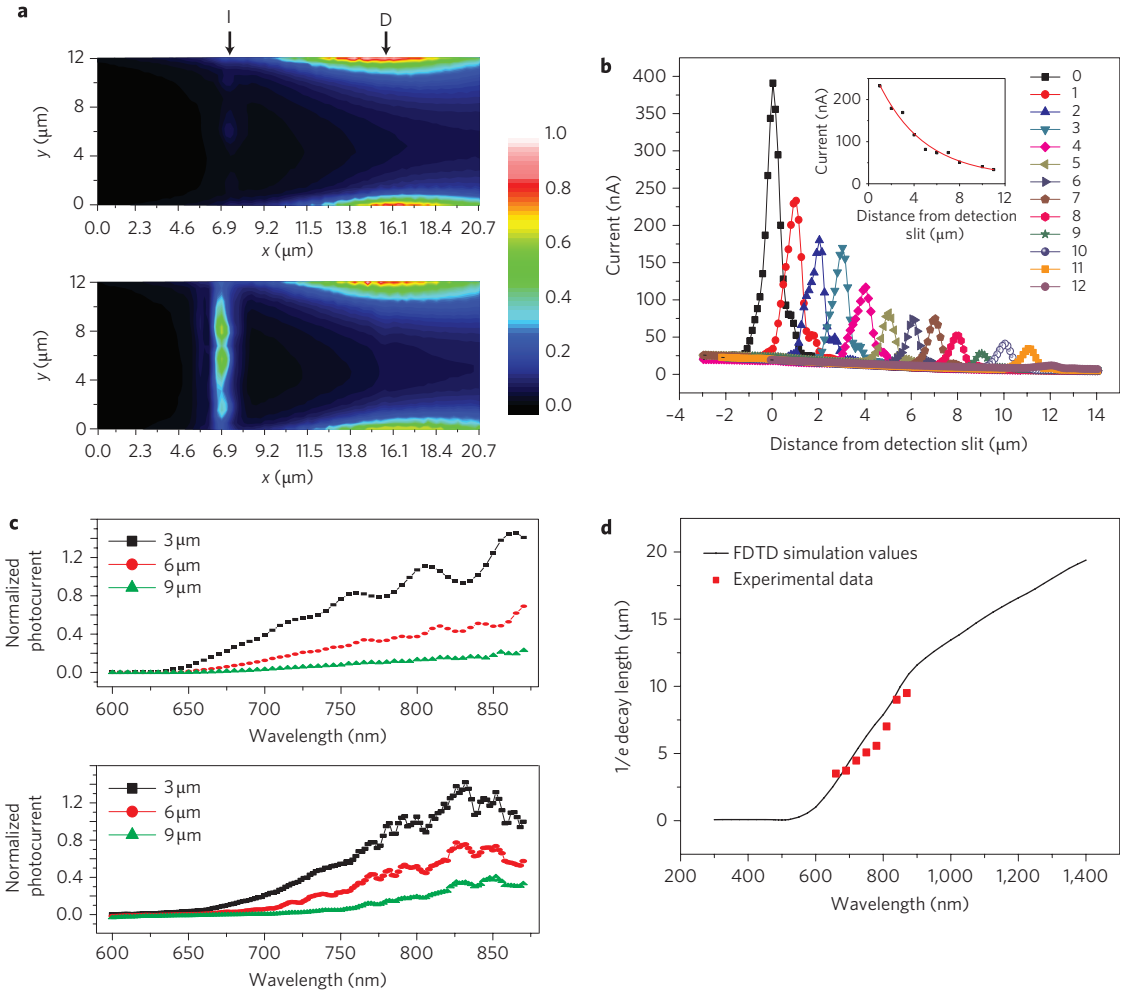

Figure 4 | MSM photocurrent measurements. a, Two-dimensional photocurrent maps for an injection–detection distance of 8 μm. The injection and detection slit are marked by I and D. No current enhancement is measured for TE polarization (top panel), indicating that no SPP excitation takes place. For TM polarization (bottom panel), SPP transmission causes a high photocurrent when the spot scans over the injection slit. **b**, Linescans (TM) over the middle of the waveguide for varying injection–detection distances (in μm). The detection slit is located at $x = 0$. **c**, Spectral responses of the SPP detectors (bottom panel) and the corresponding calculated spectra (top panel). **d**, Comparison between the calculated e^{-1} decay lengths and the experimental values.

measured photocurrent scans. By fitting the photocurrent for injection–detection distances of 1–12 μm, an e^{-1} decay length of 4.7 μm is found for 720 nm, in good agreement with literature values[6,14].

To investigate SPP dispersion in the waveguide, we performed spectral measurements (see Methods). To eliminate wavelength-dependent features of the light source, the monochromator and other optical components, the measured data are divided by the photoresponse of a reference detector containing no SPP features. Also, the background signal (independent of the waveguide length) is subtracted from the data to enable a direct comparison with results obtained through numerical calculations. In Fig. 4c the normalized spectral photoresponse is plotted as a function of the wavelength for the case of TM polarization (bottom panel). A clear injection–detection distance dependency is observed, in line with previously presented experiments. Because of the lower absorption in the metal layers at longer wavelengths, an ascending curve is found as a function of the free-space wavelength. The results correspond very well to the data obtained with numerical calculations presented in the top panel of Fig. 4c, which were performed using the same parameters as in the experiment. The finite size of the exciting laser spot prevents the formation of a pronounced interference caused by partial reflections at both slits. Such interference effects lead to the standing-wave pattern observed in Fig. 2b. The finite spot size explains why, unlike in the two-dimensional simulations, the experimental spectral data do not show pronounced oscillations. By fitting the photocurrent data for different injection–detection distances, e^{-1} decay lengths of 3.5 μm for a free-space wavelength of 660 nm to 9.5 μm for 870 nm were found.

As an independent check, the e^{-1} decay lengths were determined by using the modesolver of Lumerical FDTD (www.lumerical.com). As can be inferred from Fig. 4d, the investigated MIM waveguide supports e^{-1} decay lengths from zero up to tens of micrometres. The experimental data points obtained by electrical SPP detection are plotted together with the simulation curve. A good agreement between the experimental and calculated values is observed. All these results corroborate that an integrated MSM detector provides an efficient way to detect SPPs in metallic slot waveguides and also offers a powerful method of probing its properties. By combining these plasmonic detectors with waveguide-integrated light-emitting diodes[19], metallic-coated nanocavities[20] or nanowire light sources[21], the fabrication of a scalable, high-bandwidth plasmonic circuit on-chip can be realized in the near future.

In conclusion, we have demonstrated the remote electrical detection of SPPs inside a MIM waveguide by means of a nanoscaled MSM detector, showing great potential for the integration of scalable high-bandwidth metallic waveguides in electronic circuits.

Opto-electric transduction was realized by means of resonant coupling of propagating SPPs to a waveguide-integrated GaAs MSM detector. Polarization-dependent and spectral measurements were performed to demonstrate and study the electrical detection of confined SPPs. e^{-1} decay lengths of 3.5 μm for a free-space wavelength of 660 nm to 9.5 μm for 870 nm were found. We firmly believe that the development and fabrication of these new active plasmonic components open unique possibilities for both scientific and application-minded research.

Methods

Fabrication of the waveguide-integrated detectors. The waveguide structures were fabricated on a semi-insulating GaAs wafer. By means of molecular beam epitaxy a 1-μm-thick undoped GaAs layer was grown as the active layer of an MSM photodetector. After removing the native GaAs oxide, the bottom layer of the MIM waveguide was deposited by sputtering (Au/Ti 100 nm/2 nm). A subwavelength gap of 300 nm was defined in the negative HSQ resist by electron-beam lithography. After exposure to 100 W oxygen plasma for 20 min to harden the resist, the pattern was transferred into the gold layer by ion milling. The titanium adhesion layer and the remaining HSQ were removed in HF. The insulating layer of the MIM structure consisted of 90 nm HSQ resist, leading to a SiO_2-like structure when cured for 20 min in 100 W oxygen plasma. HSQ was chosen because of its good planarizing properties for submicrometre structures and for its SiO_2-like optical properties[22]. The top metal layer of the waveguide was also sputter deposited (Au/Ti 160 nm/2 nm). To fabricate the injection slit, similar electron-beam and ion milling steps were performed as for the detection slit. In the last step the planarization layer was selectively etched on top of the contacts using an optical lithography step so as to access the contact paths by wire bonding or probe needles.

Spectral response setup. The light from a supercontinuum white light source was coupled into a monochromator to select the desired wavelength. The light was linearly polarized and focused by a 100 × /0.7 NA Apochromatic long working distance objective onto the sample. Electrical connections were made by wirebonding or probe needles. Electrical readout of the devices was performed with a Keithley 2400 sourcemeter. An *xy*-piezo scanner mounted on an *xyz*-stage allowed one- and two-dimensional scans to be performed. At every selected position the current was measured. By scanning the sample in the focal plane a one- or two-dimensional map of the photocurrent of the detector was obtained. In the two-dimensional photocurrent maps presented in Fig. 4a, the *x*-axis contains 90 steps of 0.23 μm and the *y*-axis 70 steps of 0.46 μm. The spectral response of the MSM detector in Fig. 4c was obtained by focusing the laser spot on the injection slit and performing a wavelength sweep.

Numerical calculations. For the numerical calculations presented in Fig. 2, the RF module of Comsol Multiphysics was used. By defining similar boundary conditions to those defined in ref. 23, metals could be extended through the boundaries without introducing any parasitical reflections, allowing us to simulate waveguides with infinite length. For the simulation in Fig. 4d the mode solver of Lumerical FDTD was used.

Received 10 December 2008; accepted 16 March 2009; published online 19 April 2009

References

1. Conway, J. A., Sahni, S. & Szkopek, T. Plasmonic interconnects versus conventional interconnects: a comparison of latency, crosstalk and energy costs. *Opt. Express* **15,** 4474–4484 (2007).
2. Maier, S. A. Waveguiding: The best of both worlds. *Nature Photon.* **2,** 460–461 (2008).
3. Zia, R., Schuller J. A., Chandran, A. & Brongersma, M. L. Plasmonics: the next chip-scale technology. *Mater. Today* **9,** 20–27 (2006).
4. Ju, J. J. *et al.* 40 Gbit/s light signal transmission in long-range surface plasmon waveguides. *Appl. Phys. Lett.* **91,** 171117 (2007).
5. Berini, P., Charbonneau, R., Lahoud, N. & Mattiussi, G. Characterization of long-range surface-plasmon-polariton waveguides. *J. Appl. Phys.* **98,** 043109 (2005).
6. Dionne, J. A., Lezec, H. J. & Atwater, H. A. Highly confined photon transport in subwavelength metallic slot waveguides. *Nano Lett.* **6,** 1928–1932 (2006).
7. Chen, L., Shakya, J. & Lipson, M. Subwavelength confinement in an integrated metal slot waveguide on silicon. *Opt. Lett.* **31,** 2133–2135 (2006).
8. Weeber, J., Lacroute, Y. & Dereux, A. Optical near-field distributions of surface plasmon waveguide modes. *Phys. Rev. B* **68,** 115401 (2003).
9. Verhagen, E., Dionne, J. A., Kuipers, L., Atwater, H. A. & Polman, A. Near-field visualization of strongly confined surface plasmon polaritons in metal–insulator–metal waveguides. *Nano Lett.* **8,** 2925–2929 (2008).
10. De Vlaminck, I., Van Dorpe, P., Lagae, L. & Borghs, G. Local electrical detection of single nanoparticle plasmon resonance. *Nano Lett.* **7,** 703–706 (2007).
11. Ishi, T., Fujikata, J., Makita, K., Baba, T. & Ohashi, K. Si nano-photodiode with a surface plasmon antenna. *Jpn Appl. Phys.* **44,** L364–L366 (2005).
12. Collin, S., Pardo, F. & Pelouard, J. Resonant-cavity-enhanced subwavelength metal–semiconductor–metal photodetector. *Appl. Phys. Lett.* **83,** 1521–1523 (2003).
13. Kusunoki, F., Yotsuya, T., Takahara, J. & Kobayashi, T. Propagation properties of guided waves in index-guided two dimensional optical waveguides. *Appl. Phys. Lett.* **86,** 211101 (2005).
14. Dionne, J. A., Sweatlock, L. A., Atwater, H. A. & Polman, A. Plasmon slot waveguides: towards chip-scale propagation with subwavelength-scale localization. *Phys. Rev. B* **73,** 035407 (2006).
15. Burm, J. *et al.* High-frequency, high-efficiency MSM photodetectors. *IEEE J. Quantum Electron.* **31,** 1504–1509 (1995).
16. Kordos, P., Forster, A., Marso, M. & Ruders, F. 550 GHz bandwidth photodetector on low temperature grown molecular-beam epitaxial GaAs. *IEEE Electron. Lett.* **34,** 119–120 (1998).
17. Chou, S. Y., Liu, Y. & Fischer, P. B. Terahertz GaAs metal–semiconductor–metal photodetectors with 25 nm finger spacing and finger width. *Appl. Phys. Lett.* **61,** 477–479 (1992).
18. Chou, S. Y., Liu, Y., Khalil, W., Hsiang, T. Y. & Alexandrou, S. Ultrafast nanoscale metal–semiconductor–metal photodetectors on bulk and low-temperature grown GaAs. *Appl. Phys. Lett.* **61,** 819–821 (1992).
19. Koller, D. M. *et al.* Organic plasmon-emitting diode. *Nature Photon.* **2,** 684–687 (2008).
20. Hill, M. T. *et al.* Lasing in metallic-coated nanocavities. *Nature Photon.* **1,** 589–594 (2007).
21. Park, H. *et al.* A wavelength-selective photonic-crystal waveguide coupled to a nanowire light source. *Nature Photon.* **2,** 622–626 (2008).
22. Singh, S. K., Kumbhar, A. A. & Dusane, R. O. Repairing plasma-damaged low-*k* HSQ films with trimethylchlorosilane treatment. *Mater. Sci. Eng. B* **127,** 29–33 (2006).
23. Yu, C. & Chang, H. Yee-mesh-based finite difference eigenmode solver with PML absorbing boundary conditions for optical waveguides and photonic crystal fibers. *Opt. Express* **12,** 6165–6177 (2004).

Acknowledgements

The authors thank J. Moonens for electron-beam exposures, E. Vandenplas and J. Feyaerts for technical support and W. van de Graaf for molecular beam epitaxy growth. P.V.D. thanks the Fonds Wetenschappelijk Onderzoek Vlaanderen (FWO)-Flanders for financial support.

Additional information

Reprints and permission information is available online at http://npg.nature.com/reprintsandpermissions/. Correspondence and requests for materials should be addressed to P.N.

nature photonics

LETTERS

PUBLISHED ONLINE: 19 APRIL 2009 | DOI: 10.1038/NPHOTON.2009.46

Controlling the near-field oscillations of loaded plasmonic nanoantennas

M. Schnell[1], A. García-Etxarri[2], A. J. Huber[1,3], K. Crozier[4], J. Aizpurua[2] and R. Hillenbrand[1,3]*

Optical and infrared antennas[1–6] enable a variety of cutting-edge applications ranging from nanoscale photodetectors[7] to highly sensitive biosensors[8]. All these applications critically rely on the optical near-field interaction between the antenna and its 'load' (biomolecules or semiconductors). However, it is largely unexplored how antenna loading affects the near-field response. Here, we use scattering-type near-field microscopy to monitor the evolution of the near-field oscillations of infrared gap antennas progressively loaded with metallic bridges of varying size. Our results provide direct experimental evidence that the local near-field amplitude and phase can be controlled by antenna loading, in excellent agreement with numerical calculations. By modelling the antenna loads as nanocapacitors and nanoinductors[9–11], we show that the change of near-field patterns induced by the load can be understood within the framework of circuit theory. Targeted antenna loading provides an excellent means of engineering complex antenna configurations in coherent control applications[12], adaptive nano-optics[13] and metamaterials[14].

Optical and infrared antennas based on metal nanostructures allow for efficient conversion of propagating light into nanoscale confined and strongly enhanced optical fields, and vice versa[1–5,15]. Antennas consisting of adjacent metallic segments (that is, nanorods) separated by a nanoscopic gap (gap antennas)[1,3,4,7,8,16,17] are particularly efficient. The near-field coupling across the gap can generate extremely strong and localized fields, which are essential for applications such as single-molecule surface-enhanced Raman spectroscopy (SERS)[8] or extreme-ultraviolet (EUV) generation[16]. However, the antenna response is very sensitive to small environmental changes at the gap[18–20]. Thus, the presence of molecules or semiconductors in the gap (as is usually the case in spectroscopy or detector applications) can dramatically affect the antenna's far-field optical response with the possibility of degrading the antenna performance. On the other hand, we can take advantage of this effect for versatile tuning of the antenna response. Recently, Alù and Engheta[9,10] described this possibility in terms of antenna loading, a concept adapted from radio-frequency (RF) technology. Following the RF design rules, it has been theoretically demonstrated that the scattering response and resonance frequency of optical antennas can be tuned by loading the antenna gap with either metals or dielectrics acting as inductors or capacitors, respectively. In this Letter, we present an experimental study of how loading of antenna gaps affects the near-field response using scattering-type scanning near-field optical microscopy (s-SNOM)[21]. We provide direct experimental evidence that the local near-field amplitude and phase response can be controlled by antenna loading.

Our experiments were performed with antennas based on gold nanorods designed for fundamental dipolar resonance at mid-infrared frequencies. The rods ($1{,}550 \times 230 \times 60$ nm) were fabricated on a silicon substrate by electron-beam lithography and show a far-field resonance at a wavelength of $\lambda = 9.6$ μm (ref. 2). Note that the antenna length is significantly shorter than $\lambda/2$ due to dielectric screening by the substrate, the large width of the antenna compared to its length and plasmonic effects[15,22]. To study how the progressive loading of an antenna gap affects the near-field distribution, we used focused ion beam (FIB) milling to prepare gaps of different shapes and sizes at the centre of the rods. Using a transmission-mode s-SNOM[21,23] operating at a wavelength of $\lambda = 9.6$ μm (Fig. 1), near-field amplitude and phase images of the rods were recorded.

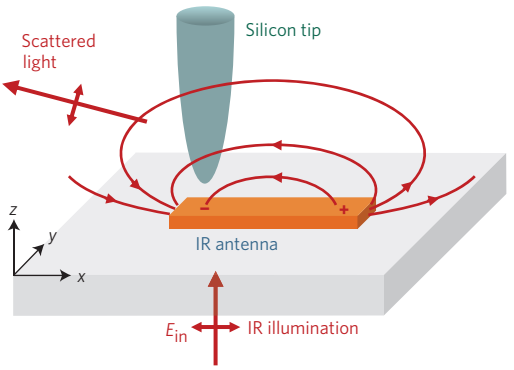

Figure 1 | Mapping the near-field distribution of optical antennas with a transmission-mode s-SNOM. The antenna is illuminated from below through a transparent substrate. While scanning the sample, the near fields of the antenna are scattered by the tip and recorded interferometrically, yielding infrared amplitude and phase images simultaneously to topography.

In a first experiment with well established dipole antennas[2] we demonstrated that transmission-mode s-SNOM equipped with dielectric tips allows for reliable mapping of antenna near-field modes. Figure 2a shows the infrared near-field amplitude and phase images of a continuous (unmodified) nanorod. The images reveal strong-amplitude signals at the rod extremities and a phase jump of about 180° at the rod centre, providing direct experimental evidence of an anti-phase field oscillation as expected for the dipolar near-field mode. To analyse the image contrast, we performed numerical calculations of the x- and z-components of the near-field distribution of a 1,550-nm-long nanorod in resonance at a wavelength of 9.6 μm (see Supplementary Fig. S1). Comparison with the experimental data clearly shows that the amplitude and phase of the z-component, $|E_z|$ and φ_z, are probed[24] (Fig. 2a, bottom).

In Fig. 2d we study a nanorod that was fully cut in its centre, representing an unloaded gap antenna. The topography image clearly reveals the two closely spaced segments separated by a

[1]Nanooptics Laboratory, CIC nanoGUNE, 20018 Donostia – San Sebastián, Spain, [2]Centro de Física de Materiales (CSIC-UPV/EHU) and Donostia International Physics Center (DIPC), 20018 Donostia – San Sebastián, Spain, [3]Nano-Photonics Group, Max-Planck-Institut für Biochemie, 82152 Martinsried and Center for NanoScience (CeNS), Munich, Germany, [4]Harvard University, Cambridge, Massachusetts 02138, USA. *e-mail: r.hillenbrand@nanogune.eu

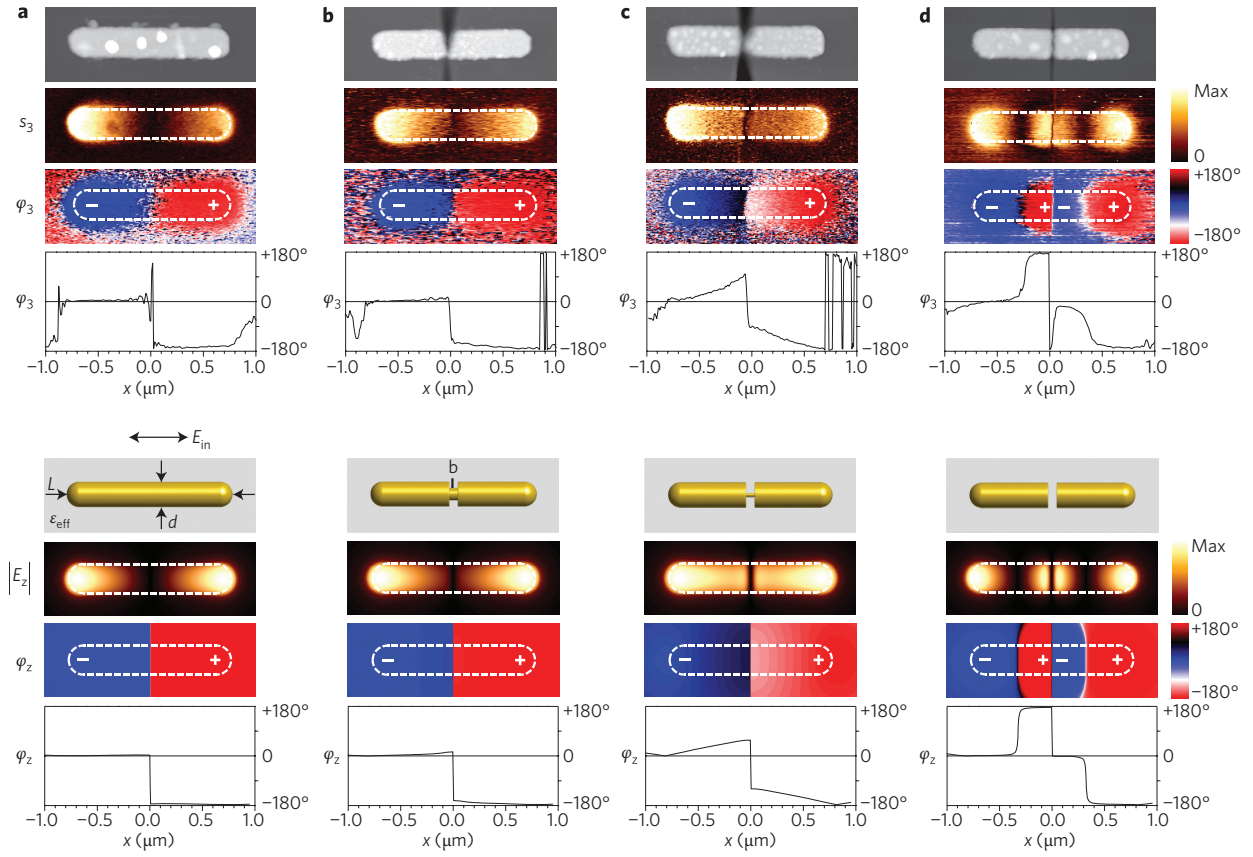

Figure 2 | Near-field images of progressively loaded nanoantennas at a wavelength of $\lambda = 9.6$ μm. a, Continuous rod antenna. **b**, Low-impedance loaded antenna where a thick metal bridge connects the two antenna segments. **c**, High-impedance loaded antenna where a tiny metal bridge connects the two antenna segments. **d**, Fully cut antenna where the two antenna segments are completely separated. Top: Experimental results showing topography and near-field amplitude s_3 and phase φ_3 images. Bottom: Theoretical near-field distribution of a model system, a 1,550-nm-long gold rod with diameter $d = 230$ nm and an 80-nm gap in its centre, embedded in an effective medium of dielectric value $\varepsilon_{eff} = 6.34$. The gap is bridged by gold disks of 80 nm length with diameters $b = 230$ nm (**a**), $b = 80$ nm (**b**), $b = 40$ nm (amplitude image, **c**) and $b = 30$ nm (phase image, **c**), $b = 0$ nm (**d**). The near-field images show the z-component of the electric field in amplitude E_z and phase φ_z in a height of 50 nm above the rod surface. In all phase images, the phase is set to 0° at the left antenna extremity.

central gap of about 80 nm. The near-field images show that both antenna segments oscillate in a dipolar-like mode, featuring high-amplitude signals at the antenna extremities and near the gap, as well as a phase jump of 180° near the centre of each segment and inside the gap. This is in good agreement with numerical calculations assuming an 80-nm gap in the rod centre (Fig. 2d, bottom).

The near-field patterns of the gap antennas are completely changed when a metal bridge (representing the load) connects the two antenna segments (Fig. 2b). Near the gap, in contrast to the fully cut rod (Fig. 2d), no significant near fields are observed. The topography clearly reveals the deep, wedge-like cut through the rod centre and also shows the metal bridge at the lower rim of the rod. Obviously, the small metal bridge (about 10% of the total cross-section of the nanorod, estimated from the topography) suffices to restore the fundamental dipolar near-field mode of the continuous rod (Fig. 2a). We attribute this effect to a current flow through the bridge that prevents charge pile-up at the gap.

A highly interesting near-field distribution is observed in Fig. 2c where a much thinner metal bridge connects the nanorod segments. The bridge cross-section is estimated from the topography to be about 2% of the total rod cross-section, thus being significantly reduced compared to Fig. 2b. The near-field images show striking differences to both the continuous and fully cut rods. We observe a significant amplitude signal along the total length of each segment and a considerable phase gradient of about 80°. To further illustrate this interesting behaviour, we monitored the near-field oscillations of the antennas in space and time. Owing to the simultaneous acquisition of amplitude $s_3(x, y)$ and phase $\varphi_3(x, y)$ signals, we can represent the near field at a sample position (x, y) and at time t by

$$f(x, y, t) = \mathrm{Re}[s_3(x, y)e^{i\varphi_3(x,y)-i2\pi t/T}] \quad (1)$$

where T is the oscillation period. A series of snapshots of f for all four antennas investigated in this Letter is shown in Fig. 3. For the continuous rod (Fig. 3a, obtained from data in Fig. 2a) the snapshots clearly show the time evolution of a single dipolar oscillation, whereas the result for the fully cut rod (Fig. 3d) reveals two closely spaced dipolar-like modes evolving simultaneously in time. In the case where the tiny metal bridge connects the antenna segments (Fig. 3c), however, we observe a significant time delay between the near fields at the gap and the antenna extremities.

To analyse the near-field behaviour of the metal-loaded antennas (Fig. 2b,c), we calculate the z-component of the near-field amplitude $|E_z|$ and phase φ_z, assuming an 80-nm gap in between the antenna segments, loaded with 80-nm-long cylindrical gold bridges of diameters between $b = 0$ nm and $b = 230$ nm. The results (see Supplementary Fig. S2) reveal that by progressive antenna loading (increasing bridge diameter b) the near-field pattern of the fully

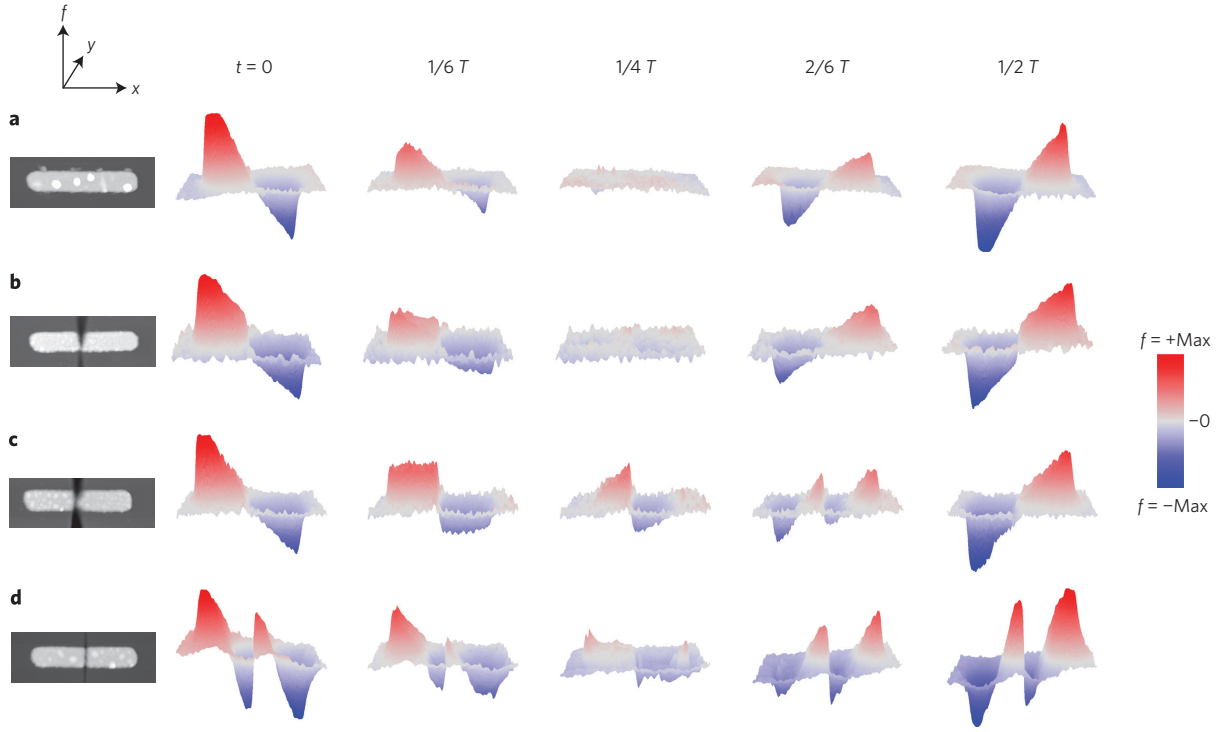

Figure 3 | Time evolution of the antenna's near-field distribution *f* obtained from the experimental data of Fig. 2. a, Continuous rod antenna. **b**, Low-impedance (inductive) loaded antenna (thick metal bridge). **c**, High-impedance (inductive) loaded antenna (tiny metal bridge). **d**, Fully cut antenna. *T* denotes the oscillation period. The corresponding movie of the near-field oscillations is provided in the Supplementary Information.

cut rod ($b = 0$) evolves towards the fundamental dipolar mode of the continuous rod. Comparing experiment and theory, we can assign to each s-SNOM image a calculated near-field pattern. For the antenna in Fig. 2b we obtain good agreement for a bridge diameter $b = 80$ nm, which corresponds to 12% of the rod's cross-section. This is consistent with the bridge size estimated from the topography image. The s-SNOM images in Fig. 2c match well with calculated near-field patterns for b between 30 to 40 nm (~2% of the rod cross-sectional area), thus confirming that indeed a tiny metallic bridge is connecting the two segments in our experiment. It is interesting to note that the variation of the single parameter b is sufficient to reproduce all the experimentally observed near-field patterns (Fig. 2a–d).

To provide further theoretical insights, we calculated the extinction spectra of the gap antennas for bridge diameters between 0 and 100 nm; these are summarized in the contour plot of Fig. 4a. For large bridge diameter b, we observe a first-order dipolar mode (D1) of the antenna at around $\lambda \approx 10$ μm (according to the experimental and theoretical near-field distributions shown in Fig. 2b) and a weaker second-order dipolar mode (D2) at $\lambda = 3.5$ μm. With decreasing bridge diameter b, we observe a slight redshift of both modes. Reaching small bridge diameters $b < 50$ nm, the behaviour changes significantly. The first-order mode (D1) experiences a divergent redshift at $b \approx 20$ nm while being increasingly damped. This can be explained by the restriction of the charge flow across the gap that is necessary to build up a mode structure compatible with D1. Thus, in the limit of very small bridge diameters, the first-order mode (D1) cannot be excited anymore. The second-order mode (D2), in contrast, is enhanced with decreasing b and turns into the first-order mode of the coupled nanorods (C1), owing to the compatible structure of both modes. Considering now the antenna response at the fixed wavelength $\lambda = 9.6$ μm, we clearly observe a transition from the first-order dipolar mode (D1) of a continuous rod (large b) towards the mode of the coupled nanorods (C1) when b is decreasing. At a given bridge diameter of ~30 nm (corresponding to our experimental situation where a tiny bridge connects the antenna gap, Fig. 2c) the antenna response at a wavelength of $\lambda = 9.6$ μm lies in between the two branches coming from D1 and D2. Thus, the near-field distribution of the antenna comprises contributions of both branches, yielding the strong phase shift on each antenna segment, an effect that we clearly identify in both the experimental and calculated near-field images.

In the RF range, circuit theory is an essential tool for the efficient design of antenna devices. Adopting RF concepts, we now show how the behaviour of our loaded infrared antennas can be explained within the framework of optical circuit theory, which has recently been introduced by Engheta and colleagues[9–11]. We can describe the impedance of the antenna load Z_{load} as a parallel circuit composed of the inductive impedance of the metallic bridge Z_{bridge} and the capacitive impedance of the effective medium filling the gap Z_{gap}, given by

$$Z_{\mathrm{bridge}} = \frac{ig}{\omega\varepsilon_{\mathrm{Au}}\pi\left(\frac{b}{2}\right)^2}, \quad Z_{\mathrm{gap}} = \frac{ig}{\omega\varepsilon_{\mathrm{eff}}\pi\left[\left(\frac{d}{2}\right)^2 - \left(\frac{b}{2}\right)^2\right]} \qquad (2)$$

Here, g is the gap width (80 nm), ω the infrared frequency, $\varepsilon_{\mathrm{Au}}$ the dielectric value of gold and $\varepsilon_{\mathrm{eff}}$ the dielectric value of the effective medium filling the gap of our model antennas considered in Figs 2 and 4a. In Fig. 4b we display a contour plot that shows the value of the load reactance X_{load} (given by $Z_{\mathrm{load}} = R_{\mathrm{load}} - iX_{\mathrm{load}}$) as a function of bridge diameter b and wavelength λ, highlighting regions of inductive (blue) and capacitive (red) behaviour. Comparing the evolution of the antenna modes (Fig. 4a) with the behaviour of X_{load} (Fig. 4b), we find an interesting connection: the first-order mode D1 strongly shifts to longer wavelengths when X_{load} increases (more inductive, displayed in darker blue). The region of capacitive X_{load},

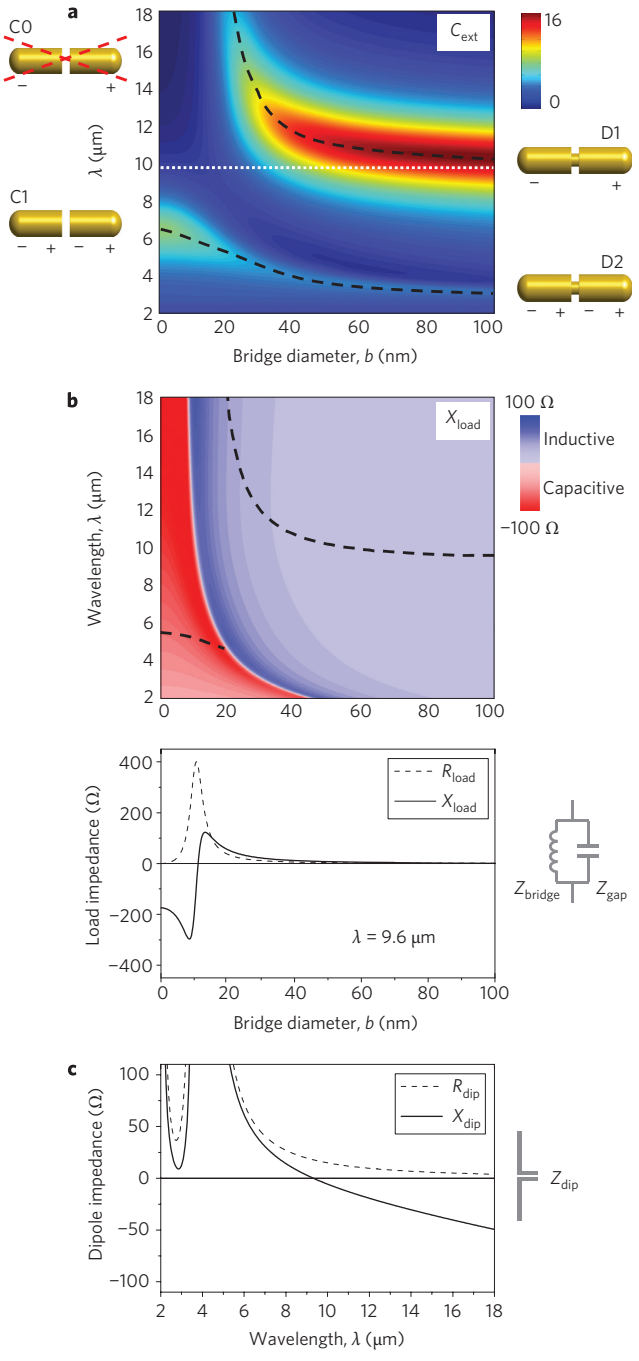

Figure 4 | Comparison of numerical calculations and antenna theory. **a**, Extinction cross-section calculated for the antennas considered in Fig. 2 as a function of the bridge diameter *b*, normalized to the projected area of the antenna. The dashed black lines trace the extinction resonances. The first-order and second-order modes of the continuous rod are marked by D1 and D2, respectively. For antennas with $b = 0$ (isolating gap), C1 is the first-order mode. The zero-order mode C0 is unphysical because it would have finite charge on each antenna segment[22]. **b**, Top: Contour plot displaying the load reactance X_{load} as a function of *b* and wavelength λ. Regions of capacitive reactance (negative X_{load}) are shown in red, regions of inductive reactance (positive X_{load}) in blue. The black dashed lines trace the first-order antenna resonances calculated by means of circuit theory. Bottom: Load resistance R_{load} and load reactance X_{load} displayed as a function of *b*, calculated for $\lambda = 9.6$ μm. **c**, Intrinsic resistance R_{dip} and reactance X_{dip} of a cylindrical dipole antenna as a function of wavelength. The calculation is based on standard equations of antenna theory[30] and assumes a 1,550-nm-long antenna of 230-nm diameter embedded in an effective medium with $\varepsilon_{eff} = 6.34$.

however, does not support the D1 mode. The intensity of the D2 mode in contrast strongly increases when the load becomes mainly capacitive. We can describe the load-induced spectral shifts of the antenna modes by modelling our infrared dipole antennas as a series combination of the dipole intrinsic impedance $Z_{dip} = R_{dip} - iX_{dip}$ (Fig. 4c) and the load impedance Z_{load} (refs 9,10). In this equivalent circuit, the antenna resonance occurs when the load reactance cancels the dipole intrinsic reactance, $X_{load} = -X_{dip}$. Evaluating this condition, we obtain the resonance wavelength as a function of bridge size *b*. The result is shown in Fig. 4b by dashed lines. For large *b*, the circuit resonance appears at a wavelength of ~9.3 μm, which is in good agreement with the resonance wavelength obtained from the extinction spectrum (Fig. 4a). With decreasing *b*, still in the inductive region, we find that the circuit resonance is redshifted owing to an increase of the load reactance X_{load} (darker blue). Below the critical bridge size b_c—which we define as the turning point where the load changes from inductive to capacitive nature—the circuit resonance suffers an abrupt change, shifting to shorter wavelengths owing to the change of sign of X_{load}, and correspondingly of X_{dip}. Comparing the evolution of the circuit resonances (dashed lines in Fig. 4b) with the spectral behaviour of the antenna modes (dashed lines in Fig. 4a), we find a remarkable agreement considering the simplicity of the model based on classical antenna theory. We expect an even better agreement by taking into account plasmonic effects[15] that are already present at infrared frequencies[6,25].

Finally, we address how the role of the load impedance affects the near-field distribution of the antennas. At $\lambda = 9.6$ μm the dipole intrinsic impedance amounts to $Z_{dip} = (17 + 2i)\ \Omega$ (Fig. 4c). For large bridge diameters ($b > 80$ nm) we find that the load impedance Z_{load} is considerably smaller than Z_{dip}, thus facilitating current flow through the load. Consequently, accumulation of charges at the gap is very low, yielding negligible near fields in its vicinity (Fig. 2b). Below the critical bridge size b_c, the load impedance is of capacitive nature. Therefore, charges are piled up at the gap, which generate strong near fields, as observed both in experiment and calculations (Fig. 2d). Interestingly, the deviation of the near-field patterns from dipolar-like modes (Fig. 2c) occurs close to the critical bridge size (see also Supplementary Fig. S2), thus confirming that the change of the near-field distribution is a consequence of the transition from inductive to capacitive load impedance.

In conclusion, the near-field images of gap antennas presented here provide direct experimental evidence that the local near-field amplitude and phase distribution can be controlled by antenna loading. This opens the door for designing near-field patterns without the need to change antenna length, which could be highly valuable for the development of compact and integrated nanophotonic devices.

Methods

Near-field microscopy. Our s-SNOM[21,23] is based on an atomic force microscope (AFM) in which cantilevered tips locally scatter the near fields of the antennas (Fig. 1). Recent s-SNOM studies[24,26–28] of plasmon-resonant nanostructures have shown that dielectric tips and appropriate polarization schemes reduce the tip–sample near-field interaction, allowing for faithful mapping of plasmonic near-field modes. In our setup we thus use silicon tips and illuminate the sample from below (transmission-mode). Owing to weak focusing, the laser beam is polarized parallel to the sample surface with only a negligible component along the tip axis. We thus achieve efficient excitation of the antennas and avoid direct excitation of the tip. Furthermore, the transmission mode offers the advantage of homogeneous antenna illumination, thus avoiding phase-retardation effects[27] inherent to the backscattering geometry in typical s-SNOM experiments.

Imaging of the antennas was performed with a CO_2 laser operating at $\lambda = 9.6$ μm. The polarization of the incident field was adjusted to be parallel to the antenna axis and the polarization of the reference beam was chosen parallel to the tip axis (*z*-axis). The tip-scattered light was collected with a parabolic mirror and recorded simultaneously with topography. Background contributions were suppressed by vertical tip oscillation at frequency Ω and by subsequent higher-harmonic demodulation of the detector signal at $n\Omega$ with $n \geq 2$ (refs 21,24,26,27). In combination with pseudoheterodyne interferometric detection, near-field optical amplitude s_n and phase φ_n images were obtained[23].

Because of the weak scattering efficiency of the silicon tips, we needed to operate with tapping amplitudes of ~200 nm. For such large tapping amplitudes, background contributions were not fully suppressed, even with signal demodulation at $n = 3$. Nevertheless, background-free near-field images could be obtained by complex-valued subtraction of the background contribution because (i) s-SNOM signals obtained by pseudoheterodyne interferometric detection are a linear complex-valued sum of near-field and background contributions[23], and (ii) the background in the presented experiments was found to be constant in the x–y plane.

Numerical calculations. The near-field distribution (Fig. 2) and the extinction cross-section (Fig. 4a) of the antennas were calculated numerically with the boundary element method (BEM)[29]. Note that in the experiment the antenna consisted of flat sections of gold on a silicon substrate, with air above the substrate, whereas the calculations were based on cylindrical rods situated in an effective medium. The dielectric value of the effective medium was chosen such that the resonance of the continuous rod ($b = 230$ nm) matched the experimental resonance measured for the 1,550-nm-long gold nanorod on the silicon substrate[2]. Owing to the presence of the silicon substrate (the effective medium surrounding the antennas in the numerical calculations), the resonance is strongly redshifted when compared to nanorods situated in air[22].

The near-field distributions were calculated for a height of 50 nm above the antenna surface. This value was chosen in order to obtain best agreement between the experimental and numerical near-field patterns for the continuous and the fully cut rods (Fig. 2a,d). Note that in the experiments the bridge dimensions can only be estimated from the topography images. Further, the calculations do not take into account the V-shape of the gap. Both aspects could explain the differences between the theoretical and experimental bridge size for a given near-field pattern. Also, this might be the reason why we find the best agreement for amplitude and phase images for slightly different bridge diameters.

Received 11 November 2008; accepted 11 March 2009; published online 19 April 2009

References

1. Grober, R.-D., Schoellkopf, R.-J. & Prober, D.-E. Optical antenna: Towards a unity efficient near-field optical probe. *Appl. Phys. Lett.* **70,** 1354–1356 (1997).
2. Crozier, K. B., Sundaramurthy, A., Kino, G. S. & Quate, C. F. Optical antennas: Resonators for local field enhancement. *J. Appl. Phys.* **94,** 4632–4642 (2003).
3. Mühlschlegel, P., Eisler, H.-J., Martin, O. J. F., Hecht, B. & Pohl, D. W. Resonant optical antennas. *Science* **308,** 1607–1609 (2005).
4. Schuck, P. J., Fromm, D. P., Sundaramurthy, A., Kino, G. S. & Moerner, W. E. Improving the mismatch between light and nanoscale objects with gold bowtie nanoantennas. *Phys. Rev. Lett.* **94,** 017402 (2005).
5. Taminiau, T. H., Stefani, F. D., Segerink, F. B. & Van Hulst, N. F. Optical antennas direct single-molecule emission. *Nature Photon.* **2,** 234–237 (2008).
6. Neubrech, F. *et al.* Resonant plasmonic and vibrational coupling in a tailored nanoantenna for infrared detection. *Phys. Rev. Lett.* **101,** 157403 (2008).
7. Tang, L. *et al.* Nanometre-scale germanium photodetector enhanced by a near-infrared dipole antenna. *Nature Photon.* **2,** 226–229 (2008).
8. Xu, H., Bjerneld, E. J., Käll, M. & Börjesson, L. Spectroscopy of single hemoglobin molecules by surface enhanced raman scattering. *Phys. Rev. Lett.* **83,** 4357–4360 (1999).
9. Alu, A. & Engheta, N. Input impedance, nanocircuit loading and radiation tuning of optical nanoantennas. *Phys. Rev. Lett.* **101,** 043901 (2008).
10. Alu, A. & Engheta, N. Tuning the scattering response of optical nanoantennas with nanocircuit loads. *Nature Photon.* **2,** 307–310 (2008).
11. Engheta, N., Salandrino, A. & Alu, A. Circuit elements at optical frequencies: Nanoinductors, nanocapacitors and nanoresistors. *Phys. Rev. Lett.* **95,** 095504 (2005).
12. Stockmann, M. I., Faleev, S. V. & Bergmann, D. J. Coherent control of femtosecond energy localization in nanosystems. *Phys. Rev. Lett.* **88,** 67402 (2002).
13. Aeschlimann, M. *et al.* Adaptive subwavelength control of nano-optical fields. *Nature* **446,** 301–304 (2007).
14. Shalaev, V. M. Optical negative-index metamaterials. *Nature Photon.* **1,** 41–48 (2007).
15. Novotny, L. Effective wavelength scaling for optical antennas. *Phys. Rev. Lett.* **98,** 266802 (2007).
16. Kim, S. *et al.* High-harmonic generation by resonant plasmon field enhancement. *Nature* **453,** 757–760 (2008).
17. Ghenuche, P., Cherukulappurath, S., Taminiau, T. H., Van Hulst, N. F. & Quidant, R. Spectroscopic mode mapping of resonant plasmon nanoantennas. *Phys. Rev. Lett.* **101,** 116805 (2008).
18. Atay, T., Song, J. H. & Nurmikko, A. V. Strongly interacting plasmon nanoparticle pairs: From dipole–dipole interaction to conductively coupled regime. *Nano Lett.* **4,** 1627–1631 (2004).
19. Romero, I., Aizpurua, J., Bryant, G. W. & de Abajo, F. J. G. Plasmons in nearly touching metallic nanoparticles: singular response in the limit of touching dimers. *Opt. Express* **14,** 9988–9999 (2006).
20. Lassiter, J. B. *et al.* Close encounters between two nanoshells. *Nano Lett.* **8,** 1212–1218 (2008).
21. Keilmann, F. & Hillenbrand, R. Near-field optical microscopy by elastic light scattering from a tip. *Philos. Trans. R. Soc. London, Ser. A* **362,** 787–805 (2004).
22. Aizpurua, J. *et al.* Optical properties of coupled metallic nanorods for field-enhanced spectroscopy. *Phys. Rev. B* **71,** 235420 (2005).
23. Ocelic, N., Huber, A. & Hillenbrand, R. Pseudoheterodyne detection for background-free near-field spectroscopy. *Appl. Phys. Lett.* **89,** 101124 (2006).
24. Olmon, R. L., Krenz, P. M., Jones, A. C., Boreman, G. D. & Raschke, M. B. Near-field imaging of optical antenna modes in the mid-infrared. *Opt. Express* **16,** 20295–20305 (2008).
25. Fumeaux, C. *et al.* Measurement of the resonant lengths of infrared dipole antennas. *Infrared Phys. & Technol.* **41,** 271–281 (2000).
26. Hillenbrand, R., Keilmann, F., Hanarp, P., Sutherland, D. S. & Aizpurua, J. Coherent imaging of nanoscale plasmon patterns with a carbon nanotube optical probe. *Appl. Phys. Lett.* **83,** 368–370 (2003).
27. Esteban, R. *et al.* Direct near-field optical imaging of higher order plasmonic resonances. *Nano Lett.* **8,** 3155–3159 (2008).
28. Yu, N. *et al.* Plasmonic quantum cascade laser antenna. *Appl. Phys. Lett.* **91,** 173113 (2007).
29. Garcia de Abajo, F. J. & Howie, A. Relativistic electron energy loss and electron-induced photon emission in inhomogeneous dielectrics. *Phys. Rev. Lett.* **80,** 5180–5183 (1998).
30. Balanis, C. A. *Antenna Theory* (John Wiley & Sons, 2005).

Acknowledgements

The authors would like to thank A. Ziegler and A. Rigort (both Abteilung Molekulare Strukturbiologie, Max-Planck-Institut für Biochemie) for help with FIB milling and M. Raschke (Seattle) and N. Engheta (University of Pennsylvania) for stimulating discussions. We thank Nanosensors (Erlangen) for providing HF-etched silicon tips, F.J. García de Abajo for BEM tools and C.F. Quate and G.S. Kino (both Stanford University) for previous insights on the optical antennas studied in this Letter. This research was supported by the Etortek program of the Department of Industry of the Basque Government and the Basque Foundation for Science (Ikerbasque). J.A. acknowledges CSIC special intramural project PIE 2008601039.

Additional information

Supplementary information accompanies this paper at www.nature.com/naturephotonics. Reprints and permission information is available online at http://npg.nature.com/reprintsandpermissions/. Correspondence and requests for materials should be addressed to R.H.

nature photonics

ARTICLES

PUBLISHED ONLINE: 26 APRIL 2009 | DOI: 10.1038/NPHOTON.2009.68

Electrofluidic displays using Young–Laplace transposition of brilliant pigment dispersions

J. Heikenfeld[1]*, K. Zhou[1], E. Kreit[1], B. Raj[1], S. Yang[1], B. Sun[2], A. Milarcik[2], L. Clapp[2] and R. Schwartz[2]

Conventional electrowetting displays reconfigure the contact angle of a coloured oil film on a planar hydrophobic surface. We report on electrofluidic displays, in particular a three-dimensional microfluidic display device that provides a direct view of brilliantly coloured pigment dispersions. Electromechanical pressure is used to pull the aqueous dispersion from a reservoir of small viewable area (<10%) into a surface channel of large viewable area (>90%). The hydrophobic channel and reservoir respectively impart a small or large radius of curvature on the dispersion. Therefore, with no voltage, Young–Laplace pressure forces the dispersion to retract into the reservoir. Preliminary prototypes exhibit ∼55% white reflectance, and future development points towards a reflectance of ∼85%. Uniquely, compared to electrowetting pixels, the electrofluidic pixels reduce the visible area of the coloured fluid by an additional two to three times (improving contrast), are potentially bistable, are as thin as ∼15 μm (giving potential for rollable displays), and can be miniaturized without increased operating voltage.

Reflective displays use ambient light to illuminate the screen image and therefore provide superior energy efficiency, sunlight legibility, and flexible/rollable[1] form factor. Numerous technologies are vying for reflective applications: in electronic paper, high white state reflectance R (%) is critical, examples include electrophoretic[1] (E-Ink, ∼40%), electrowetting[2] (Liquavista, >50%), cholesteric liquid crystal[3] (Kent Displays Inc., ∼30%), electrochromic[4,5] (NTerra Inc., ∼45%, DIC, ∼65%), micro-electromechanical interference[6] (Qualcomm Inc., ∼25%) and liquid powder[7] (Bridgestone, ∼40%). However, all of these technologies fall well short of the visual brilliance and contrast of pigments printed onto bleached-wood fibre ($R > 80\%$). For example, electrophoretic displays and liquid powder displays are fundamentally limited by the need to place a thin white pigment layer in front of a black absorbing layer. Interference modulated displays can provide brilliant reflective colour at a single pixel, but creating a broadband and wide-angle white reflector is not achievable at the scales required for micro-electromechanical operation. Electrowetting displays currently achieve high reflectance by reconfiguring the contact angle of a coloured oil film on a planar white substrate. However, the coloured oil area is typically only reduced to ∼20–30% of the viewable area, limiting contrast. Furthermore, dyes generally lack the light stability and colour performance of pigments used in modern printed media. If reflective displays are to achieve the performance of paper, an altogether different approach will be required, and not just incremental improvements to existing technologies. Ideally, a new approach might leverage the use of high-performance pigments used in printing. Somehow, these pigments would need to be hidden to occupy less than 5–10% of the viewable area when paper-white reflection is desired. Furthermore, any new approach should use only planar photolithographic microfabrication so that the technique is suitable for manufacture.

Figure 1 presents a newly proposed 'electrofluidic' display structure that reduces the visible area of the coloured fluid by a factor of two to three more than that of an electrowetting display. The electrofluidic architecture is further distinct from electrowetting displays in its driving principles, device structure, its potential for bistability, the reduced parallax for multilayer subtractive colour pixels, its tight pixel confinement for rollable displays, and in its use of water-dispersed pigments instead of oil-soluble dyes. We chose 'electrofluidic' nomenclature because the mechanism involves charge-induced movement of liquids through microfluidic cavities.

The basic electrofluidic structure has several important geometrical features. The first is a reservoir that will hold an aqueous pigment dispersion in less than 5–10% of the visible area. The second feature is a surface channel occupying 80–95% of the visible area; this receives the pigment dispersion from the reservoir when a suitable stimulus is applied. Third, there is a duct surrounding the device that enables counterflow of a nonpolar fluid (oil or gas) as the pigment dispersion leaves the reservoir. It is important to note that all of these features are inexpensively formed in a single photolithographic or microreplication step. Several additional coatings and a top substrate are added (Fig. 1b). The surface channel is first bound by two electrowetting[8] plates consisting of an electrode and hydrophobic dielectric. The top electrowetting plate is composed of a transparent In_2O_3:SnO_2 electrode (ITO) so that the surface channel may be viewed by the naked eye. The bottom electrowetting plate comprises a highly reflective electrode made from aluminium, for example. With this arrangement, when no voltage is applied, a net Young–Laplace pressure[9] causes the pigment dispersion to occupy the cavity, which imparts a larger radius of curvature on the pigment dispersion. Therefore at equilibrium, the pigment dispersion occupies the reservoir and is largely hidden from view. This is analogous to connecting two soap bubbles by a straw—the larger bubble has a larger radius of curvature and a lower Young–Laplace pressure, and will therefore consume the smaller bubble. When a voltage is applied between the two electrowetting plates[10] and the pigment dispersion (Fig. 1c), an electromechanical[11] pressure is induced that exceeds the net Young–Laplace pressure, and the pigment dispersion is pulled into the surface channel. If the volume of the pigment dispersion is slightly greater than the volume of the surface channel, then the pigment will be simultaneously viewable in both the reservoir and the surface channel, and nearly the entire device area will exhibit the coloration of the pigment. If the voltage is removed the pigment dispersion rapidly (milliseconds to tens of milliseconds) recoils into the reservoir. Thus a switchable

[1]Novel Devices Laboratory, Department of Electrical and Computer Engineering, University of Cincinnati, Cincinnati, Ohio 45221, USA, [2]Sun Chemical Corporation, Cincinnati, Ohio 45232, USA. *e-mail: heikenjc@email.uc.edu

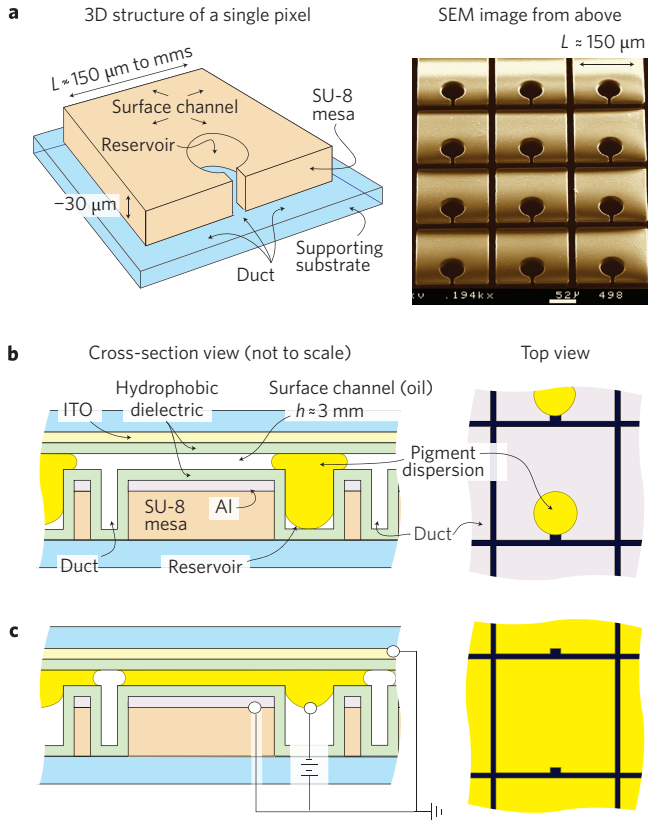

Figure 1 | The three-dimensional pixel structure and basic pixel operation. **a**, Three-dimensional diagram of a single pixel (left) and scanning electron microscope (SEM) images (right) of the SU-8 mesa structure. **b**,**c**, Cross-sections (left) and top views (right) of the pixels with no voltage (**b**) and an applied voltage (**c**) sufficient to cause the pigment dispersion to fill the surface channel.

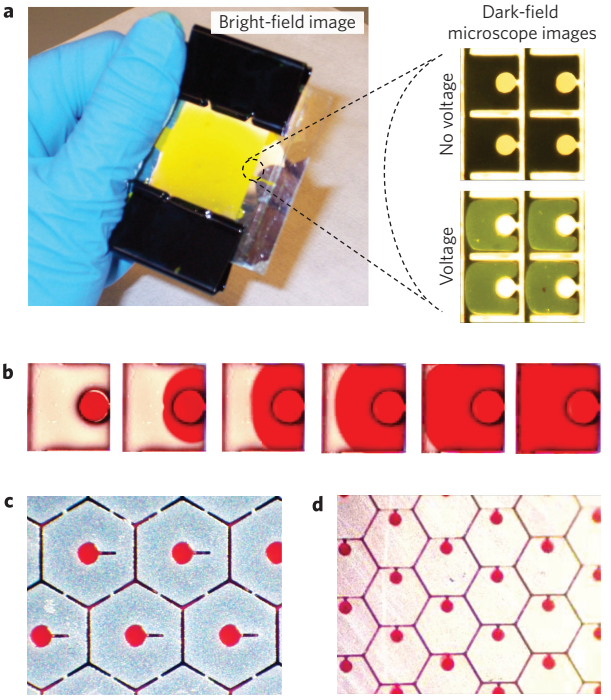

Figure 2 | Images of electrofluidic displays and pixels. **a**, Bright-field image of a 170 DPI direct-drive demonstrator with ~30,000 pixels (left) and pixel dark-field images (right). **b**, Time-lapse images of 500-μm-square pixels. **c**, Hexagonal pixel with two separate ducts, one for the reservoir and one for the pixel border. **d**, Hexagonal pixels in which the reservoir comprises only ~5% of the viewable area. Two videos of pixel operation are also provided in the Supplementary Information.

device is created that can hide the pigment or reveal the pigment with a visual brilliance that is similar to pigment printed on paper. Figure 2a presents a bright-field photograph of an assembled yellow prototype and dark-field microscope images of individual pixels. Dark-field imaging only captures scattered light from nonplanar or diffuse surfaces, and therefore highlights the self-diffuse (optically scattering) advantage of pigment dispersions. Shown in Fig. 2b–d are bright-field images of several red pigment and alternative device geometries. (See Supplementary Information for two dark-field videos of $L \approx 150$ and 300 μm pixels.) Single pixels can be as small as tens of micrometres, and in our laboratory we have demonstrated reversible switching over surface channel lengths as large as 100 cm. It is interesting to briefly note that pigment area is changed in a manner that visually mimics biological chromatophores[12] in bobtail squids[13] and chameleons.

A deeper discussion of the fundamental operating principles will now be presented. Figure 3a schematically demonstrates that the movement of pigment dispersion into or out of the surface channel is regulated by a competition between Young–Laplace pressure[9] and electromechanical[11] pressure generated by the electrowetting effect[8]. Young–Laplace pressure can be calculated from

$$\Delta p = \gamma_{ao}(1/R_1 + 1/R_2) \quad (1)$$

which includes interfacial surface tension γ_{ao} between the aqueous pigment dispersion and the oil, and the principle radii of curvature for the pigment dispersion meniscus (R_1, R_2). Typical pixels have a surface channel length ($L \approx 50$–500 μm) that is $\gg 10\times$ the channel height h. Therefore, Young–Laplace pressure in the surface channel is dominated by only a single radius of curvature R. For the materials used herein, the Young's contact angle[9] θ_Y for the pigment dispersion is $>160^\circ$, and therefore R can be further approximated as being only due to the surface channel height ($R \approx h/2$). The pigment dispersion also has a curved meniscus in the reservoir, where the radius of curvature is governed by two equal radii of curvature. However, the reservoir diameter is typically $>10\times$ the surface channel height and the Young–Laplace pressure in the reservoir is insignificantly small. Therefore at no voltage the net Young–Laplace pressure can be approximated as being due only to the surface channel: $\Delta p \approx 2\gamma_{ao}/h$. As shown in the plot of Fig. 3a, at no voltage an example device has a maximum Δp of ~3 kN m^{-2}. For the case for applied voltage an understanding of the electrowetting[8] effect is first required:

$$\cos\theta_V = \cos\theta_Y + \frac{1}{2}\frac{\varepsilon V^2}{\gamma_{ao} d} \quad (2)$$

where θ_V is the electrowetted contact angle, ε/d is the hydrophobic dielectric capacitance per unit area, and the applied d.c. voltage or a.c. r.m.s. voltage is indicated by V. As predicted by equation (2) and as shown in Fig. 3a, electrowetting reduces the pigment dispersion contact angle as the voltage is increased. Combining equations (1) and (2), the net pressure acting on the pigment dispersion in the surface channel can be approximated as

$$\Delta p \approx \frac{2\gamma_{ao}}{h} - \frac{\varepsilon V^2}{hd} \quad (3)$$

As shown in the plot and diagrams of Fig. 3a and according to equation (3), the pigment dispersion will be pulled into the

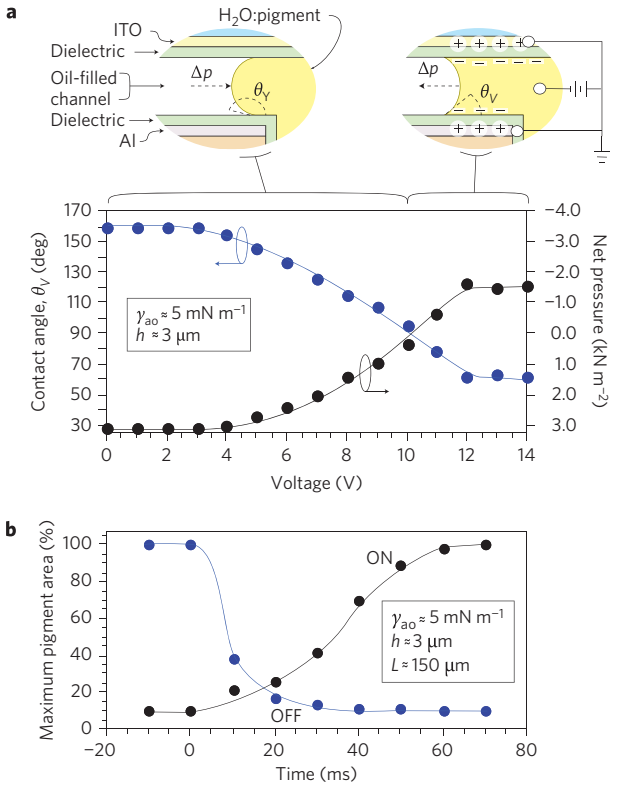

Figure 3 | Voltage and time response of electrofluidic pixel characteristics. **a**, Plot of contact angle and net meniscus pressure versus voltage, and schematic of the pigment dispersion movement in the surface channel. **b**, Pigment area versus time for 150-μm pixels.

surface channel when Δp becomes negative. Without substantial contact angle hysteresis[9], equation (2) also predicts that the threshold for pulling pigment into the surface channel is $\theta_V < 90^\circ$ (analogous to capillary wetting). For the materials used in Fig. 3, the pressure pulling the pigment dispersion into the surface channel reaches a maximum at the onset of electrowetting saturation ($V \approx 12$ V, $\theta_V \approx 60^\circ$, $h \approx 3.0$ μm, $\gamma_{ao} \approx 5$ mN m^{-1}, $\Delta p \approx -1.5$ kN m^{-2}). The electrowetting saturation is likely due to charge injection[14] into the hydrophobic dielectric. Preliminary tests were also performed with alternative aqueous/oil/dielectric materials and with ~30–100 Hz bipolar voltages like those used in displays. These tests showed less charge injection and contact angles as low as $\theta_V \approx 30^\circ$ (with a larger range for Δp). Higher surface tension can also be used to achieve values of Δp of ~–17 kN m^{-2}, as demonstrated with d.c. voltage and a carbon black pigment dispersion ($\theta_V \approx 70^\circ$, $h \approx 2.0$ μm, $\gamma_{ao} \approx 50$ mN m^{-1}). We have also recently validated full pixel ON/OFF contrast for a materials system with a value of $\theta_Y \approx 105^\circ$ and $\theta_V \approx 75^\circ$. We note this achievement because electrofluidic pixels therefore require less contact angle change than conventional electrowetting pixels ($\theta_Y \approx 180^\circ$, $\theta_V \approx 90$–120°). Furthermore, unlike electrowetting pixels, electrofluidic pixels do not require increased operating voltage as the pixel size is scaled down[15]. These opportunities for reduced operating voltage (electric field) are important because they can reduce the occurrence of electrolysis (dielectric breakdown).

For all the examples discussed above, the duct design shown in Fig. 1a has been effective at terminating advancement of the pigment dispersion at the end of the surface channel. The physics governing this termination has two origins: (i) the duct marks the end of the aluminium electrode; (ii) the dispersion encounters a diverging capillary geometry at the channel/duct interface. Thus the duct is further important as it prevents merging of pigment dispersions in adjacent pixels. Regarding intermediate pigment positioning (grey scale), for voltages implemented near the ideal threshold of $\Delta p = 0$ the pigment dispersion could be held at various positions. The voltage range for stability can be determined from equation (3) by incorporating the effects of contact angle hysteresis[8,9]. Contact angle hysteresis is typically only a few degrees in oil (<0.1–1 kN m^{-2}), but it can be increased by providing a rough or patterned hydrophobic dielectric (~1s of kN m^{-2}).

We will now provide a proper explanation of why the pushing and pulling of the pigment dispersion should be considered as the result of the net pressure between Young–Laplace and electromechanical pressure. It has been experimentally demonstrated[16] that the local microscopic contact angle at the contact line is always Young's (θ_Y). The electrowetted contact angle (θ_V) is only a projection that is macroscopically observed at a distance from the solid surface that is roughly equal to the hydrophobic dielectric thickness (d). Therefore, for the surface channel geometries used herein ($h \approx$ 1s of micrometres) and dielectric thicknesses ($d \approx$ 0.1s to 1s of micrometres), the meniscus geometry will exhibit a more complex curvature than the simple diagram shown in Fig. 3a. Consequently, it is appropriate to use equations (2) and (3), but with the understanding that movement of the pigment dispersion with voltage should not be directly attributed to contact angle change. Some further clarifications are provided. At 12 V the total electromechanical pressure is approximately –4.5 kN m^{-2}, which simply exceeds the ~3.0 kN m^{-2} Young–Laplace pressure, resulting in a net pressure of approximately –1.5 kN m^{-2}, as shown in Fig. 3. We previously stated that our maximum achievable net pressure was approximately –17 kN m^{-2}. This net pressure is the sum of ~50 kN m^{-2} Young–Laplace pressure and approximately –67 kN m^{-2} electromechanical pressure. These descriptions are all consistent with equation (3).

This understanding of pressure is critical to the next topic of discussion: the potential for video switching speed (~10–20 ms). As shown in Fig. 3b, the demonstrated ON speed for filling 90% of the maximum pigment area is currently $t_{ON} \approx 50$ ms for 150-μm electrofluidic display pixels. It is notable that the OFF speed in Fig. 3b is ~2× faster than the ON speed, which is in agreement with the ~2× difference in magnitude of Δp shown in Fig. 3a. Next, consider theoretical speed for 170 DPI colour pixels, where the RGB subpixel size would be $L \approx 50$ μm. As a first approximation, this smaller L will decrease t_{ON} by ~9× as the distance travelled is reduced by 3× and as the liquid velocity U is increased 3× according to $U \propto h/L$ (ref. 17). t_{ON} could also be decreased by ~10× through previously mentioned materials that yield $\Delta p \approx 17$ kN m^{-2}. Now, consider how the current $t_{OFF} \approx 25$ ms would be affected by scaling and materials optimization. Again, device scaling to $L \approx 50$ μm provides a 9× decrease in t_{OFF}, and the case for an optimized Δp provides a ~15× decrease in t_{OFF} ($\Delta p \approx$ –50 kN m^{-2}). Finally, the oil and pigment viscosities are ~2 cSt and could be potentially reduced to ~1 cSt, resulting in a 2× decrease in both t_{ON} and t_{OFF}. The net effect of the above design changes predicts a minimum t_{ON} and t_{OFF} that is well below 1 ms. Such speed is far faster than that required for video, and only a small fraction of the abovementioned improvements are needed.

Our last detailed discussion is on display brightness as determined by pigments, reflectors, fill factor and pixel architecture. Brilliant coloration is achieved by transposing a ~10–15 wt% pigment dispersion in front of a high-performance reflector such as aluminium. This approach is conceptually unique and has several advantages over other pigment-based display devices such as electrophoretic[1] or liquid powder[7] displays. It should be noted that electrofluidic devices can also operate with the dye-coloured oil and clear water used in electrowetting displays[2]. However, aqueous pigment dispersions provide a significant performance boost over dyes[2] for the following reasons: (i) they are self-diffuse

(optically scattering) for an inherently wide view angle; (ii) they generally provide superior light fastness due to reduced surface area exposure to oxygen, light or water[18]; (iii) at high concentrations (>10 wt%) pigment dispersions typically allow a wider range of interfacial surface tension (γ_{ao} ~5 to ~50 mN/m) than dyes in oil[19]; (iv) pigments are aqueous-dispersed, so even at ~10 wt% a very low viscosity is achieved (~2 cSt); (v) unlike coloured oil, coloured water allows electrically conductive colorants such as carbon-black to be used. The custom pigment dispersions developed for electrofluidic displays were provided by Sun Chemical Corp. A diffusely reflective white state is also required for a wide viewing angle. Although not shown here, diffuse white coloration can be achieved by using a diffuse or translucent oil, by using a textured aluminium reflector, or by using the ~tens of micrometres thickness of the polymer mesa to build up a diffusely reflecting layer. For a maximally bright white or coloured state, a high-performance reflector is required. An aluminium reflector system is used for the device shown in Fig. 2. When dielectric-protected, this aluminium reflector has a measured R of >93%. Even higher reflectivity is possible if the aluminium is placed beneath a mesa or dielectric containing $BaTiO_3$ powder. Also, $R > 98\%$ across the visible spectrum is available with a multilayer polymer dielectric reflector similar to 3M Vikuiti ESR. Consider a 150-μm-wide pixel (L), with a surface channel height of 3 μm (h), and with a 2-μm-wide duct (regarding fabrication challenges, the duct does not need to reach all the way to the lower substrate). An aluminium reflector can enable a white state reflectance of $R > 77\%$ or >90% as theoretically calculated for a ratio of surface channel to reservoir area of 10:1 or 20:1, respectively. For a carbon-black pigment dispersion with <5% reflectance, the theoretical contrast ratio can therefore range from >15:1 to >18:1. Interestingly, conventional offset printed ink films are ~2 μm thick and may typically contain about 15–25% pigment. Therefore the combination of pigment loading and thickness of the electrofluidic pixel can provide a degree of saturation similar to conventional printed media. It should be noted that to achieve such performance the films on the top substrate must be optimized in thickness and refractive index to minimize Fresnel reflections. Although we have not yet optimized the reflective aluminium electrode, the top substrate, or pixel geometry for ~80–90% white reflectance, we can report on preliminary prototype results. 1-inch diagonal direct-drive prototypes have been demonstrated at pixel sizes of a few millimetres, 500 μm, 300 μm and 150 μm (~30,000 pixels). Greater than 98% pixel yield has been achieved at the 300 μm pixel size. Several combinations of white diffuse, coloured (C, M, Y or R), and opaque black (K) liquids have been tested. Prototypes with ~300-μm pixels already provide a switchable white/black reflectivity of ~55%/~8% (~7:1). The development tasks for achieving >80% reflectivity and ~20:1 contrast ratio are a fairly straightforward improvement of existing device features: the aluminium reflector ($R \approx 70\%$), the reflective area (~75%), and the antireflection coating of the front glass ($R \approx 5\%$). Progress is under way, as recent single pixel tests now show >90% reflective area. Full-colour operation requires a more sophisticated pixel architecture. As illustrated in Fig. 4a, a high-efficiency black/white electrofluidic pixel can be combined with a RGBW colour filter array[20]. This could theoretically result in a ~40% white state brightness (like the existing Amazon Kindle™ but with the advantage of offering full colour images). Also shown in Fig. 4a, an even higher full-colour brightness of >60% is theoretically possible if a two-layer subtractive CMY approach is used, similar to that that proposed for electrowetting[2] cholesteric[21] displays. The electrofluidic CMY pigment dispersions developed by Sun Chemical have the spectra shown in Fig. 4b, and are shown in Fig. 4c. It should be noted for the two-layer CMY approach that the geometry and coloured fluid positioning in electrofluidic pixels is further distinct from electrowetting pixels

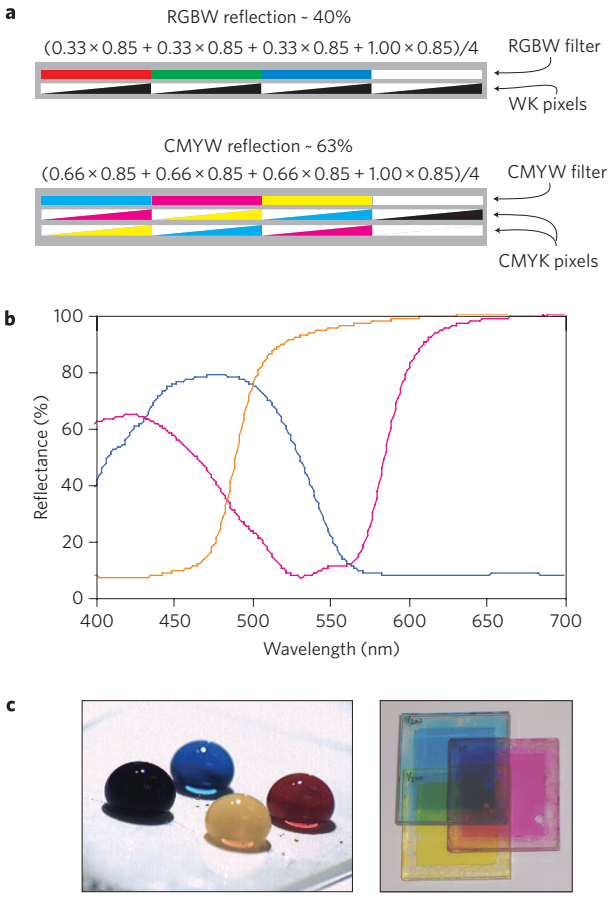

Figure 4 | Colour filtering techniques and materials that are required for full-colour electrofluidic displays. a, Red-green-blue-white[20] (RGBW) and cyan-magenta-yellow-white (CMYW) pixel architectures. **b**, CMY pigment reflectance spectra. **c**, Images of pigment droplets and an overlay of three CMY prototypes.

in terms of parallax. For 300 DPI electrofluidic pixels the theoretical view angle is >45° before ~10% parallax arises. Although substantially more difficult to manufacture, use of three stacked CMY electrofluidic pixels is possible. The brightness of such an approach could equal that of printed media, but is likely limited to larger sized pixels such as those used in signage and indicators.

Thus far we have discussed the positive benefits and potentials for electrofluidic displays. However, research and development challenges should be briefly presented. First, the simple drive scheme shown in Fig. 1 does not provide analogue grey scale. Challenges to grey-scale operation include error accumulation (as in electrophoretic displays) and pixel capacitance that varies with grey-scale state (as in electrowetting displays). Therefore patterned electrodes or surfaces should be implemented for an analogue response or to create intermediate grey-scale reset states. Several simple yet promising grey-scale architectures are now in development. For electronic paper, bistable grey scale is highly desirable to eliminate power consumption once an image is selected. 'Droplet-driven' electrowetting displays[22] are bistable, but only allow two-bit grey scale. Advanced electrofluidic pixel concepts can theoretically provide bistable operation and analogue (numerous) grey-scale states. Regarding aging, electrolysis (dielectric breakdown) must be avoided, and as previously discussed there may be a lower voltage (electric field) advantage over conventional electrowetting displays. For applications such as rollable displays, adherent substrate spacers[23] comprising ~1–3% of the pixel area must be developed. Creating a full-colour reflective display is a highly challenging task for any technology, let alone

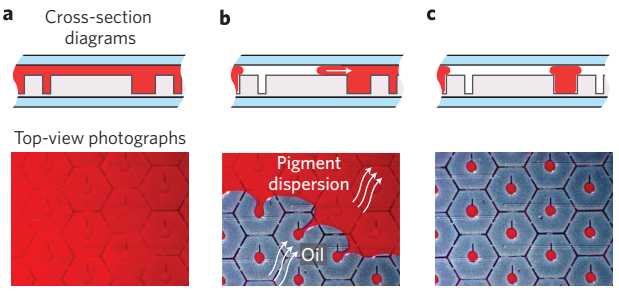

Figure 5 | The liquids in electrofluidic displays can be dosed by means of self-assembly. a,**b**, The pigment dispersion is first vacuum filled (**a**) similar to liquid dosing in a liquid-crystal display, then oil is introduced (**b**) at one edge of the display and the pigment recedes from the channel due to Young–Laplace pressure. However, the oil in the channel moves past the reservoir before pigment is removed from the reservoir (the reservoir has a larger cavity and lower Young–Laplace pressure). **c**, The completed dosing. A video of the liquid dosing is provided in the Supplementary Information.

electrofluidic displays, which have numerous geometries and materials not previously seen in displays. Full-colour operation requires repeatable liquid dosing. As shown in Fig. 5 we have developed a simple liquid self-assembly process that is governed by Young–Laplace pressure. The self-assembly process works well for the 1-inch demonstrator units, and scalability to larger sizes is in development. (See Supplementary Information for a video of the self-assembly process.) In addition to liquid dosing, we have made substantial efforts to ensure manufacturability. As detailed in the Methods, pixel fabrication only requires simple vacuum deposition, photolithography and wet-processing techniques. It is also interesting to note that the fabrication of the bottom substrate is identical in composition and number of steps to the fabrication of low-cost electrowetting displays[15], with only the geometry and sequencing of materials being different. Taking these challenges into account, we are now beginning to develop a more advanced prototype to fully demonstrate that electrofluidic displays can achieve performance equivalent to the centuries-old brilliance of pigments printed on paper.

Methods

The simplest embodiment of a direct-drive electrofluidic prototype was fabricated as follows. The entire process can be implemented with temperatures as low as ~100–120 °C and is likely compatible with organic transistors and flexible plastic substrates. First, Microchem SU-8 epoxy was photolithographically patterned to create the mesa structure shown in Fig. 1. As an alternative, the mesa structure can be created more quickly and at lower cost by using embossing/microreplication techniques similar to Sipix Microcup™ technology. Next, a reflective aluminium electrode and a dielectric such as Al_2O_3 or Parlyene C was vacuum deposited. The electrode was patterned and pixilation created by using angled deposition or photoresist patterning and wet-etching. These films were then further solution coated with Cytonix Fluoropel 1601V or Asahi Cytop 809M fluoropolymer. The dielectric and fluoropolymer comprise the hydrophobic dielectric shown in Figs 1 and 3. The array of pixels was dosed with dodecane oil and a ~10–15 wt% pigment dispersion provided by Sun-Chemical Corp. The liquid dosing, as shown in Fig. 5, uses a new self-assembly approach that expands upon our existing self-assembly capabilities[15] for electrowetting displays. The top substrate, which seals the device, included a ~50-nm thin In_2O_3:SnO_2 film and another hydrophobic dielectric. The top plate further included a patterned SU-8 spacer to regulate the surface channel height. Devices were temporarily sealed with rubber gaskets and binder-clips or permanently sealed with UV epoxy.

Received 6 October 2008; accepted 23 March 2009; published online 26 April 2009

References

1. Huitema, H. E. A. *et al.* Flexible electronic-paper active-matrix displays. *J. Soc. Inf. Display* **14,** 729–733 (2006).
2. Hayes, R. A. & Feenstra, B. J. Video-speed electronic paper based on electrowetting. *Nature* **425,** 383–385 (2003).
3. Khan, A. *et al.* Reflective cholesteric LCDs for electronic paper applications. *Proc. International Display Manufacturing Conference* 397–399 (2005).
4. Back, U. *et al.* Nanomaterials-based electrochromics for paper-quality display. *Adv. Mater.* **14,** 845–848 (2002).
5. Nakashima, M. *et al.* Naturally white electrochromic display using organic/inorganic nanocomposite pulp. *SID Symp. Dig.* **36,** 1678–1681(2005).
6. Miles, M. *et al.* Digital paper for reflective displays. *J. Soc. Inf. Display* **11,** 209–215 (2003).
7. Hattori, R. *et al.* A novel bistable reflective display using quick-response liquid powder. *J. Soc. Inf. Display* **12,** 75–80 (2004).
8. Mugele, F. & Baret, J. Electrowetting: from basics to applications. *J. Phys. Condens. Matter* **17,** R705–R774 (2005).
9. Berthier, J. *Microdrops and Digital Microfluidics* (William and Andrew, 2008).
10. Fair, R. Digital microfluidics: is a true lab-on-a-chip possible? *Microfluidics Nanofluidics* **3,** 245–281 (2007).
11. Jones, T. B. An electromechanical interpretation of electrowetting. *J. Micromech. Microeng.* **15,** 1184–1187 (2005).
12. Hanlon, R. T. & Messenger, J. B. *Cephalopod Behaviour* (Cambridge Univ. Press, 1998).
13. Kramer, R. M., Crookes-Goodson, W. J. & Naik, R. R. The self-organizing properties of squid reflectin protein. *Nature Mater.* **6,** 533–538 (2007).
14. Verheijen, H. & Prins, M. Reversible electrowetting and trapping of charge: model and experiments. *Langmuir* **15,** 6616–6620 (1999).
15. Sun, B. *et al.* Scalable fabrication of electrowetting displays with self-assembled oil dosing. *Appl. Phys. Lett.* **91,** 011106 (2007).
16. Mugele, F. & Buehrle, J. Equilibrium drop surface profiles in electric fields. *J. Phys. Condens. Matter* **19,** 375112 (2007).
17. Song, J., Evans, R., Lin, Y. Y., Hsu, B. N. & Fair, R. A scaling model for electrowetting-on-dielectric microfluidic actuators. *Microfluidics Nanofluidics* http://dx.doi.org/10.1007/s10404-008-0360-y (2009).
18. Cristea, D. & Vilarem, G. Improving light fastness of natural dyes on cotton yarn. *Dyes and Pigments* **70,** 238–245 (2006).
19. Roques-Carmes, T. *et al.* The effect of the oil/water interfacial tension on electrowetting driven fluid motion. *Colloids Surf. A* **267,** 56–63 (2005).
20. Brown Elliot, C., Credelle, T. & Higgins, M. Adding a white subpixel. *Inf. Display* **5,** 26–31 (2005).
21. Shiyanovskaya, I. *et al.* Single substrate coatable multicolor cholesteric liquid crystal displays. *Proc. Soc. Inf. Display* **38,** 65–68 (2007).
22. Blankenbach, K. *et al.* Novel highly reflective and bistable electrowetting displays. *J. Soc. Inf. Display* **16,** 237–244 (2008).
23. Jang, S. *et al.* Tight bonding of two plastic substrates for flexible LCDs. *Proc. Soc. Inf. Display* **38,** 653–656 (2007).

Acknowledgements

The authors acknowledge partial financial support for Cincinnati's general program in displays by Sun Chemical Corp., Motorola (K. Dean), Polymer Vision (E. Huitema), ITRI Taiwan (W. Cheng), Air Force Research Labs (R. Naik), Air Force Office of Scientific Research (AFOSR) Young Investigator Award no. 06NE223 (K. Reinhardt), and an National Science Foundation (NSF) CAREER Award no. 0640964 (Electronics Photonics & Device Technologies (EPDT)). The authors thank R. Fair of Duke University for discussion on switching speed in microscale electrowetting cavities.

Additional information

Supplementary information accompanies this paper at www.nature.com/naturephotonics. The authors declare competing financial interests: details accompany the full-text HTML version of the paper at www.nature.com/naturephotonics. Reprints and permission information is available online at http://npg.nature.com/reprintsandpermissions/. Correspondence and requests for materials should be addressed to J.H.

nature photonics

ARTICLES

PUBLISHED ONLINE: 26 APRIL 2009 | DOI: 10.1038/NPHOTON.2009.69

Bulk heterojunction solar cells with internal quantum efficiency approaching 100%

Sung Heum Park[1,2], Anshuman Roy[1], Serge Beaupré[3], Shinuk Cho[1,2], Nelson Coates[1], Ji Sun Moon[1,2], Daniel Moses[1], Mario Leclerc[3], Kwanghee Lee[1,2]* and Alan J. Heeger[1,2]*

We report the fabrication and measurement of solar cells with 6% power conversion efficiency using the alternating co-polymer, poly[*N*-9′′-hepta-decanyl-2,7-carbazole-alt-5,5-(4′,7′-di-2-thienyl-2′,1′,3′-benzothiadiazole) (PCDTBT) in bulk heterojunction composites with the fullerene derivative [6,6]-phenyl C_{70}-butyric acid methyl ester ($PC_{70}BM$). The PCDTBT/$PC_{70}BM$ solar cells exhibit the best performance of any bulk heterojunction system studied to date, with $J_{SC} = 10.6$ mA cm^{-2}, $V_{OC} = 0.88$ V, $FF = 0.66$ and $\eta_e = 6.1\%$ under air mass 1.5 global (AM 1.5 G) irradiation of 100 mW cm^{-2}. The internal quantum efficiency is close to 100%, implying that essentially every absorbed photon results in a separated pair of charge carriers and that all photogenerated carriers are collected at the electrodes.

Polymer bulk heterojunction (BHJ) solar cells based on composites of an electron-donating conjugated polymer and an electron-accepting fullerene offer promise for the realization of a low-cost, printable, portable and flexible renewable energy source[1–4]. Although BHJ solar cell performance has steadily improved, with power conversion efficiencies (PCE $\equiv \eta_e$) approaching 5%, further improvements in efficiency are required for large-scale commercialization[5–7].

Rather than using a single junction architecture, the fundamental BHJ concept involves the self-assembly of nanoscale heterojunctions by spontaneous phase separation of the donor (polymer) and the acceptor (fullerene). As a result of this spontaneous phase separation, charge-separating heterojunctions are formed throughout the bulk of the material[2].

Over the past decade, research has focused on regio-regular poly(3-hexylthiophene) (P3HT) as the standard electron-donating material in polymer BHJ solar cells, with important progress having been made in understanding the device science and the associated improvements in device efficiency. Relatively high-performance polymer BHJ solar cells made from a mixture of P3HT and [6,6]-phenyl C61 butyric acid methyl ester (PCBM) have been reported, with maximum PCEs of $\eta_e = 4$–5% (refs 5–7). Although approaches to improving the efficiency of P3HT/PCBM cells are still being reported, the relatively large bandgap of P3HT ($\sim$1.9 eV) limits the fraction of the solar spectrum that can be harvested, and the relatively small energy difference between the top of the π-band (highest occupied molecular orbital, HOMO) of P3HT and the lowest unoccupied molecular orbital (LUMO) of the fullerene acceptor results in a low open-circuit voltage, $V_{OC} \approx 0.6$ V. These fundamental energies defined by the electronic structure of the semiconducting polymer (the energy gap and the HOMO energy) must be decreased in order achieve polymer BHJ solar cells with PCEs of 6% and higher.

Recently, several classes of low-bandgap polymers have been developed to better harvest the solar spectrum with deeper HOMO energies that can potentially increase V_{OC} (refs 8–12). These polymers are designed to make use of internal charge transfer from an electron-rich unit to an electron-deficient moiety within the fundamental repeat unit. Among them, alternating co-polymers based on poly(2,7-carbazole) derivatives[11,12], with a suite of electron-deficient moieties to choose from, are particularly interesting (see Fig. 1). The different electron-deficient moieties can be used to tune the electronic energy gap of the semiconducting polymer, while the deep HOMO of the carbazole leads to higher values for V_{OC} (ref. 11). The implied flexibility in the synthesis can lead to both a smaller bandgap that enables the harvesting of a larger fraction of the solar radiation spectrum, and a deeper HOMO energy that increases the open circuit voltage of the photovoltaic device. In their initial report of the synthesis and device performance of PCDTBT, Leclerc and colleagues demonstrated a PCE of 3.6% from a BHJ cell with V_{OC} value approaching 0.9 V (ref. 12).

We report here solar cells with 6% PCE from BHJ composites comprising PCDTBT/[6,6]-phenyl C71 butyric acid methyl ester ($PC_{70}BM$) with short-circuit current $J_{SC} = 10.6$ mA cm^{-2}, open circuit voltage $V_{OC} = 0.88$ V and fill factor $FF = 0.66$ under air mass 1.5 global (AM 1.5 G) irradiation of 100 mW cm^{-2}. The internal quantum efficiency (IQE) is close to 100%, implying that essentially every absorbed photon results in a separated pair of charge carriers and that all photogenerated carriers are collected at the electrodes.

Titanium oxide optical spacer and hole blocking layer

Historically, a relatively low PCE has been demonstrated in polymer solar cells made from polymers that make use of the internal charge transfer concept, including PCDTBT[11,12]. This low PCE has been limited by the relatively low photocurrent obtained from these devices. In BHJ cells, the photocurrent generation is governed by two main factors[13,14]: (i) the fractional number of absorbed photons in the active layer (relative to the total flux of photons from the solar spectrum) and (ii) the IQE defined by the fraction of collected carriers per absorbed photon. In principle, one can simply increase the thickness of the active layer to absorb more light. However, because of the relatively low carrier mobility of the disordered materials (cast from solution with subsequent phase separation), increasing the thickness increases the internal resistance of the device. Consequently, the fill factor typically

[1]Center for Polymers and Organic Solids, University of California at Santa Barbara, Santa Barbara, California 93106, USA, [2]Heeger Center for Advanced Materials, Gwangju Institute of Science and Technology, Gwangju 500-712, South Korea, [3]Department of Chemistry, University of Laval, G1K 7P4 Quebec City, Quebec, Canada. *e-mail: klee@gist.ac.kr; ajhe@physics.ucsb.edu

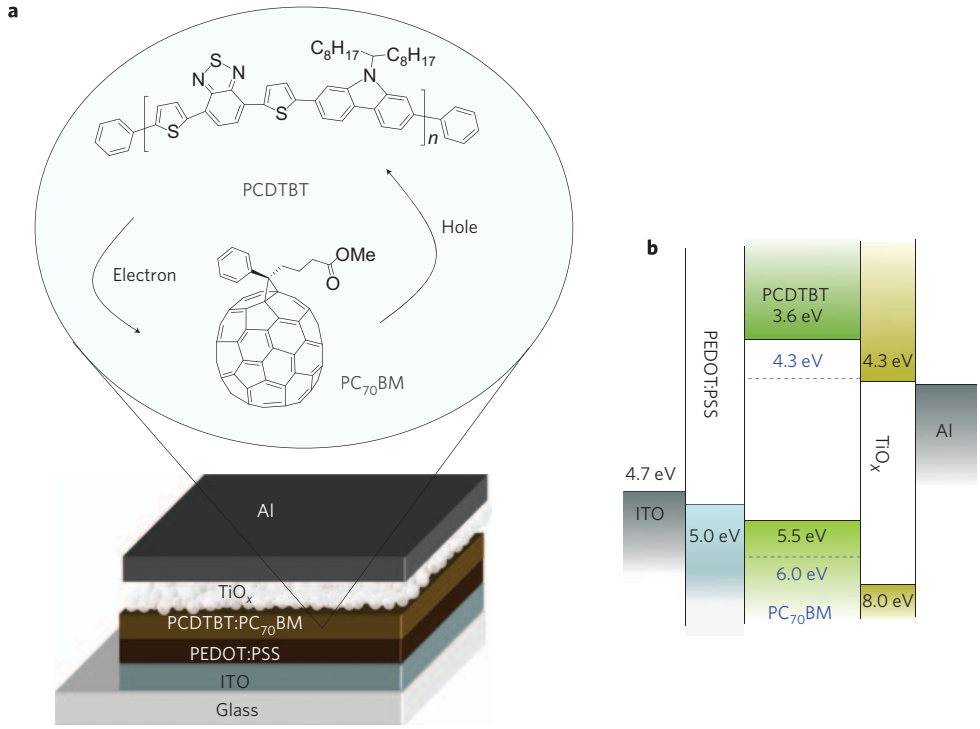

Figure 1 | Device structure and energy level diagram of the components. a, The bulk heterojunction (BHJ) film is a phase separated blend of PCDTBT and $PC_{70}BM$. The inset shows the transfer of photogenerated electrons from PCDTBT to $PC_{70}BM$. The titanium oxide (TiO_x) layer is introduced as an optical spacer on top of the BHJ layer. **b**, Energy level diagram of the components of the device.

plummets as the thickness is increased. Based on this simple analysis, we consider the following approach towards obtaining higher photocurrent: maximizing the photon absorption for a fixed active layer thickness while simultaneously improving the IQE.

To increase the photocurrent while keeping the thickness fixed, we used an optical spacer between the photo-active layer and the top electrode; because of the optical spacer, the maximum light intensity is redistributed to be within the active charge separating BHJ layer. The utility of the optical spacer has been reproduced in recent publications[15]. In parallel, by choosing optimal conditions for processing, we have demonstrated a nanoscale BHJ morphology that results in nearly 100% IQE. This dual focused approach applied to PCDTBT/$PC_{70}BM$ results in PCE, $n_e \geq 6\%$; the highest value reported to date for polymer BHJ solar cells.

Figure 1 shows the structure of the BHJ device together with the molecular structures and an energy level diagram of the component materials. From the fundamental physics of the open-circuit voltage associated with the donor–acceptor heterojunction and the empirical relationship demonstrated in refs 16–18, the relatively deep HOMO energy of PCDTBT, ~5.5 eV, should result in a higher open-circuit voltage. Moreover, because the spherical symmetry of the fullerene has been lifted in $PC_{70}BM$ (compared to PCBM), the PCDTBT/$PC_{70}BM$ BHJ material has higher absorption and, consequently, enhanced photocurrent[19,20].

The solution processible titanium sub-oxide (TiO_x) layer[15,21,22] was introduced as an optical spacer[21] and as a hole blocker[23] (see Supplementary Information) between the BHJ layer and the top metal electrode. The TiO_x layer redistributes the light intensity within the BHJ by changing the optical interference between the incident light and the light reflected from the metal electrode[24,25]. As the active layer thickness decreases, the intensity of reflected light increases, and the optical interference effect becomes more pronounced. Hence, we expect that the efficacy of the TiO_x layer will be higher for thinner active layers. Hole blocking by the TiO_x is also more important for thinner-film devices. In the PCDTBT:$PC_{70}BM$ solar cells reported here, the thickness of the active layer is ~80 nm, and the TiO_x layer thickness is ~10 nm. With this configuration, we are able to make good use of the optical spacer by avoiding destructive interference within the charge separating layer between the incident light and the light reflected from the aluminium–TiO_x interface. In addition, the bottom of the conduction band of TiO_x matches the LUMO of $PC_{70}BM$. Finally, the relatively high electron mobility of $PC_{70}BM$ and the hole-blocking feature of TiO_x enable efficient electron collection without a significant increase in the series resistance[21–23].

Figure 2a shows the absorption spectra of PCDTBT solar cells with and without the TiO_x layer. The total absorption by the active layer (including the doubled path length in the BHJ layer as a result of reflection from the aluminium electrode) was measured in reflection geometry as illustrated in the inset of Fig. 2a. Comparing two devices with the same active layer thickness (80 nm), a substantial enhancement in absorption is observed in the device with the TiO_x layer. Consequently, as shown in Fig. 2b, the device with the TiO_x layer demonstrates higher IPCE (incident photon-to-current efficiency) throughout the visible range compared with the device without the TiO_x layer. Because the integration of the product of the IPCE with the AM 1.5 solar spectrum is equal to the short-circuit current, the higher short-circuit current (see Fig. 2c) of the device with TiO_x is consistent with the higher IPCE values.

Nanoscale morphology and photocurrent generation

Note, however, that the photocurrent is determined by the product of the total number of absorbed photons within the solar spectrum and the IQE of the device[26–28]. The IQE is determined by a three-step process[26–28]: (i) migration/diffusion of the photogenerated excitations to the PCDTBT/$PC_{70}BM$ interface; (ii) exciton dissociation and charge separation at the interface; and (iii) collection of charge carriers at the ITO and aluminium electrodes. Because of step (i), the nanoscale phase separation in BHJ materials must be less than 20 nm because the exciton diffusion length is generally less than

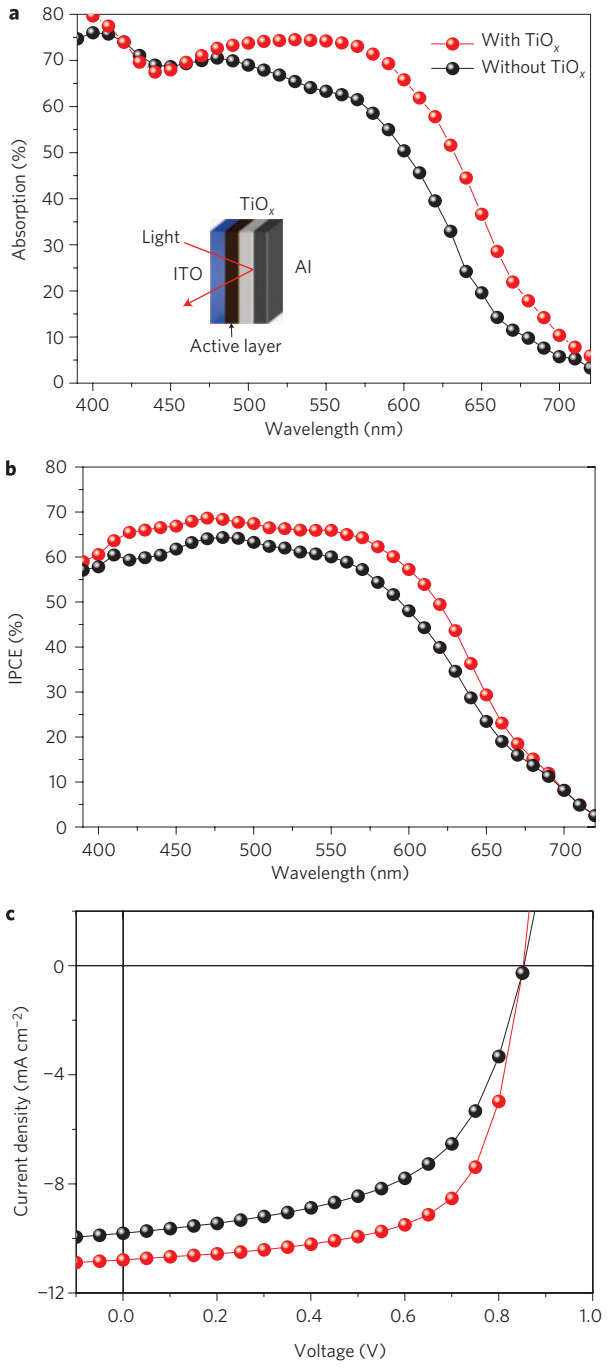

Figure 2 | The effects of TiO_x layer as an optical spacer on device performance. a, Total absorption in the active layer measured in a reflection geometry with the TiO_x layer (red symbols) and without the TiO_x layer (black symbols). The inset shows a schematic of the device structure. **b**, Incident photon-to-current efficiency (IPCE) spectra with the TiO_x layer (red symbols) and without the TiO_x layer (black symbols). **c**, Current density versus voltage characteristics (*J*–*V*) of the device with the TiO_x layer (red symbols) and without the TiO_x layer (black symbols).

10 nm (refs 29,30). In addition, smaller-scale phase separation creates larger-area PCDTBT:$PC_{70}BM$ interfaces where charge separation can take place. For step (ii), a sufficiently large energy difference between the PCDTBT LUMO and the $PC_{70}BM$ LUMO is required for ultrafast photoinduced electron transfer. For step (iii), both the PCDTBT and $PC_{70}BM$ phases must form percolated networks with few charge-trapping sites or 'dead ends'. The ultrafast photo-induced charge transfer (<100 fs) at the polymer–fullerene interface ensures that the charge separation efficiency approaches 100% (refs 2,31,32). Hence, the molecular organization and morphology on the nanometre scale as described by steps (i) and (ii), and the nanoscale morphology and the interface between the cathode and the TiO_x/BHJ as described in step (iii), provide the route to high IQE.

The nanoscale morphology of the PCDTBT:$PC_{70}BM$ BHJ is strongly affected by processing parameters such as choice of solvents, blend ratio of PCDTBT to $PC_{70}BM$, solution concentration, thermal annealing, and the molecular structure of the component materials[33–35]. In our experiments, thermal annealing of the PCDTBT:$PC_{70}BM$ system at high temperatures reduced the *FF*, J_{SC} and V_{OC} (see Supplementary Information). Thus, the use of thermal annealing is eliminated as a strategy for improving device performance. However, it is well known that for polymer-based solar cells, performance is strongly affected by both the solvent and the blend ratio[33–36]. This is expected because the solvent is known to affect the BHJ domain size, and the donor/acceptor blend ratio determines the formation of percolated networks.

Figure 3a–c shows defocused[37,38] transmission electron microscope (TEM) images of PCDTBT:$PC_{70}BM$ (1:4 ratio) films dissolved in chloroform (CF), chlorobenzene (CB) and dichlorobenzene (DCB), respectively. Although large dark clusters (200 and 300 nm) are observed in the CF and CB films, clearly defined nanoscale phase separation is observed in the film cast from DCB. These features are also observed in the surface phase images measured by atomic force microscopy (AFM), as shown in the insets of the TEM images. The higher electron density of $PC_{70}BM$ compared with PCDTBT causes electrons to be scattered more efficiently by the $PC_{70}BM$ from the TEM beam. Thus, the darker regions in the TEM images are regions of phase-separated $PC_{70}BM$. Because the exciton diffusion length (<10 nm) is much smaller than the 200–300 nm features seen in Fig. 3a,b, photo-generated excitons will often recombine before reaching the interfaces in films cast from solution in CB or CF, causing reduced charge carrier generation at the interfaces and a concomitant loss of photocurrent.

Figure 3d shows the IPCE spectra of solar cells comprising BHJ films cast from CF, CB, DCB and from a mixture of CB and DCB. The cell fabricated with a BHJ film cast from DCB has a higher IPCE over the entire excitation spectrum compared to devices comprising films cast from either CF or CB. Processing from a mixture of DCB and CB also increases the IPCE compared to processing from pure CB. Increasing the amount of DCB in the CB/DCB mixture increases the contribution from $PC_{70}BM$ to the IPCE, as is evident from the pronounced peaks around 400 and 450 nm.

Figure 3a–c demonstrates that DCB results in significantly smaller nanoscale phase separation. Therefore, the increased IPCE shown in Fig. 3d and obtained from devices made with films cast from pure DCB or from mixtures of CB and DCB results from the nanoscale phase separation. The enhanced J_{SC} and higher *FF* (see Fig. 3e) imply the formation of well-connected percolated networks for each of the phase-separated components (donor and acceptor). Thus, using DCB evidently also leads to better-connected percolated networks, which, in combination with the nanoscale phase separation, improve the device performance.

Obviously, the connectivity is sensitive to the blend ratio of PCDTBT to $PC_{70}BM$. Figure 4a–d shows TEM images of PCDTBT:$PC_{70}BM$ films cast from DCB with increasing amounts of $PC_{70}BM$. As the amount of $PC_{70}BM$ progressively increases, the nanoscale phase separation can be seen more clearly, with gradual emergence of a 'fibrillar' PCDTBT nanostructure. This fibrillar PCDTBT nanostructure is most pronounced in films at the 1:4 blend ratio, implying that increasing the amount of $PC_{70}BM$ causes the PCDTBT network to form longer and better connected pathways.

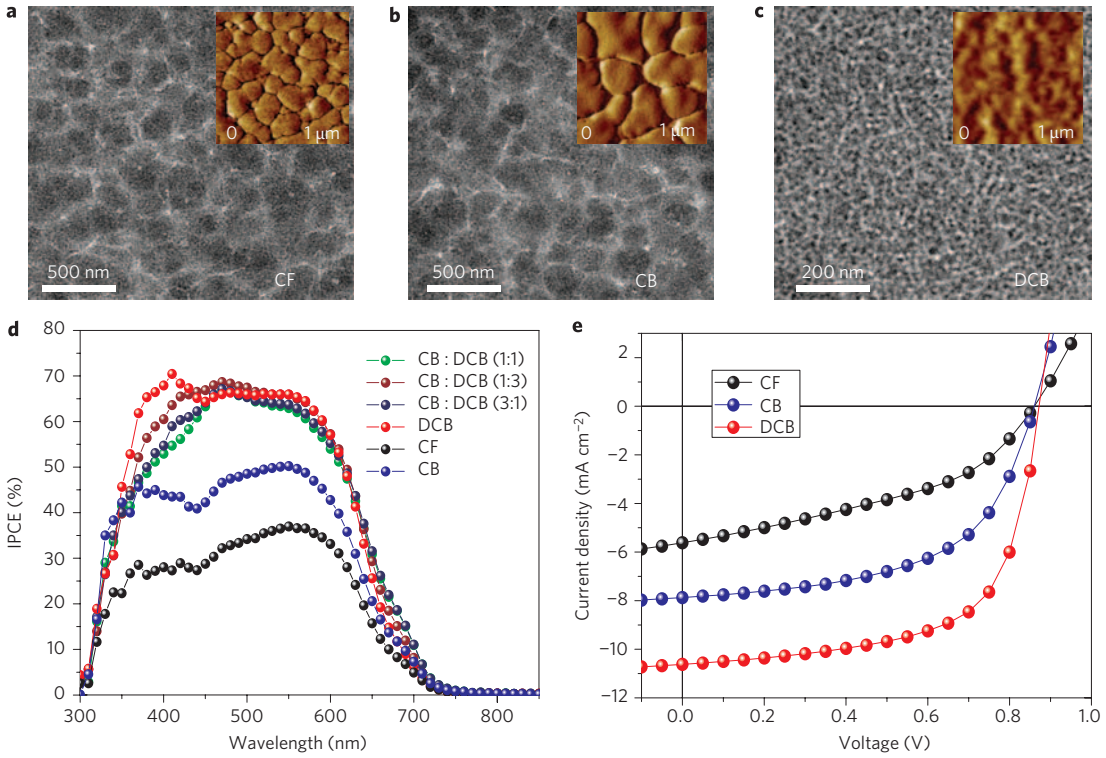

Figure 3 | The effects of CF, CB and DCB solvents on film morphology and device performance. a–c, TEM images of PCDTBT:$PC_{70}BM$ films spin-cast from CF (**a**), CB (**b**) and DCB (**c**) solvents. The insets show the surface phase images measured by atomic force microscopy (AFM). **d**,**e**, IPCE spectra (**d**) and *J–V* characteristics (**e**) of the devices fabricated with films cast from CF, CB and DCB.

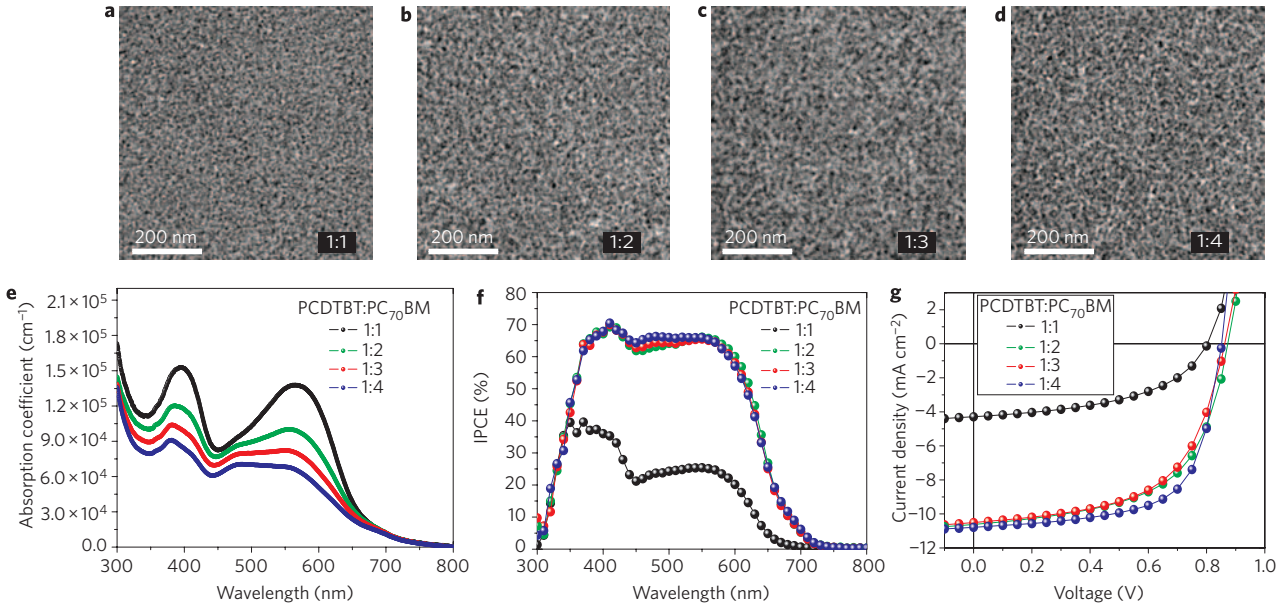

Figure 4 | The effect of blending ratio on film morphology and device performance. a–d, TEM images of the PCDTBT:$PC_{70}BM$ blend films spin-cast from DCB with increasing amounts of $PC_{70}BM$: blending ratios 1:1 (**a**), 1:2 (**b**), 1:3 (**c**) and 1:4 (**d**). **e**, Absorption coefficients of the films with blend ratios of 1:1, 1:2, 1:3 and 1:4. **f**, IPCE spectra for the same films as in **e. g**, *J–V* characteristics of the devices fabricated using BHJ films with blend ratios of 1:1, 1:2, 1:3 and 1:4.

Internal quantum efficiency

The morphology observed in Fig. 4d, using the 1:4 ratio of PCDTBT to $PC_{70}BM$, is ideal for polymer solar cell performance, as is made evident by the increased IQE. However, 80% of the film in terms of mass is now made of $PC_{70}BM$, which has only weak absorption in the visible spectral range. This is evident from the plot of the absorption coefficient shown in Fig. 4e. The decreased absorption coefficient for the 1:4 film reduces the number of absorbed photons in the active layer for fixed film thickness.

To determine the optimum blend ratio, we used the IPCE and *J–V* characteristics of the solar cells. Figure 4f shows the IPCE spectra of solar cells with various blend ratios. Although the IPCE curve obtained from the 1:1 device shows a poor photo-response,

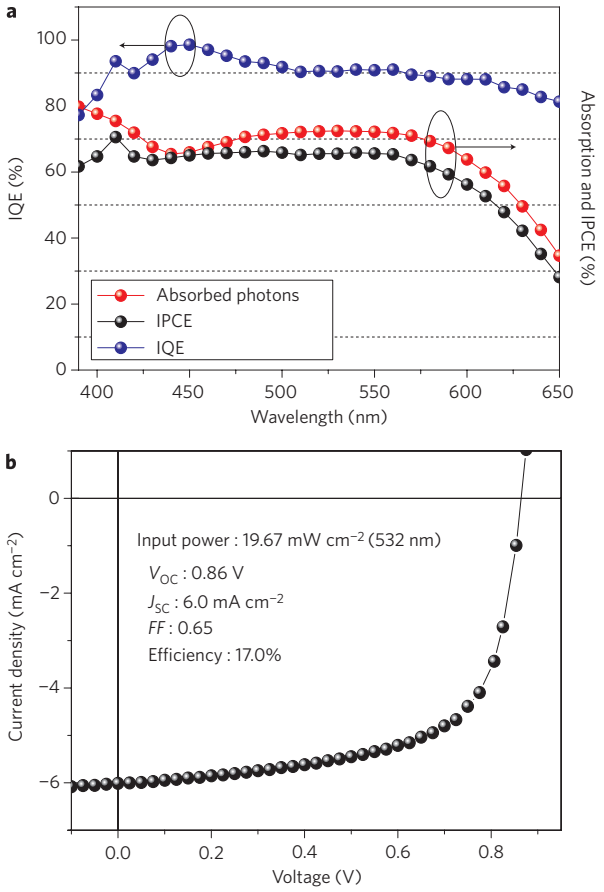

Figure 5 | Internal quantum efficiency (IQE) of PCDTBT:PC$_{70}$BM solar cells. a, IQE values of the 1:4 device with film cast from DCB. The red line shows the total absorption of the device, and the black line the IPCE. **b**, *J–V* characteristics of the device under monochromatic 532-nm light.

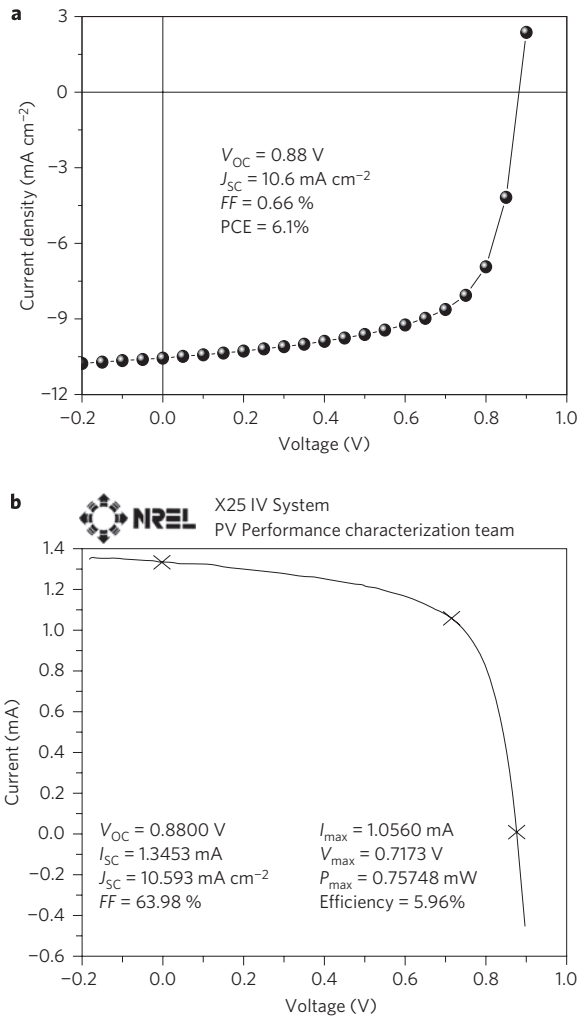

Figure 6 | Power conversion efficiency of PCDTBT:PC$_{70}$BM solar cells. a, *J–V* characteristics of a PCDTBT:PC$_{70}$BM solar cell under AM 1.5 G irradiation with an intensity of 100 mW cm^{-2}. **b**, NREL-certified *J–V* characteristics of a PCDTBT:PC$_{70}$BM solar cell.

comparable (and better) IPCE values are obtained from the 1:2, 1:3 and 1:4 ratios in the BHJ films. This observation is in good agreement with the *J–V* characteristics shown in Fig. 4 g. However, the *FF* values vary significantly amongst devices made from BHJ films with different blend ratios; the *FF* progressively increases as the PCDTBT to PC$_{70}$BM ratio decreases from 1:2 to 1:4. The photogenerated mobile carriers must be transported by means of percolated pathways to the respective electrodes. Breaks and 'dead ends' in the percolation pathways of the 1:1, 1:2 and 1:3 devices as seen in Fig. 4a–c increase the series resistance, and decrease the *FF*.

Measurements of the total absorption spectrum and the IPCE of the PCDTBT/PC$_{70}$BM solar cells enabled the calculation of the IQE spectrum[24,25,28] shown in Fig. 5a, where the red line indicates the total absorption of the 1:4 device and the black line the IPCE spectrum. We find that the PCDTBT/PC$_{70}$BM solar cells have remarkably high IQE values (that is, high efficiency of collected carriers per incident absorbed photon). The IQE (blue line) of the PCDTBT/PC$_{70}$BM solar cells approaches 100% around 450 nm and stays near or even above 90% throughout the entire absorption spectrum (400–650 nm). Such a high IQE is remarkable, indicating that nearly every absorbed photon leads to a separated pair of charge carriers and that all photogenerated carriers are collected at the electrodes.

Solar cell efficiency under monochromatic green light

The high efficiency of the PCDTBT/PC$_{70}$BM solar cells is further demonstrated when irradiated with monochromatic light. Figure 5b shows the *J–V* characteristics of a PCDTBT/PC$_{70}$BM BHJ device under monochromatic irradiation (532 nm) with an intensity of 19.67 mW cm^{-2}. The power conversion efficiency is $\eta_e = 17\%$ with $FF = 65\%$, $V_{OC} = 0.86$ V and $J_{SC} = 6.0$ mA cm^{-2}. Note that the measured 17% efficiency is consistent with IQE $\approx$ 95% at 532 nm when calculated directly from the *J–V* curve and the relatively low optical density at 532 nm (at 532 nm ~30% of the incident light is reflected out through the front surface). Because the IPCE of the device is nearly constant throughout the entire absorption spectrum (400–650 nm), it is possible to get ~17% efficiency from the entire absorption spectrum of PCDTBT. Therefore, the observation of $\eta_e = 17\%$ at 532 nm demonstrates that efficiencies of 10–15% should be achievable with BHJ cells fabricated using semiconducting polycarbazole derivatives with absorption spectra that extend deeper into the infrared; that is, with smaller energy gaps and similarly high IPCE. Tandem cells offer the promise of significantly higher values[4].

Power conversion efficiency of 6% under AM 1.5 G irradiation

Under standard measurement conditions[39,40], the PCDTBT/PC$_{70}$BM solar cells exhibit high PCE. The *J–V* characteristics of the device under AM 1.5 G irradiation from a calibrated solar simulator with irradiation intensity of 100 mW cm^{-2} are shown in Fig. 6a. The PCDTBT/PC$_{70}$BM solar cells reproducibly yield $J_{SC} = 10.6$ mA cm^{-2}, $V_{OC} = 0.88$ V, $FF = 0.66$ and $\eta_e = 6.1\%$. More than 20 out of 100 devices demonstrated efficiencies greater

than 6%. The highest value that we obtained in our laboratory was 6.2% with no antireflective coating on the glass. One of the PCDTBT/$PC_{70}BM$ solar cells with an initial efficiency of 6.1% (without antireflective coating) was sent to NREL for certification, after monitoring and ensuring the device performance for one week. NREL returned the device with a certified efficiency of 5.96%, as shown in Fig. 6b. Given the significant time lag between our sending the device to NREL and the measurement at NREL, we naturally expect some degradation. In fact, lifetime data gathered in our laboratory show that the device had already degraded somewhat by the time the NREL measurement was performed (see Supplementary Information).

Conclusion

In conclusion, we have successfully demonstrated high-efficiency BHJ solar cells comprising PCDTBT and $PC_{70}BM$ (1:4 ratio) as the active charge separating layer. With PCDTBT/$PC_{70}BM$, neither thermal annealing[6,36] nor the addition of processing additives[9,41] are required for achieving high efficiency. The PCDTBT/$PC_{70}BM$ solar cells exhibit $\eta_e = 6\%$ under AM 1.5 irradiation, the highest certified value reported to date. More important, the IQE of the PCDTB/$PC_{70}BM$ solar cells approaches 100%, implying that every photon absorbed leads to a separated pair of charge carriers and that every photogenerated mobile carrier is collected at the electrodes.

Methods

Device fabrication. Solar cells were fabricated on an indium tin oxide (ITO)-coated glass substrate with the following structure: ITO-coated glass substrate/poly(3,4-ethylenedioxythiophene) (PEDOT:PSS)/PCDTBT:$PC_{70}BM$/TiO_x/Al. The ITO-coated glass substrate was first cleaned with detergent, ultrasonicated in acetone and isopropyl alcohol, and subsequently dried overnight in an oven. PEDOT:PSS (Baytron PH) was spin-cast from aqueous solution to form a film of 40 nm thickness. The substrate was dried for 10 min at 140 °C in air and then transferred into a glove box to spin-cast the charge separation layer. A solution containing a mixture of PCDTBT:$PC_{70}BM$ (1:4) in dichlorobenzene solvent with a concentration of 7 mg/ml was then spin-cast on top of the PEDOT/PSS layer. The film was dried for 60 min at 70 °C in the glove box. The TiO_x precursor solution diluted 1:200 in methanol was spin-cast in air on top of the PCDTBT:$PC_{70}BM$ layer (5,000 rpm for 40 s). The sample was heated at 80 °C for 10 min in air. Then, an aluminium (Al, 100 nm) electrode was deposited by thermal evaporation in a vacuum of about 5×10^{-7} torr. Current density–voltage (J–V) characteristics of the devices were measured using a Keithley 236 Source Measure Unit. Solar cell performance used an Air Mass 1.5 Global (AM 1.5 G) solar simulator with an irradiation intensity of 1,000 W m^{-2}. An aperture (12.7 mm^2) was used on top of the cell to eliminate extrinsic effects such as crosstalk, waveguiding, shadow effects and so on. The spectral mismatch factor was calculated by comparison of the solar simulator spectrum and the AM 1.5 spectrum at room temperature.

Measurement system. Our measurement system yielded data in precise agreement with measurements made at NREL. Results for cells returned to us after NREL measurement had expected values. Our integrated IPCE values always agreed with the measured short-circuit current to within a few percent.

TEM microscopy. Specimens were prepared by first casting a PCDTBT:$PC_{70}BM$ blend thin film on glass. The films were baked at 70 °C for 1 h, and then removed from the nitrogen environment and scored with a diamond scribe to define the sample size. The substrate and film were immersed in deionized water for 20 min and sonicated to promote delamination. Resulting pieces of the film were transferred to a PELCO copper TEM grid with a carbon/Formvar support grid. TEM specimens were allowed to dry under low heat to remove excess water from the transfer process. Light field imaging was performed in an FEI T20 TEM using proper defocus for additional phase contrast from the relatively amorphous polymer material.

Received 19 December 2008; accepted 24 March 2009; published online 26 April 2009

References

1. Sariciftci, N. S., Smilowitz, L., Heeger, A. J. & Wudl, F. Photoinduced electron transfer from a conducting polymer to buckminsterfullerene. *Science* **258,** 1474–1476 (1992).
2. Yu, G., Gao, J., Hemmelen, J. C., Wudl, F. & Heeger, A. J. Polymer photovoltaic cells: enhanced efficiencies via a network of internal donor–acceptor heterojunctions. *Science* **270,** 1789–1791 (1995).
3. Halls, J. J. *et al.* Efficient photodiodes from interpenetrating polymer networks. *Nature* **376,** 498–500 (1995).
4. Kim, J. *et al.* Efficient tandem polymer solar cells fabricated by all-solution processing. *Science* **317,** 222–225 (2007).
5. Li, G. *et al.* High-efficiency solution processible polymer photovoltaic cells by self-organization of polymer blends. *Nature Mater.* **4,** 864–868 (2005).
6. Ma, W. Yang, C., Gong, X., Lee, K. & Heeger, A. J. Thermally stable, efficient polymer solar cells with nanoscale control of the interpenetrating network morphology. *Adv. Funct. Mater.* **15,** 1617–1622 (2005).
7. Kim, Y. *et al.* A strong regioregularity effect in self-organizing conjugated polymer films and high-efficiency polythiophene:fullerene solar cells. *Nature Mater.* **5,** 197–203 (2006).
8. Muhlbacher, D. *et al.* High photovoltaic performance of a low-bandgap polymer. *Adv. Mater.* **18,** 2884–2889 (2006).
9. Peet, J. *et al.* Efficiency enhancement in low-bandgap polymer solar cells by processing with alkane dithiols. *Nature Mater.* **6,** 497–500 (2007).
10. Wang, E. *et al.* High-performance polymer heterojunction solar cells of a polysilafluorene derivative. *Appl. Phys. Lett.* **92,** 033307–033310 (2008).
11. Blouin, N. *et al.* Toward a rational design of poly(2,7-carbazole) derivatives for solar cells. *J. Am. Chem. Soc.* **130,** 732–742 (2008).
12. Blouin, N., Michaud, A. & Leclerc, M. A low-bandgap poly(2,7-carbazole) derivative for use in high-performance solar cells. *Adv. Mater.* **19,** 2295–2300 (2007).
13. Hoppe, H. & Sariciftci, N. S. Organic solar cells: An overview. *J. Mater. Res.* **19,** 1924–1945 (2004).
14. Winder, C. & Sariciftci, N. S. Low bandgap polymers for photon harvesting in bulk heterojunction solar cells. *J. Mater. Chem.* **14,** 1077–1086 (2004).
15. Hayakawa, A., Yoshikawa, O., Fujieda, T., Uehara, K. & Yoshikawa, S. High performance polythiophene/fullerene bulk-heterojunction solar cell with a TiO_x hole blocking layer. *Appl. Phys. Lett.* **90,** 163517 (2007).
16. Scharber, M. C. *et al.* Design rules for donors in bulk-heterojunction solar cells—towards 10% energy-conversion efficiency. *Adv. Mater.* **18,** 789–794 (2006).
17. Brabec, C. J., Sariciftci, N. S. & Hummenlen, J. C. Plastic solar cells. *Adv. Mater.* **11,** 15–26 (2001).
18. Brabec, C. J. *et al.* Origin of the open circuit voltage of plastic solar cells. *Adv. Funct. Mater.* **11,** 374–380 (2001).
19. Arbogast, J. W. & Foote, C. S. Photophysical properties of C_{70}. *J. Am. Chem. Soc.* **113,** 8886–8889 (1991).
20. Wienk, M. M. *et al.* Efficient methano[70]fullerene/MDMO-PPV bulk heterojunction photovoltaic cells. *Angew Chem. Int. Ed.* **42,** 3371–3375 (2003).
21. Kim, J. Y. *et al.* New architecture for high-efficiency polymer photovoltaic cells using solution-based titanium oxide as an optical spacer. *Adv. Mater.* **18,** 572–576 (2006).
22. Lee, K. *et al.* Air-stable polymer electronic devices. *Adv. Mater.* **19,** 2445–2449 (2007).
23. Cho, S. *et al.* Multilayer bipolar field-effect transistors. *Appl. Phys. Lett.* **92,** 063505 (2008).
24. Persson, N.-K. & Inganas, O. in *Organic Photovoltaics* Ch. 5 (Taylor & Francis, 2005).
25. Slooff, L. H. *et al.* Determining the internal quantum efficiency of highly efficient polymer solar cells through optical modeling. *Appl. Phys. Lett.* **90,** 1435061 (2007).
26. Mayer, A. C., Scully, S. R., Hardin, B. E., Rowell, M. W. & McGehee, M. D. Polymer-based solar cells. *Mater. Today* **10,** 28–33 (2007).
27. Schilinsky, R., Waldauf, C. & Brabec, C. J. Recombination and loss analysis in polythiophene based bulk heterojunction photodetectors. *Appl. Phys. Lett.* **81,** 3885–3887 (2002).
28. Dennler, G. *et al.* Angle dependence of external and internal quantum efficiencies in bulk-heterojunction organic solar cells. *J. Appl. Phys.* **102,** 0545161 (2006).
29. Vacar, D., Maniloff, E. S., McBranch, D. W. & Heeger, A. J. Charge-transfer range for photoexcitations in conjugated polymer/fullerene bilayers and blends. *Phys. Rev. B* **56,** 4573–4577 (1997).
30. Shaw, P. E., Ruseckas, A. & Samuel, I. D. W. Exciton diffusion measurements in poly(3-hexylthiophene). *Adv. Mater.* **20,** 3516–3520 (2008).
31. Kraabel, B. *et al.* Subpicosecond photoinduced electron transfer from conjugated polymers to functionalized fullerenes. *J. Chem. Phys.* **104,** 4267–4273 (1996).
32. Brabec, C. J. *et al.* Transient photoinduced electron transfer process in conjugated polymer/fullerene bulk heterojunction in real time. *Chem. Phys. Lett.* **340,** 232–236 (2001).
33. Yao, Y. Hou, J., Xu, Z., Li, G. & Yang, Y. Effects of solvent mixtures on the nanoscale phase separation in polymer solar cells. *Adv. Funct. Mater.* **18,** 1783–1789 (2008).
34. Gunes, S., Neugebauer, H. & Sariciftci, N. S. Conjugated polymer-based organic solar cells. *Chem. Rev.* **107,** 1324–1338 (2007).
35. Zhang, F. *et al.* Influence of solvent mixing on the morphology and performance of solar cells based on polyfluorene copolymer/fullerene blends. *Adv. Funct. Mater.* **16,** 667–674 (2006).

36. Hoppe, H. & Sariciftci, N. S. Morphology of polymer/fullerene bulk heterojunction solar cells. *J. Mater. Chem.* **16,** 45–61 (2006).
37. Ma, W., Yang, C. & Heeger, A. J. Spatial Fourier-transform analysis of the morphology of bulk heterojunction materials used in plastic solar cells. *Adv. Mater.* **19,** 1387–1390 (2007).
38. Moon, J. S., Lee, J. K., Cho, S., Byun, J. & Heeger, A. J. Columnlike structure of the cross-sectional morphology of bulk heterojunction materials. *Nano Lett.* **9,** 230–234 (2009).
39. Shrotriya, V. *et al.* Accurate measurement and characterization of organic solar cells. *Adv. Funct. Mater.* **16,** 2016–2023 (2006).
40. Metzdorf, J., Winter, S. & Wittchen, T. Radiometry in photovoltaics: calibration of reference solar cells and evaluation of reference values. *Metrologia* **37,** 573–578 (2000).
41. Lee, J. K. *et al.* Processing additives for improved efficiency from bulk heterojunction solar cells. *J. Am. Chem. Soc.* **130,** 3619–3623 (2008).

Acknowledgements

The research leading to the results reported here was supported by the Air Force Office of Scientific Research, the Department of Energy and by a grant from the US Army CERDC. The TiO_x development work was carried out at the Heeger Center for Advanced Materials (Gwangju Institute of Science and Technology (GIST) and UCSB) with support from under the Global Research Laboratory (GRL) Program sponsored by the Korean Government. The authors thank C. Brabec and R. Gaudiana for advice and encouragement, and for supplying the $PC_{70}BM$. The measurements at NREL were carried out by P. Ciszek and K. Emery. We thank them for their help and cooperation.

Additional information

Supplementary information accompanies this paper at www.nature.com/naturephotonics. The authors declare competing financial interests: details accompany the full-text HTML version of the paper at www.nature.com/naturephotonics. Reprints and permission information is available online at http://npg.nature.com/reprintsandpermissions/. Correspondence and requests for materials should be addressed to K.L. and A.J.H.

ERRATUM

Heat-assisted magnetic recording by a near-field transducer with efficient optical energy transfer

W. A. Challener, Chubing Peng, A. V. Itagi, D. Karns, Wei Peng, Yingguo Peng, XiaoMin Yang, Xiaobin Zhu, N. J. Gokemeijer, Y.-T. Hsia, G. Ju, Robert E. Rottmayer, Michael A. Seigler and E. C. Gage

Nature Photonics **3,** 220–224 (2009); published online 22 March 2009, corrected after print 24 March 2009.

In the version of this article originally published, in the caption to Fig. 4a the distance between the dashed lines was incorrectly given as 0.050 nm; this should have read 0.050 μm. The error has now been corrected in the HTML and PDF versions.

CORRIGENDUM

Complete optical isolation created by indirect interband photonic transitions

Zongfu Yu and Shanhui Fan

Nature Photonics **3,** 91–94 (2009); published online: 11 January 2009; corrected online 15 April 2009.

The authors wish to correct equation (4) of the above Letter; it should have appeared as shown below. This also affects the final sentence in the third paragraph from the end of page 92, which should now read: For this device, our calculation indicates that over a frequency bandwidth of 1.2 THz, the contrast ratio between forward and backward transmission coefficients is above 40 dB.

$$a_1(z) = e^{-iz\Delta k/2}\left[\cos\left(z\sqrt{C^2+(\Delta k/2)^2}\right) + i\frac{\Delta k/2}{\sqrt{C^2+(\Delta k/2)^2}}\sin\left(z\sqrt{C^2+(\Delta k/2)^2}\right)\right]$$

$$a_2(z) = ie^{iz\Delta k/2}\frac{C\sin\left(z\sqrt{C^2+(\Delta k/2)^2}\right)}{\sqrt{C^2+(\Delta k/2)^2}} \qquad (4)$$

Bright future for electronic paper

A prototype display technology that electromechanically transports colourful aqueous dispersed pigments over the surface of mirror-like pixels is a promising new approach to making electronic paper with high reflectivity and contrast. *Nature Photonics* spoke to Jason Heikenfeld to learn more.

Where did the idea of making an electrofluidic display come from?

I started electrowetting display work in late 2003 and have been involved in several academic–corporate projects in the area. This has included collaborations with Prime View International (PVI) and the Industrial Technology Research Institute (ITRI), both in Taiwan, and with Sun Chemical, Motorola and Polymer Vision. Sun Chemical is one of the world-leading providers of pigments, so it should be no surprise that Russ Schwartz of Sun Chemical and I were exploring ways to use Sun Chemical pigments in electrowetting displays. Our basic pixel switching concept was realized while I was reading some papers on the role of Young–Laplace pressure in electrowetting lab-on-chip devices. Our first attempt can be seen in our published work on arrayed electrowetting microwells. Our second attempt (see photo) was drastically different in structure and closer to that which we report in this issue. I vividly remember viewing this device in the lab with our post-doc Dr Bo Sun. The device was crude, but both Russ and I were absolutely struck by the brilliant coloration exhibited by the device. This device had paper-like colour that was unlike anything we had previously seen in electrowetting or electrophoretic displays. As we do with all our new discoveries, we next spent a few months theoretically refining the device design, and mapping out manufacturability and performance metrics. Only after that did we begin intense research and development of the electrofluidic display platform.

How exactly does an electrofluidic display operate?

The long-term goal of reflective displays is to mimic the appearance of pigment on paper. This means more than just bright colour: the reflection also has to be diffuse like paper rather than specular like a mirror. One could argue that the ultimate reflective display would simply place the best colorants used by the printing industry directly beneath the front viewing substrate of a display. In our electrofluidic display pixels we place an aqueous pigment dispersion inside a tiny reservoir. The reservoir comprises ~5–10% of the viewable pixel area and therefore the pigment is substantially hidden from view in the pixel's off state. We then use voltage to electromechanically pull the pigment out of the reservoir and spread it as a film directly behind the viewing substrate. As a result, the display takes on a colour and brightness similar to that of conventional pigments printed on paper. When we remove the voltage, Young–Laplace pressure (surface tension) causes the pigment dispersion to recoil rapidly back into the reservoir.

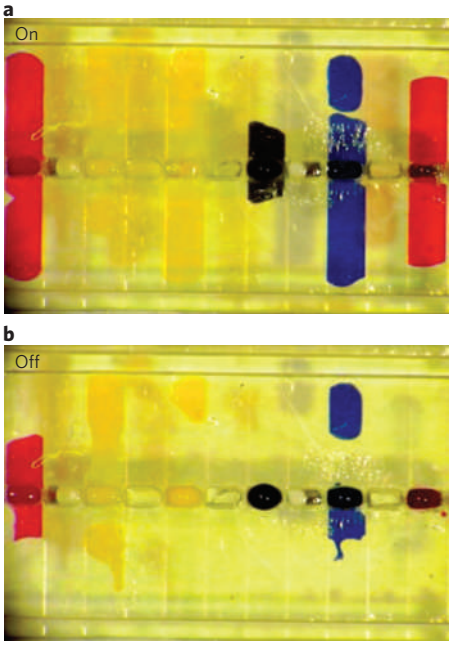

The early days: image of a switched pigment pixel in its on and off states from one of the team's earlier designs.

What are the benefits of your scheme over competing electronic-paper and reflective display technologies?

First, our displays have the potential for a much higher contrast ratio and brightness. In simple terms our displays will look more like real paper than current e-paper. We believe that consumers will place a great deal of value on this benefit. Low power consumption, rollable functionality and video capabilities are all desirable features for e-paper but ultimately what consumers want is a bright display with saturated full colour, which is not currently available. Another key advantage of this technology is that it is much easier to offer a wide array of colour because we already have a high-performance colour set just like that in your inkjet printer, so we can mix these colours and deliver any desired colour at no additional cost. A third advantage is that there is no colour mixing within each pixel. For electrophoretic displays like the Amazon Kindle [an e-book platform] one colorant must be electrically segregated from another, but this separation is not complete and there is always colour mixing which adversely affects shade. This is not to imply that electrophoretic displays are not a brilliant invention, but they are not perfect. In summary, our new displays are a major step forward in realizing true paper-like reflective displays. Our newer embodiments further reduce manufacturing complexity, and we estimate for simple applications that it should be possible to hit an ultimate cost point of less than US$10 per square foot.

Tell me about your future plans?

Now that we have published these first-generation devices we have two major ongoing activities. First, we are exploring some interesting alternative designs of an electrofluidic pixel. As part of this work we are collaborating with Dr Rajesh Naik of the Materials and Manufacturing Directorate at the Air Force Research Laboratory on designing bioinspired devices that mimic the dynamic coloration seen in cephalopods. Second, we have just launched a new company named γ-Dynamics to off-load and accelerate commercial development. This company includes John Rudolph and Ken Dean as founding members, both of whom are well known in the displays industry. This commercialization effort also includes a partnership with PolymerVision for creating full-colour rollable displays.

INTERVIEW BY OLIVER GRAYDON

Jason Heikenfeld and his co-workers have a paper on their electrofluidic display research on page 292 of this issue.